Abstract

LIN, XIAO Structural Health Monitoring using Geophysical Migration Technique with Built-in Piezoelectric Sensor/Actuator Arrays. (Under the direction of Dr. F. G. Yuan)

Lamb waves based ultrasonic testing has been studied for many years. However, conventional methods of generating and collecting of Lamb waves usually require bulky instruments and manual interference, thus can not be applied directly for in-situ or in-service monitoring of the structural health. Especially, the method of interpreting the Lamb waves in an active structural health monitoring (SHM) system with built-in piezoelectric sensors/actuators is not available yet. The objective of this study was to propose and validate, through numerical simulation and experimental studies, the feasibility of adopting the geophysical migration method to interpret the ultrasonic Lamb wave signals for the purpose of realizing quantitative damage identification.

A homogeneous isotropic plate with a surface-mounted linear piezoelectric ceramic (PZT) disk array is studied as an example. The piezoelectric disks act as actuators to excite Lamb waves and also as sensors to receive the waves reflected from the structural anomaly in the plate. The migration technique, which is an advanced technique in geophysics to reverse the reflection wave field and to image the Earth interior, is then used to back-propagate the recorded wave signals and to visually image the damage in the plate. Mindlin plate theory is adopted to model the propagating waves, and a two-dimensional 2-6 order explicit finite difference algorithm is used to synthesize the reflection waves and to implement the migration process. The stability and accuracy

criteria of the finite difference algorithm when used in plate problems is discussed. An analytical solution is derived for the transient Lamb waves of an infinite plate subject to a point loading. This solution is used to verify the accuracy of the finite difference calculation. Both poststack and prestack migration are studied to propagate the reflection energy back to the damages. For the poststack migration, a one-way version of flexural wave equation is derived and the data pre-processing procedures before migration, such as muting direct arrival, deconvolution and stacking, are discussed. For prestack migration, an excitation-time imaging condition specifically for the migration of waves in a plate is introduced based on ray-tracing concepts and the asymptotic properties of flexural wave velocities and the migration is proceeded through the full-way wave equation. The results of numerical simulation show that the migration method possesses the capability of identifying multiple discrete damages without *a priori* assumption on the distribution pattern of the damages. Thus not only the existence but also the shape and the dimensions of the damages can be visually identified. An experimental apparatus is then set up to validate the conclusions drawn from the synthetic data. For calibration of the system, an analytical model of the waves in a plate incorporated with PZT sensors/actuators is developed. The agreement between the model calculated data and the measured data in the experiment shows that A_0 mode Lamb waves are accurately generated and collected. Finally, the migration results from the reflection waves of an artificial damage in an arc shape recorded in the experiment are presented. It is shown that the existence of the damage could be correctly imaged through the migration process as it was shown in the numerical simulation.

STRUCTURAL HEALTH MONITORING USING GEOPHYSICAL MIGRATION TECHNIQUE WITH BUILT-IN PIEZOELECTRIC SENSOR/ACTUATOR ARRAYS

by

Xiao Lin

A dissertation submitted to the Graduate Faculty of
North Carolina State University
in partial fulfillment of the
requirements for the Degree of
Doctor of Philosophy

Aerospace Engineering

Raleigh

2000

Approved by:

Dr. Jeffrey W. Eischen

Dr. Y. Richard Kim

Dr. Larry M. Silverberg

Dr. Fuh G. Yuan
Chairman of Advisory Committee

Biography

Xiao Lin was born on July 18, 1965 in Yudu, Jiangxi Province, the People's Republic of China. Having received his elementary and secondary education in Yudu, he graduated from the First High School of Yudu in 1981. He received Bachelor of Science degree in 1985 and Master of Science degree in 1988, both in the Department of Mechanical Engineering, Huazhong University of Science and Technology. He then joined the faculty of the Department of Mechanical Engineering in East China Jiaotong University in 1988 and had been teaching there for nine years since then. In the fall of 1997, he entered the Ph. D. program of Aerospace Engineering in North Carolina State University at Raleigh, and resumed his student life till now.

Acknowledgements

First of all, I would like to thank Dr. F. G. Yuan for suggesting the following work and serving as my graduate advisor over the past three years. I appreciate very much his guidance and enthusiastic encouragement that Dr. Yuan has given to me throughout the work. Especially, his insight into cross-disciplinary research and his insistence of pursuing excellence in research influence me greatly and surely my future academic career will benefit much from it.

I would also like to thank all the other committee members. I thank Dr. Jeffrey W. Eischen for his patience and kindness he has shown me whenever I met academic challenges. I thank Dr. Y. Richard Kim for his excellent instructions that brought me a panorama vision of Nondestructive Testing techniques. I thank Dr. Larry M. Silverberg who helped me understand the engineering value of this study and gave me lots of invaluable advice regarding the experiment work.

Special thank goes to Dr. Yetmen Wang, who offered me the kernel code of the finite difference algorithm used in this study and provided numerous information regarding many aspects of the current research. Without his generous help, much longer time could be needed to complete this work.

I would also like to express my thanks to Mr. Rufus L. Richardson and Mr. Mike Breedlove. They have given me lots of help in building the experimental facilities and manufacturing many precise and art-like parts. Also, thanks go to all the members in our research group for their care and help. The friendship with them makes my life in Raleigh brighter and more colorful.

Finally, but not least, I should thank my lovely wife Yun and sweet daughter Qinnan. It is their considerateness and tolerance that ensures I can spend more time in the lab and concentrate on the study. I wish I could have any chances that I can compensate a little what they lost because of my negligence during the study.

Table of Contents

List of Tables

List of Figures

Nomenclature & Abbreviations

Greek symbols

β	duration time of the applied force to the plate, s
$\Delta s (= \Delta x = \Delta y)$	grid space, in.
Δt	time step, s
$\boldsymbol{\varepsilon}$	vector of dielectric permittivity ε_{ij}, F/in.
ε_0	the dielectric permittivity of a free space, $\varepsilon_0 = 2.2479\times10^{-13}$ F/in.
κ	shear correction factor, $\kappa^2 = \pi^2/12$
Λ	actuation strain of the piezoelectric actuator, in./in.
λ	wavelength, in.
ν	Poisson's ratio
ρ	mass density, lb./in.^{3}
σ	vector of stress components σ_{ij}, psi
ω	angular frequency, rad/s
ψ	rotation of the vertical section of the plate, in./in.

Roman symbols

A, B	constants defined in eq. (2.11)
a	radius of the piezoelectric disk, in.
C	phase velocity, in./s
C_0	velocity of plate waves, in./s

$C_{\max}$	maximum phase velocity of the waves of all possible modes, in./s
C_{mV}	voltage-moment conversion coefficient, lb./V
C_P	velocity of dilational waves, in./s
C_R	velocity of Raleigh surface waves, in./s
C_S	velocity of shear waves, in./s
D	vector of electric displacements D_i, C/in.^{2}
D	plate bending stiffness, $D = Eh^3/[12(1-\nu^2)]$
d	vector of piezoelectric strain constants d_{ij}, in./V
E	vector of electric fields E_i, V/in.
E	Young's modulus, psi
f	frequency, Hz
f_0	central frequency of the sinusoid modulation signal, Hz
f_c	cut-off frequency, Hz
G	shear modulus, psi
G'	modified shear modulus, $G' = \kappa^2 G$, psi
$H(t)$	Heaviside step function
$H_m^{(n)}$	Hankel function of the nth kind of order m
h	plate thickness, in.
K_3	relative dielectric constant
k	wavenumber
M	bending and twisting moment, lb·in./in.
N_p	number of cycles of the sinusoid modulation signal
P	amplitude of the applied pressure to the plate, psi

Q	transverse shear force per unit of length, lb/in.
q	pressure loading on the plate in normal direction, psi
R	the distance between the center of the actuator and the sensor, in.
r	distance between the loading (actuator) and the measuring position, in.
r'	distance between the sensor and the measuring position, in.
$\mathbf{S}$	vector of strain components S_{ij}, in./in.
$\mathbf{s}$	vector of compliance constants s_{ij}, 1/lb.
t	time, sec.
t_d	one-way travel time between two points, s
x, y, z	rectangular coordinates, centered at the plate neutral axis
x', y', z'	rectangular coordinates, with origin at the center of PZT sensor
$\mathbf{u}$	vector of unknowns in the finite difference algorithm
u, v, w	displacements in the directions of x, y and z, respectively, in.

Subscripts

a	denotes absorbing boundary
b	denotes bonding layer
i, j	denotes the index of grid point in the x and y direction, respectively
p	denotes piezoelectric material
V_{in}	input voltage applied on the piezoelectric actuators, V
V_{out}	output voltage from the piezoelectric sensors, V
x, y, r, θ	denote the directions in rectangular and polar coordinates with origin at the center of the actuator or the point loading position

x', y', r', θ' denotes the directions in rectangular and polar coordinates with origin at the center of the sensor

Superscripts

n denotes the index of time step

Caps

~ denotes variables in frequency domain

Abbreviations

ABC	Absorbing Boundary Condition
AF	Anisotropic Filtering
ANN	Artificial Neural Network
CFL	Courant-Friedrichs-Lewy Stability Criterion
CMP	Common Middle Point
CPT	Classical Plate Theory
FE	Finite Element
FD	Finite Difference
GUI	Graphical User Interface
MPT	Mindlin Plate Theory
NDT/E	Nondestructive Testing/Evaluation
NMO	Normal MoveOut
PML	Perfectly Matched Layer

PZT	Lead Zirconate Titanate
SHM	Structural Health Monitoring
SNR	Signal to Noise Ratio

1 Introduction

1.1 Background

Integrity of critical structures such as aircraft, nuclear reactors, pressure vessels, etc., needs to be monitored constantly to prevent catastrophic failure. In order to respond to any possible damage leading to failure of the structures, damages should be detected, evaluated, if possible monitored, even though the structures might be in services. Traditional nondestructive testing/evaluation (NDT/NDE) techniques can not be applied directly to monitor structures' health status because these techniques usually are based on in-laboratory testing and require bulky instruments (Thomas, 1995). Especially for aerospace vehicles, the health monitoring system requires to perform on in-service structures in isolated environments without manual interference. Thus, integrating monitoring components such as sensors, either surface-mounted or embedded, into the structures is compulsory in these circumstances (Boller, 1997). A structural health monitoring (SHM) system with built-in sensors is called smart SHM system and has attracted much attention in the past decade (Chang, 1999; Hickman *et al*., 1991; Kudva *et al*., 1993). Besides sensors, transmitters or actuators, whose function is to excite diagnostic signals, can also be implanted in the structures to build an active SHM system. Moreover, a major advantage of the active SHM system over a passive one (without built-in actuators) is that the active SHM is subjected to a pre-scribed actuation and thus increases the possibility of deducing the structure status from the collected sensor data. A primary issue in constructing active SHM system is to choose suitable monitoring signals. Although in general sense any physical signals could be used to monitor the structural health, ultrasonic stress waves have been considered as a principal candidate of potential signals in active SHM systems (Boller, 1996).

Stress waves propagate in plate-like structures in directions parallel to the plate surfaces is defined as Lamb waves or guided elastic waves. Lamb waves can propagate over long distances and provide a potentially very attractive means in the health

monitoring for large area structures like wings and fuselages (Achenbach and Thompson, 1991). Lamb wave based testing can potentially detect varies of damages - such as corrosions, delaminations, cracks - not only on the surface but also hidden inside the structures, and the detectability of small damages can be obtained simply by increasing the frequency of diagnosis signals. Unlike diagnostic signals in other monitoring schemes like penetrant, eddy current, X-ray inspection, etc., the generation and collection of wave signals are readily accommodated through the structure integrated with sensors/actuators. The difficulties of applying ultrasonic Lamb wave based monitoring lie on the signals are not instinctually interpretable due to their dispersive characteristics and complicated mode conversion phenomena (Alleyne and Cawley, 1992a and 1992b). This difficulty is further augmented due to the interaction between host structures and sensors/actuators in a smart SHM. Many researches have been conducted utilizing Lamb wave based smart SHM and these researches could be divided into three major categories:

(a) Integrating and optimizing actuators/sensors in structures for Lamb wave generation and reception;
(b) Modeling with experimental verification the propagation of Lamb waves and their interaction with damages;
(c) Developing robust diagnosis algorithms to extract health status information from the received wave signals.

1.2 Lamb wave generation and reception

Traditional techniques of generating and receiving Lamb waves began in the 1950s and have not changed much since then (Worlton, 1957; Kino *et al*., 1980; Bar-Cohen, 1998). The Lamb wave based testing requires two transducers as a transmitter and a receiver separately, or just one that functions as both transmitter and receiver, depending on whether the testing scheme is pitch-catch or pulse-echo configuration. In most cases the Lamb wave transducers are made of piezoelectric materials due to the coupled electromechanical behavior and its excellent dynamic response characteristics. In some

acoustic emission studies, lead break was also used to emulate the source of plate waves (Gorman and Prosser, 1996; Hsu *et al*., 1977). In the past decade, EMATs (electro-magnetic acoustic transducer) and fiber optic are also used to either generate or receive Lamb waves respectively (Guo *et al*., 1991). Especially, studies of laser based ultrasonic Lamb wave testing are growing rapidly (Hayashi *et al*., 1999). Unlike conventional methods, laser based ultrasonic testing does not require couplant or immersion of the specimen in the liquid and provides a method to realize non-contact ultrasonic testing. One of the disadvantages of the conventional ultrasonic Lamb wave based NDT techniques is that a test is executed point by point, thus is time-consuming and not suitable for in-service testing. Recently, many researchers have studied the technique of integrating piezoelectric actuators and sensors into structures for the purpose of generating and collecting diagnostic Lamb waves and thus realizing continuous monitoring of the structural integrity. In Roh and Chang's study (1995), distributed piezoelectric ceramic (PZT) disks were surface-mounted on a composite structure to generate and receive the diagnostic signals for impact damage detection. The experimental results showed very promising features of integrated sensor/actuator technique in structures for health monitoring purposes. Bonding the piezoelectric ceramics on the two opposite sides of surfaces of a plate accommodates generating A_0 and S_0 mode Lamb waves separately and the current study adopts this method as well. Egusa and Iwasawa (1998) made piezoelectric paint from piezoelectric ceramic powder that could be coated on complex shape of structures to fabricate an intelligent material system. It was proven that the paint possesses the sensor capability of collecting dynamic signals in damage detection applications. Comparing with piezoelectric ceramic, piezoelectric polymer film has higher dielectric voltage constants and is recognized as a better sensor material. It is also flexible and could be easily cut into any shape to fit a complex structural shape. Polyvinylidene fluoride (PVDF) was used in Cawley's study bonding on the specimen to excite Lamb waves (Monkhouse *et al*., 1997). Their experimental results showed that Lamb waves ranged from 0.5 to 4MHz could be efficiently generated through the design. In this design, interdigital electrode patterns on the PVDF substrate were controllable for generating desirable Lamb mode shapes to

suppress the dispersive effect, which has been a major barrier to the interpretation of Lamb wave signals. Selecting interdigital electrode pattern to generate desired flexural and bulk waves was also studied by Moetakef group (Moetakef *et al*., 1996). In their studies, each electrode was applied a voltage independently with a pre-set time delay, which coordinated with the electrode pattern to control the excitation. The problem was also modeled by finite element methods to provide a comparison with the experimental results. Piezoelectric sensors/actuators may also be embedded inside the structure rather than mounted on the surface. In a paper by Moulin and his colleagues (Moulin *et al*., 1997), a piezoelectric element was embedded into a carbon-epoxy composite plate and acted as an actuator to generate Lamb waves. The displacement field on the plate surface was predicted by a hybrid finite element – normal mode expansion method and was verified experimentally by an optical measurement.

1.3 Modeling and experimental studies of Lamb waves

Building a model for stress wave propagation in the structures and the interaction between the waves and damages is a prerequisite for achieving the goal of quantitative damage identification. Modeling the transient flexural waves in a plate induced by point loading (a point transmitter) has been examined by many researchers (Miklowitz, 1960; Weaver and Pao, 1982). However, it is commonly recognized that even though the equation of Lamb waves in the frequency domain has a rather simple form, fully understanding the physics for every mode to give an analytical expression of the wave motion remains a research topic. Even for some approximation expressions derived by ray-tracing or normal mode expansion method, the calculation is computationally intensive and thus far field waves (10 plate thickness away from the loading point) solution was not accessible yet (Weaver and Pao, 1982). Therefore, simplified models have been resorted to by many researchers to describe lower-order modes of the flexural waves. For characterizing the first antisymmetric mode (A_0) Lamb waves or flexural waves, many studies (Doyle, 1989; Medick, 1961) used classical plate theory (CPT) based on Kirchhoff thin plate assumption, in which the effect of rotary inertia and

transverse shear deformation is ignored. However, it is found that for ultrasonic signals whose frequency span is in the order of kHz to MHz, rotary inertia and transverse shear deformation must take into account, even for rather thin plates. By taking these two effects into consideration, Mindlin plate theory (MPT) (Mindlin, 1951) is a better approximation theory for A_0 mode Lamb waves and has been used in numerous studies. Regarding the interaction of Lamb waves with anomalies in structures, analytical solutions are limited on very simple types of damages based on the simplified theories (Pao and Chao, 1964; Norris and Vemula, 1995; Vermula and Norris, 1997). Numerical studies are often examined to explore Lamb waves in the structures with complex shape and/or boundary constraints and to model the scattering effect from damages or inhomogeneities. Finite element (FE) methods have often been used in numerical studies (Karunasena *et al*., 1995, Kundu and Maslov, 1997). Nevertheless, the requirement of fine mesh to simulate accurately the wave scattering phenomena makes the computational burden unacceptable if the far field response is required. Recently, some researchers combine the finite element with normal mode expansion method together to increase the computational efficiency (Datta *et al*., 1991; Moulin *et al*., 1999). The FE code is to mesh the interface between the structure and the damages and to calculate the near field wave phenomena. Normal mode solution is then applied to obtain the far field response by matching the boundary conditions between the two calculation regions.

Finite difference (FD) methods have long been used to solve wave propagation problems, especially in geophysics and seismology (Cherukuri *et al*., 1996; Dai, 1993; Gottlieb and Turkel, 1976; Kelly *et al*., 1976). An advantage of FD method over FE method for a transient problem is that the mesh dispersive effect in the FD is not as serious as in the FE method, thus a larger time step is allowed in the simulation. The applications of FD modeling in ultrasonic testing are continuously growing and an extensive review about FD in NDT applications was given by Bond (1988). It is asserted in that review that up to late 80s, the FD model can only solve problems with characteristic dimensions smaller than three times the wavelength and larger than one-tenth of the wavelength. Due to the computational burden, structures used in FD

simulation are always modeled in size smaller than the real dimensions. Thus absorbing boundaries are needed to be constructed for the edges of the calculation mesh, so that the edges behave like "transparent" and will not introduce artificial reflection waves or the reflection could be reduced to an acceptable level. Many algorithms have been proposed to construct effective absorbing boundaries. One-dimensional absorbing boundary is widely used (Gottlieb *et al*., 1982), but it can only absorb normal incidence compressional and shear waves. Clayton and Engquist (1977) used a paraxial approximation of the elastic wave equation to construct absorbing boundaries, which can be much more conveniently implemented in two-dimensional problems. Dai (1993) proposed a compound absorbing boundary which can effectively absorb waves with a large range of incidence angles. Another issue in FD simulation is the accurate implementation of physical boundary conditions (Gottlieb *et al*., 1982), i.e., free-surface conditions for Lamb wave problems. Balasubramanyam *et al*. (1996) intentionally chose a second-order FD algorithm, so that the free surface condition could be easily implemented through the difference equations of the displacement expressions. MPT was used in a study by Assadi-Lamouki to build the FD model (Assadi-Lamouki *et al*., 1989). Both the bending and twisting moments can be expressed in terms of transverse deformation and the boundary and loading conditions can be plugged into the algorithm without much difficulty. The stability criterion of FD algorithm related to plate problems was also discussed in that study according to the rate of energy propagation of flexural waves. For the modeling of piezoelectric sensors and actuators incorporated in intelligent structures, thorough reviews have been given by Chee *et al*. (1998) and Crawley (1994) and thus will not be repeated here. However, up to the author's knowledge, a combined analytical, numerical and experimental study of the Lamb wave model for a structure with built-in sensors and actuators has not been investigated yet. In the current study, the flexural wave model will be established based on MPT and the coupling effect of sensors/actuators with the plate is taken into consideration. FD algorithm, which is also necessary for the proposed wave signal interpretation method, is chosen to simulate the flexural waves scattered from damages.

1.4 Interpretation methods

Damage identification algorithm is dependent on the methods of generation and reception of Lamb waves. Preliminary methods of interpreting ultrasonic signals are to compare some characteristic parameters between virgin and damaged structures and draw conclusions based on the comparisons (Tan *et al*., 1995; Kundu and Maslov, 1997; Thomas, 1995). These parameters could be wave speed, arrival time, amplitude, attenuation, peaks, etc., either in time domain or in frequency domain. The diagnosis algorithms cover a wide range as well from conventional techniques, such as modal analysis and optimization, to artificial intelligence related techniques, such as expert system, and artificial neural network (ANN), etc. (Alleyne and Cawley, 1992b; Tracy *et al*., 1996). ANN is used for classifying the obtained monitoring information and near real-time diagnosis could be realized once the network has been well trained. With the help of contemporary computation power, the data required to train the neural network could be obtained from numerical simulation, which could save extensive labor of acquiring large amount of experimental data (Takadoya *et al*., 1992). Wavelet transform has attracted much attention recently because it can decompose the dispersive waves into its frequency components and analyze parameters like velocity and attenuation coefficient by a single frequency. It was proven that it also could be used to determine the thickness of the specimen and measure the dispersive curve (Hayashi *et al*., 1999; Kishimoto *et al*., 1995). However, these methods are still based on conventional point to point testing algorithm and do not fully take advantages of the SHM system with distributed sensors/actuators. Further, these methods usually can recognize only the existence of the damages and very limited quantitative information about the damages could be obtained only when a fixed form of damage is assumed *a priori*. Especially, a diagnostic algorithm for distributed damages with arbitrary number and various forms is not available yet. The reason might be that a unique solution usually could not be obtained in this inverse problem of extracting one of system's parameters through system's output. Mathematically speaking, determination of physical condition of a

structure based on the sensor signals with these diagnostic algorithms is an ill-posed, nonlinear inverse problem, for which unique solution can not be obtained even perfect data is given.

Recently, many researchers have attempted to propose methods from either hardware or software prospective to propagate the received reflection waves back to the reflectors (damages), thus to realize quantitative damage identification. The idea is based on that the wave field is reversible (Fink, 1992; Chang and McMechan, 1986). It is also known that based on Huygens' principle, a reflector can be treated as a secondary source (Claerbout, 1985). Thus, if one is able to use sensors to record a complete reflection wave field and find a method to back-propagate the recorded waves, the energy of these waves will progressively converge back to the secondary source and indicates the existence of a reflector. Fink (1993) used up to 128 piezoelectric transducers to generate and receive the sound waves. The wave signals were stored in memories and read backward to constitute a reverse wave field. The reversed waves were then re-emitted to detect the flaws by focusing the waves. By using this so-called time-reversal mirror, Fink could identify a flaw with dimension as small as 0.016 in. The disadvantage of this technique is that it is based on point-by-point testing and might be not applicable in SHM system. Achenbach and his colleagues also used the concept of reversing reflection field in their NDT studies (Deutsch *et al*., 1997). A linear array was used to focus both Raleigh waves and Lamb waves. The time-of-flight was estimated through the cross-correlation of the re-emitted and received signals. The array was self-adjusted by a delay of calculated time-of-flight and the received signals were sent out again to amplify the reflection. By iterative operation of this procedure and switching the element as transmitter, the ultrasonic signals were illustrated numerically and experimentally to be able to focus on an artificial anomaly in the aluminum plate. Comparing these hardware methods, the migration technique actually is a method by use of software to back-propagate the reflection wave.

1.5 Migration concepts

Migration is the computer process that does the reverse (Claerbout, 1985). In Fig. 1.1a, a vertical plane section through the Earth is shown. In geophysical exploration, a wave source (primary source) is exploded on the Earth's surface and the sound reflected from underneath the Earth is recorded by a linear array of geophones (receivers). Migration attempts to form the image of subsurface reflectors by moving or "migrating" the recorded wave field to their actual spatial locations, topology of the Earth's interior. In the oil industry, the migrated image provides information of the Earth's subsurface for geophysicists to decide on prospective locations for hydrocarbon traps. The inverse process deals with back-propagating the recorded waves to obtain geological information (secondary sources) by systematically solving the wave equation as time-dependent boundary value problems based on Huygens' principle. From mathematical viewpoint, identifying the sources, which appear on the right hand side of the wave equation, is a well-posed problem. The migration technique treats the Earth's interior as secondary sources and therefore transfers an ill-posed problem to a well-posed problem which results in a unique solution. Over the past thirty years, research on the migration technique has attained a maturity and is indispensable as an advanced interpretation method for reflection wave field (Claerbout, 1985; Loewenthal *et al*., 1974; Sun and McMechan, 1986; Yilmaz, 1993). In contrast, Fig. 1.1b shows a plate with a linear array of piezoelectric elements. This configuration is an analog to the reflection geophysical prospecting as shown in Fig. 1.1a. These PZT (Lead Zirconate Titanate) disks used in the current study act as actuators and sensors alternately. A source wavelet (voltage) is applied on one of the piezoelectric actuators and induces diagnostic wave signals. If the waves encounter the interface of an inhomogeneity or a damage, they will be reflected, refracted, or diffracted. When the reflection waves hit the PZT disks acting as sensors, the strain change sensed on the piezoelectric sensors will generate a voltage output, which will be amplified and recorded as raw monitoring data. Comparing Fig. 1.1a with b leads to a conclusion that the data acquisition method of an active Lamb wave based SHM system is similar to the data collection method used in geophysics. Migration technique thus could be implemented in SHM to process the recorded wave signals and image the structures and damages, although the area under investigation and the range of

frequency significantly differs between geophysical prospecting and damage identification. The resulting image figuratively reveals the size, the form, location of the damages in the plate, hence the diagnostic algorithms are not needed. In addition, pre-assumption about damage pattern is not required to manipulate the recorded signals, which make detection of distributed multiple damages possible.

In SHM, migration can be applied more robustly than in geophysical prospecting. First of all, in geophysics field, migration is based on *a priori* estimation of the velocity distribution of the Earth's underneath layers, which is a critical prerequisite to obtain correct image through migration. For SHM, it is no longer a concern. Once the study object is targeted, the material properties and structure layout are essentially known, and thus the wave propagation velocity can be accurately predicted. Another advantage is that the actuators and sensors can be distributed at an arbitrary location, which provide more flexibility using migration methods. Further, it is relatively easy in SHM to generate various types of source wavelets and to control the excitation period and different energy transfer direction of the waves, while it is extremely difficult to accommodate them in geophysics field. These characteristics of input wavelet can be properly selected to detect different possible shapes and forms of the damages. Therefore, intelligently choosing these characteristics will make detection much more sensitive. The study objects in SHM and in geophysics or seismology are different, hence some of the data processing procedures in geophysics or seismology field, which are directly related to the Earth, may not be relevant in SHM, such as velocity analysis, residual statics correction, ground roll muffling, etc. However, other procedures, such as deconvolution, Common Middle Point (CMP) sorting, Normal MoveOut (NMO) correction and stacking, which are essential to migration methods, must be adopted when migration is applied to SHM field. Especially, some procedures, such as stacking, whose purpose is to enhance the signal to noise ratio, are always desirable in SHM.

Although migration technique may be a very powerful technique to interpret the reflection wave field recorded from distributed sensors in an active SHM system, it has been studied only by a limited number of researchers. Chien (1997) outlined the

procedure of applying migration in SHM and numerically studied a case of using migration method to image the supposed damage (a big hole) in a plate. The waves in the plate were modeled by CPT and no experimental study was pursued. Liu *et al.* (1996) introduced the migration concept into the NDE of concrete structures. In their studies, a surface crack was *a priori* assumed thus all the imaging process was simplified to find the first arrival time and converted it into the distance by timing the wave propagation velocity.

1.6 Summary

Accordingly, the objective of the thesis is to demonstrate the feasibility of adopting migration technique to interpret ultrasonic Lamb waves generated and received by a structure integrated with actuators and sensors (a linear array) in a smart SHM system, thus realizing quantitative damage identification. Comparing with previous studies, the current study uses a higher-order plate theory, Mindlin plate theory (MPT), to build the mathematical model for analytical analysis and numerical simulation. In addition, not only migration method itself but also many migration related signal processing procedures are also discussed in detail in this study. Most of all, extensive experimental works are pursued to provide a strong support to both the analytical and numerical conclusions obtained from the study.

The main content of this study is covered in Chapter 2 through Chapter 6. In Chapter 2, the aim is to propose a finite difference algorithm for both simulation of the plate wave propagation and the migration. In the first part of Chapter 2, an analytical solution is derived for the transient Lamb waves of an infinite plate subject to a point loading This fundamental solution serves as a benchmark to verify the accuracy of the finite difference solution. Then, a MacCormack 2-6 order finite difference algorithm is presented, and the stability criterion and boundary condition treatment of this algorithm when applied to plate problems are discussed in detail. In Chapter 3, the feasibility of applying poststack migration to image the plate and to detect a single symmetric damage

is studied numerically. The concepts of finite difference reverse-time poststack migration including the relevant data processing procedures are given in this chapter. Also, a one-way version of flexural wave equation is derived followed by a presentation of numerical results about the influence of excitation signals and damage dimensions on the resolution of the migration images. In the first part of Chapter 4, the reverse-time prestack migration process is discussed. Then an excitation-time imaging condition specifically for the migration of waves in a plate is introduced based on ray-tracing concepts and the asymptotic properties of flexural wave velocities. Then, the numerical results are presented to show that two assumed discrete damages are correctly identified through prestack migration. The influence of number of sensors/actuators on the final image of the damage in the plate is also discussed in this section. In Chapter 5, an experimental work is pursued to validate the feasibility of applying migration to process wave signals and identify the structural anomaly. First, an analytical model of wave signals generated/collected by piezoelectric (PZT) actuators/sensors is developed. After the configuration of experimental setup is presented, this chapter shows the signals recorded from the experiment and compares them with the calculation data from the analytical model. Finally, the migration results from the reflection waves of an artificial arc shape damage recorded from the experiment are presented. Chapter 6 summarizes the contributions and conclusions of this study and it also proposes some perspective topics for the future research.

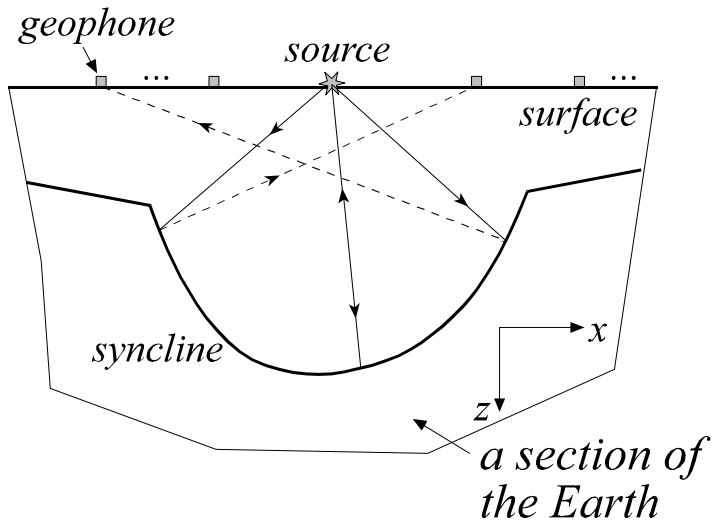

(a)

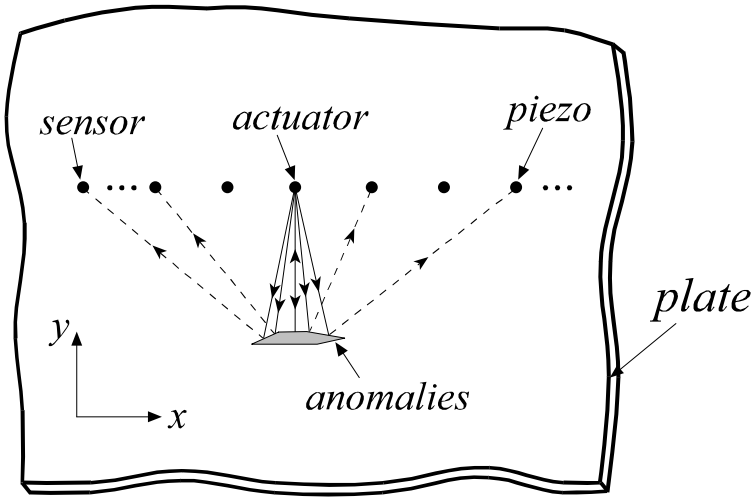

(b)

Fig. 1.1 An analog between geophysical exploration and plate SHM

2 Flexural Waves in a Plate

In the first part of this chapter, an analytical solution is derived for the transient Lamb waves of an infinite plate subject to a point loading. The solution is based on Mindlin plate theory (MPT) and can be simply reduced to the response derived from the classical plate theory (CPT) when both rotary inertia and transverse shear effect are ignored. A MacCormack 2-6 order finite difference algorithm is then presented and the stability criterion and boundary condition treatment of this algorithm when applied to plate problems are discussed in detail. The accuracy of the adopted algorithm is verified by comparing the numerical results with the analytical solution. Thus the finite difference algorithm can be used to simulate the reflection waves and to implement the migration process.

2.1 Mindlin plate theory (MPT) and an analytical solution

2.1.1 Governing equations

Mindlin (1951) proposed an approximation theory for flexural waves in elastic, isotropic plates. By integrating the exact equations of elasticity across the plate thickness and introducing a shear correction factor for the constitutive relations of the transverse shear, the equations of governing the wave motions can be restrained in the two dimensional domain. Assuming u_x and u_y are proportional to z (normal direction to the plate),

$$u_x = z\psi_x(x,y,t), \quad u_y = z\psi_y(x,y,t), \quad u_z = w(x,y,t) \tag{2.1}$$

The equations of motions are then written as:

$$\rho h \frac{\partial^2 w}{\partial t^2} = \frac{\partial Q_x}{\partial x} + \frac{\partial Q_y}{\partial y} + q \tag{2.2a}$$

$$\frac{\rho h^3}{12}\frac{\partial^2 \psi_x}{\partial t^2} = \frac{\partial M_x}{\partial x} + \frac{\partial M_{xy}}{\partial y} - Q_x \tag{2.2b}$$

$$\frac{\rho h^3}{12}\frac{\partial^2 \psi_y}{\partial t^2} = \frac{\partial M_{xy}}{\partial x} + \frac{\partial M_y}{\partial y} - Q_y \tag{2.2c}$$

and the constitutive equations:

$$\begin{Bmatrix} M_x \\ M_y \\ M_{xy} \end{Bmatrix} = D \begin{bmatrix} 1 & \nu & 0 \\ \nu & 1 & 0 \\ 0 & 0 & \frac{1-\nu}{2} \end{bmatrix} \begin{Bmatrix} \frac{\partial \psi_x}{\partial x} \\ \frac{\partial \psi_y}{\partial y} \\ \frac{\partial \psi_x}{\partial y} + \frac{\partial \psi_y}{\partial x} \end{Bmatrix} \tag{2.2d}$$

$$Q_x = \kappa^2 Gh\left(\frac{\partial w}{\partial x} + \psi_x\right) \tag{2.2e}$$

$$Q_y = \kappa^2 Gh\left(\frac{\partial w}{\partial y} + \psi_y\right) \tag{2.2f}$$

Substituting the stress resultants in eqs. (2.2d-f) into eqs. (2.2a-c), the equations of motions in terms of displacement components, w, ψ_x, ψ_y can be obtained. Then, by eliminating ψ_x and ψ_y from three motion equations, a single differential equation for w turns out to be:

$$\left(\nabla^2 - \frac{\rho}{G'}\frac{\partial^2}{\partial t^2}\right)\left(D\nabla^2 - \frac{\rho h^3}{12}\frac{\partial^2}{\partial t^2}\right)w + \rho h\frac{\partial^2 w}{\partial t^2} = \left(1 - \frac{D\nabla^2}{G'h} + \frac{\rho h^2}{12G'}\frac{\partial^2}{\partial t^2}\right)q \tag{2.3}$$

Eq. (2.3) can be used to describe flexural and thickness-shear waves in the plate, and gives an adequate approximation to three dimensional theory under the frequency of lowest antisymmetric thickness-shear mode. If both the transverse shear deformation and rotatory inertia terms are omitted, Eq. (2.3) reduces to the governing equation of CPT, which is only valid to predict the flexural waves for the cases of small wavenumbers and characteristic dimension of a plate much smaller than the wavelength:

$$D\nabla^4 w + \rho h \frac{\partial^2 w}{\partial t^2} = q(x, y, t) \tag{2.4}$$

in which $\nabla^4 = \nabla^2 \nabla^2$. In a polar coordinate system, the displacements are presented as:

$$u_r = z\psi_r(r, \theta, t), \quad u_\theta = z\psi_\theta(r, \theta, t), \quad u_z = w(r, \theta, t) \tag{2.5}$$

and the equations (2.2a-f) could be written as (Mindlin and Deresiewicz, 1954):

$$\frac{\partial M_r}{\partial r} + \frac{1}{r}\frac{\partial M_{r\theta}}{\partial \theta} + \frac{M_r - M_\theta}{r} - Q_r = \frac{\rho h^3}{12}\frac{\partial^2 \psi_r}{\partial t^2} \tag{2.6a}$$

$$\frac{\partial M_{r\theta}}{\partial r} + \frac{1}{r}\frac{\partial M_\theta}{\partial \theta} + \frac{2M_{r\theta}}{r} - Q_\theta = \frac{\rho h^3}{12}\frac{\partial^2 \psi_\theta}{\partial t^2} \tag{2.6b}$$

$$\frac{\partial Q_r}{\partial r} + \frac{1}{r}\frac{\partial Q_\theta}{\partial \theta} + \frac{Q_r}{r} = \rho h \frac{\partial^2 w}{\partial t^2} \tag{2.6c}$$

$$M_r = D[\frac{\partial \psi_r}{\partial r} + \frac{\nu}{r}(\psi_r + \frac{\partial \psi_\theta}{\partial \theta})] \tag{2.6d}$$

$$M_\theta = D[\frac{1}{r}(\psi_r + \frac{\partial \psi_\theta}{\partial \theta}) + \nu \frac{\partial \psi_r}{\partial r}] \tag{2.6e}$$

$$M_{r\theta} = \frac{D}{2}(1-\nu)[\frac{1}{r}(\frac{\partial \psi_r}{\partial \theta} - \psi_\theta) + \frac{\partial \psi_\theta}{\partial r}] \tag{2.6f}$$

$$Q_r = \kappa^2 Gh(\psi_r + \frac{\partial w}{\partial r}) \tag{2.6g}$$

$$Q_\theta = \kappa^2 Gh(\psi_\theta + \frac{1}{r}\frac{\partial w}{\partial \theta}) \tag{2.6h}$$

2.1.2 Analytical solution for infinite plates subject to transient point loading

Applying Fourier transform to eqs. (2.6) with respect to t and considering only axially symmetric motions, it yields

$$\widetilde{M}_r = D(\frac{d}{dr} + \frac{\nu}{r})\widetilde{\psi}_r \tag{2.7a}$$

$$\widetilde{M}_\theta = D(\nu \frac{d}{dr} + \frac{1}{r})\widetilde{\psi}_r \tag{2.7b}$$

$$\widetilde{Q}_r = \kappa^2 Gh(\widetilde{\psi}_r + \frac{d\widetilde{w}}{dr}) \tag{2.7c}$$

$$(\frac{d}{dr} + \frac{1}{r})\widetilde{M}_r - \frac{\widetilde{M}_\theta}{r} - \widetilde{Q}_r = -\frac{\rho\omega^2 h^3}{12}\widetilde{\psi}_r \tag{2.8a}$$

$$(\frac{d}{dr} + \frac{1}{r})\widetilde{Q}_r = -\rho\omega^2 h\widetilde{w} \tag{2.8b}$$

where $\widetilde{g}(r,\omega) = \int_{-\infty}^{+\infty} e^{-i\omega t} g(r,t)dt$, g represents any of the M_r, M_θ, Q_r, ψ_r, and w. Substituting eq. (2.7) into eq. (2.8), the plate equations of motion in terms of displacements are obtained:

$$(\frac{d^2}{dr^2} + \frac{1}{r}\frac{d}{dr} - \frac{1}{r^2} + \frac{\rho\omega^2 h^3}{12D} - \frac{\kappa^2 Gh}{D})\widetilde{\psi}_r - \frac{\kappa^2 Gh}{D}\frac{d\widetilde{w}}{dr} = 0 \tag{2.9}$$

$$(\frac{d}{dr} + \frac{1}{r})\widetilde{\psi}_r + (\frac{d^2}{dr^2} + \frac{1}{r}\frac{d}{dr} + \frac{\rho\omega^2}{\kappa^2 G})\widetilde{w} = 0 \tag{2.10}$$

By eliminating $\widetilde{\psi}_r$ from eq. (2.9) and eq. (2.10), an exclusive equation for transverse displacement $\widetilde{w}$ is obtained:

$$(\nabla^4 + A\nabla^2 + B)\widetilde{w}(r,\omega) = 0 \tag{2.11}$$

where $\nabla^2 = \frac{d^2}{dr^2} + \frac{1}{r}\frac{d}{dr}$, and

$$A = (\frac{\rho h^3}{12D} + \frac{\rho}{\kappa^2 G})\omega^2,\ B = (\frac{\rho^2 h^3}{12\kappa^2 GD}\omega^2 - \frac{\rho h}{D})\omega^2$$

Assuming the input frequency is lower than the cutoff frequency, $\omega \le (2\kappa/h)\sqrt{3G/\rho}$, the solution is only composed of one propagating wave. In this case, B is negative. Defining two positive real wave numbers k_1 and k_2,

$$k_1^2 = (\sqrt{A^2 - 4B} + A)/2\,,\ k_2^2 = (\sqrt{A^2 - 4B} - A)/2$$

eq. (2.11) can be transformed into

$$(\frac{d^2}{dr^2} + \frac{1}{r}\frac{d}{dr} + k_1^2)(\frac{d^2}{dr^2} + \frac{1}{r}\frac{d}{dr} - k_2^2)\widetilde{w} = 0 \tag{2.12}$$

The complete solutions of eq. (2.12) should include the solutions of both a standard Bessel equation

$$\frac{d^2\widetilde{w}}{dr^2} + \frac{1}{r}\frac{d\widetilde{w}}{dr} + k_1^2\widetilde{w} = 0 \tag{2.13a}$$

and a modified Bessel equation

$$\frac{d^2\widetilde{w}}{dr^2} + \frac{1}{r}\frac{d\widetilde{w}}{dr} - k_2^2\widetilde{w} = 0 \tag{2.13b}$$

For the outward propagating waves generated by a point impact, the solution can be best expressed as

$$\widetilde{w} = C_1 H_0^{(2)}(k_1 r) - C_2 H_0^{(2)}(-ik_2 r) \tag{2.14}$$

where $H_0^{(2)}$ are Hankel functions of the second kind of order 0, C_1, C_2 are constants which will be determined by the boundary conditions and the initial conditions. By use of the asymptotic property of Hankel function with a small argument

$$H_0^{(2)}(r) \approx -\frac{2i}{\pi}\ln(r) \qquad \text{as } r \to 0 \tag{2.15}$$

it can be observed that in order to satisfy the requirement of finite displacement at the origin $r = 0$, C_1, C_2 must be equal. Thus, the solution of $\widetilde{w}$ is expressed as

$$\widetilde{w} = C[H_0^{(2)}(k_1 r) - H_0^{(2)}(-ik_2 r)] \tag{2.16}$$

in which the constant C can be determined by the applied loading condition.

By differentiating eq. (2.10) with respect to r and subtracting the result from eq. (2.9), $\widetilde{\psi}_r$ is written in terms of $\widetilde{w}$,

$$\widetilde{\psi}_r = \frac{\rho\omega^2}{\kappa^2 GB}\frac{d}{dr}[\frac{d^2}{dr^2} + \frac{1}{r}\frac{d}{dr} + A - \frac{\kappa^2 GB}{\rho\omega^2}]\widetilde{w} \tag{2.17}$$

Then substituting eq. (2.17) into eq. (2.7c) leads to

$$\widetilde{Q}_r = \frac{\rho h\omega^2}{B}[\frac{d^3}{dr^3} + \frac{1}{r}\frac{d^2}{dr^2} + (A - \frac{1}{r^2})\frac{d}{dr}]\widetilde{w} \tag{2.18}$$

Replacing $\widetilde{w}$ with eq. (2.16) and expanding eq. (2.18) by use of recurrence relations of Bessel functions:

$$2\frac{dH_n^{(2)}(z)}{dz} = H_{n-1}^{(2)}(z) - H_{n+1}^{(2)}(z) \text{ and } H_n^{(2)} = (-1)^n H_{-n}^{(2)} \tag{2.19}$$

Eq. (2.18) can be explicitly written as

$$\widetilde{Q}_r = \frac{\rho h\omega^2 C}{B}\frac{d}{dr}[(A - k_1^2)H_0^{(2)}(k_1 r) + (A - k_2^2)H_0^{(2)}(-ik_2 r)] \tag{2.20}$$

Assuming the point force $\widetilde{q}(\omega)$ is distributed evenly on an infinite small circular area with $r = r_0$, then by the equilibrium relation of the shear force

$$\widetilde{q}(\omega) = 2\pi r_0 \widetilde{Q}|_{r=r_0} \tag{2.21}$$

The constant C can be evaluated by

$$C = \frac{iB\widetilde{q}}{4\rho h\omega^2(k_1^2 + k_2^2)} \tag{2.22}$$

Considering a very thin plate (Kirchhoff plate), for which the transverse shear and rotatory inertia can be ignored, i.e., $A = 0$ and $k_1^2 = k_2^2 = k^2 = B$, the solution eq. (2.16) is reduced to a solution for CPT governed by eq. (2.4):

$$\widetilde{w} = \frac{-i\widetilde{q}}{8Dk^2}[H_0^{(2)}(kr) - H_0^{(2)}(-ikr)] \tag{2.23}$$

The transverse displacement w can be obtained by inverse Fourier transform of eq. (2.16) and (2.23).

2.1.3 Comparisons of solutions based on MPT with CPT

The derived solution is first compared with the widely accepted Medick's CPT solution (Medick, 1961), for the purpose of showing that the current reduced solution eq. (2.23) for CPT is consistent with Medick's solution. The time history of the point force was given by

$$q(r=0,t)=P[H(t)-H(t-\beta)] \tag{2.24}$$

where $H(t)$ is Heaviside step function and $\beta = 10\mu s$. The waveform of the load ($P = 1\,lb$) and corresponding frequency spectrum are given in Figs. 2.1a and 2.1b, respectively. The transverse displacement of Medick's solution is given by

$$w(r,t)=\begin{cases} \dfrac{Pt}{4\pi\sqrt{\rho hD}}M\left(\sqrt{\dfrac{\rho h}{D}}\dfrac{r^2}{4t}\right) & 0<t\le\beta \\ \dfrac{P}{4\pi\sqrt{\rho hD}}\left\{tM\left(\sqrt{\dfrac{\rho h}{D}}\dfrac{r^2}{4t}\right)-(t-\beta)M\left(\sqrt{\dfrac{\rho h}{D}}\dfrac{r^2}{4(t-\beta)}\right)\right\} & t>\beta \end{cases} \tag{2.25}$$

where $M(x)$ is defined as $M(x)=\pi/2-Si(x)-\sin x+xCi(x)$, and $Si(x)$ and $Ci(x)$ are the sine and cosine integrals, respectively. Transverse displacement w for both solutions are normalized by

$$\overline{w}(r,t)=\frac{w(r,t)}{P\beta/(4\pi\sqrt{\rho hD})} \tag{2.26}$$

In the calculation, the material is chosen as an Al-6061 plate with $h = 0.063\,in.$, $E = 10523\text{Ksi.}$, $\nu = 0.3$, $\rho = 0.098\,lb./\text{in.}^3$. It is known that Mindlin plate theory (MPT) can be reduced to classical plate theory (CPT) when rotatory inertia and transverse shear effects are neglected. It is also expected that Mindlin plate theory solution should be close to CPT solution for low frequency signals, i.e., large wavelength λ comparing with plate thickness h, where Kirchhoff's assumptions are satisfied. Fig. 2.2 shows good agreement between current CPT solution reduced from Mindlin plate theory and Medick's CPT solution for entire period of time. Fig. 2.3 clearly displays the difference between these two approximation theories. For long times, Mindlin plate theory gives

close results as those by classical plate theory. However, for short times in which the signal is dominated by high frequency components, the result shows a discrepancy between two solutions. Further Mindlin solution shows a delay in phase and an increase in amplitude comparing with the classical plate theory. This can be explained by knowing that the inertia term in the equation will bring phase lag and transverse shear deformation will amplify the transverse displacement.

Next to demonstrate the influence of high frequency components in the signals on these two solutions more clearly, the response of a load of sinusoid modulation function was calculated. The loading history is given by

$$q(r=0,t)=P\,[H(t)-H(t-N_p/f_0)]\,(1-\cos\frac{2\pi f_0 t}{N_p})\sin 2\pi f_0 t \tag{2.27}$$

where $N_p=5$ and $P=1lb$. The waveform of the load (f_0 = 100kHz) and corresponding frequency spectrum are given in Figs. 2.4a and 2.4b, respectively. It can be noticed that the energy of this narrow banded signal is concentrated around the central frequency f_0, which makes it possible to evaluate the wavelength λ in terms of f_0 quantitatively based on the dispersion relation.

Fig. 2.5 gives the solutions of MPT and CPT when the plate is subjected to the point load governed by eq. (2.27). It is well known that only when the wavelength is 10 times larger than the plate thickness, classical plate theory will agree well with both exact elasticity solution and MPT. As it can be observed from Fig. 2.5a, when the central frequency is 10kHz, which corresponds to wavelength $\lambda \approx 24.6h$, the solutions based on MPT and CPT match very well. It means that at this range using classical plate theory to approximate the elasticity solution is reasonable. In Fig. 2.5b, where central frequency is 100kHz, which corresponds to wavelength $\lambda \approx 7.4h$, CPT departs distinctly from MPT. This implies that in high frequency range the effect of rotary inertia and transverse shear deformation has to be taken into account. When ultrasonic testing technique is adopted in SHM applications, the order of applicable frequencies ranges from kHz to MHz. Thus, it is inevitable to use MPT or higher order approximation theory to model the problem.

2.2 Finite difference algorithm for simulating the waves

2.2.1 A 2-6 order MacCormack algorithm

Defining

$$\mathbf{u}^T = \{\dot{w},\ \dot{\psi}_x,\ \dot{\psi}_y,\ Q_y,\ Q_x,\ M_x,\ M_y,\ M_{xy}\} \tag{2.28a}$$

$$\mathbf{q}^T = \{q,\ 0,\ 0,\ 0,\ 0,\ 0,\ 0,\ 0\} \tag{2.28b}$$

and differentiating eq. (2.2d-f), the system of eq. (2.2) can be rewritten as a first-order system equations in matrix form:

$$\mathbf{E}_0 \frac{\partial \mathbf{u}}{\partial t} = \mathbf{A}_0 \frac{\partial \mathbf{u}}{\partial x} + \mathbf{B}_0 \frac{\partial \mathbf{u}}{\partial y} + \mathbf{C}_0 \mathbf{u} + \mathbf{q} \tag{2.29}$$

where

$$\mathbf{E}_0 = \begin{bmatrix} \rho h & 0 & 0 & 0 & 0 & 0 & 0 & 0 \\ 0 & \frac{\rho h^3}{12} & 0 & 0 & 0 & 0 & 0 & 0 \\ 0 & 0 & \frac{\rho h^3}{12} & 0 & 0 & 0 & 0 & 0 \\ 0 & 0 & 0 & \frac{1}{\kappa^2 G h} & 0 & 0 & 0 & 0 \\ 0 & 0 & 0 & 0 & \frac{1}{\kappa^2 G h} & 0 & 0 & 0 \\ 0 & 0 & 0 & 0 & 0 & \frac{1}{(1-\nu^2)D} & -\frac{\nu}{(1-\nu^2)D} & 0 \\ 0 & 0 & 0 & 0 & 0 & -\frac{\nu}{(1-\nu^2)D} & \frac{1}{(1-\nu^2)D} & 0 \\ 0 & 0 & 0 & 0 & 0 & 0 & 0 & \frac{2}{(1-\nu)D} \end{bmatrix}$$

$$\mathbf{A}_0 = \begin{bmatrix} 0 & 0 & 0 & 0 & 1 & 0 & 0 & 0 \\ 0 & 0 & 0 & 0 & 0 & 1 & 0 & 0 \\ 0 & 0 & 0 & 0 & 0 & 0 & 0 & 1 \\ 0 & 0 & 0 & 0 & 0 & 0 & 0 & 0 \\ 1 & 0 & 0 & 0 & 0 & 0 & 0 & 0 \\ 0 & 1 & 0 & 0 & 0 & 0 & 0 & 0 \\ 0 & 0 & 0 & 0 & 0 & 0 & 0 & 0 \\ 0 & 0 & 1 & 0 & 0 & 0 & 0 & 0 \end{bmatrix} \quad \mathbf{B}_0 = \begin{bmatrix} 0 & 0 & 0 & 1 & 0 & 0 & 0 & 0 \\ 0 & 0 & 0 & 0 & 0 & 0 & 0 & 1 \\ 0 & 0 & 0 & 0 & 0 & 0 & 1 & 0 \\ 1 & 0 & 0 & 0 & 0 & 0 & 0 & 0 \\ 0 & 0 & 0 & 0 & 0 & 0 & 0 & 0 \\ 0 & 0 & 0 & 0 & 0 & 0 & 0 & 0 \\ 0 & 0 & 1 & 0 & 0 & 0 & 0 & 0 \\ 0 & 1 & 0 & 0 & 0 & 0 & 0 & 0 \end{bmatrix} \quad \mathbf{C}_0 = \begin{bmatrix} 0 & 0 & 0 & 0 & 0 & 0 & 0 & 0 \\ 0 & 0 & 0 & 0 & -1 & 0 & 0 & 0 \\ 0 & 0 & 0 & -1 & 0 & 0 & 0 & 0 \\ 0 & 0 & 1 & 0 & 0 & 0 & 0 & 0 \\ 0 & 1 & 0 & 0 & 0 & 0 & 0 & 0 \\ 0 & 0 & 0 & 0 & 0 & 0 & 0 & 0 \\ 0 & 0 & 0 & 0 & 0 & 0 & 0 & 0 \\ 0 & 0 & 0 & 0 & 0 & 0 & 0 & 0 \end{bmatrix}$$

Further defining $\mathbf{U} = \mathbf{E}_0\mathbf{u}$, $\mathbf{A}_t = \mathbf{A}_0\mathbf{E}_0^{-1}$, $\mathbf{B}_t = \mathbf{B}_0\mathbf{E}_0^{-1}$, $\mathbf{C}_t = \mathbf{C}_0\mathbf{E}_0^{-1}$, eq. (2.29) can be rewritten as

$$\frac{\partial \mathbf{U}}{\partial t} = \mathbf{A}_t \frac{\partial \mathbf{U}}{\partial x} + \mathbf{B}_t \frac{\partial \mathbf{U}}{\partial y} + \mathbf{C}_t\mathbf{U} + \mathbf{q} \tag{2.30}$$

In modeling the damage as a region of inhomogeneity in the plate, only the property matrix $\mathbf{E}_0$ needs to be altered in the above governing equations, which will make the modeling of scattering problem much easier in the numerical calculation. Considering the major portion of eq. (2.30)

$$\frac{\partial \mathbf{U}}{\partial t} = \mathbf{A}_t \frac{\partial \mathbf{U}}{\partial x} + \mathbf{B}_t \frac{\partial \mathbf{U}}{\partial y} \tag{2.31}$$

since $\mathbf{E}_0$ is independent of time and spatial coordinates and $\mathbf{A}_0$, $\mathbf{B}_0$ is not dependent on the spatial coordinates, then $\mathbf{A}_t$ and $\mathbf{B}_t$ are not dependent on spatial coordinates. Eq. (2.31) can be rewritten in a divergence-free form:

$$\mathbf{U}_t = \mathbf{f}_x + \mathbf{g}_y \tag{2.32}$$

where $\mathbf{f}$ and $\mathbf{g}$ are $\mathbf{A}_t\mathbf{U}$ and $\mathbf{B}_t\mathbf{U}$ respectively. Subscripts x, y and t represent the derivatives with respect to these variables. A MacCormack explicit finite difference algorithm is used to solve this two-dimensional wave equation. In each time step Δt, this algorithm updates eq. (2.32) by first solving the equation in the x direction ($\mathbf{U}_t = \mathbf{f}_x$) and then in the y-direction ($\mathbf{U}_t = \mathbf{g}_y$), thus the algorithm is a dimensional splitting method and has a smaller phase error than unsplit schemes.

The dimensional splitting method is facilitated first in the x dimension by defining F_x as a backward-forward operator for one-dimensional problem $\mathbf{U}_t = \mathbf{A}_t\mathbf{U}_x$, which includes a predictor $\mathbf{U}_{i,j}^{(1)}$ and a corrector $\mathbf{U}_{i,j}^{(n+1/2)}$ shown in the following:

<u>predictor</u>

$$\mathbf{U}_{i,j}^{(1)} = \mathbf{U}_{i,j}^{(n)} + \frac{\Delta t}{30\Delta x}[37(\mathbf{f}_{i,j}^{(n)} - \mathbf{f}_{i-1,j}^{(n)}) - 8(\mathbf{f}_{i-1,j}^{(n)} - \mathbf{f}_{i-2,j}^{(n)}) + (\mathbf{f}_{i-2,j}^{(n)} - \mathbf{f}_{i-3,j}^{(n)})] \tag{2.33a}$$

corrector

$$\mathbf{U}_{i,j}^{(n+1/2)} = \frac{1}{2}(\mathbf{U}_{i,j}^{(n)} + \mathbf{U}_{i,j}^{(1)}) + \frac{\Delta t}{60\Delta x}[37(\mathbf{f}_{i+1,j}^{(1)} - \mathbf{f}_{i,j}^{(1)}) - 8(\mathbf{f}_{i+2,j}^{(1)} - \mathbf{f}_{i+1,j}^{(1)}) + (\mathbf{f}_{i+3,j}^{(1)} - \mathbf{f}_{i+2,j}^{(1)})] \quad (2.33b)$$

and defining F_x^+ as a forward-backward operator for $\mathbf{U}_t = \mathbf{A}_t\mathbf{U}_x$ with the following predictor and corrector:

predictor

$$\mathbf{U}_{i,j}^{(1)} = \mathbf{U}_{i,j}^{(n)} + \frac{\Delta t}{30\Delta x}[37(\mathbf{f}_{i+1,j}^{(n)} - \mathbf{f}_{i,j}^{(n)}) - 8(\mathbf{f}_{i+2,j}^{(n)} - \mathbf{f}_{i+1,j}^{(n)}) + (\mathbf{f}_{i+3,j}^{(n)} - \mathbf{f}_{i+2,j}^{(n)})] \quad (2.33c)$$

corrector

$$\mathbf{U}_{i,j}^{(n+1/2)} = \frac{1}{2}(\mathbf{U}_{i,j}^{(n)} + \mathbf{U}_{i,j}^{(1)}) + \frac{\Delta t}{60\Delta x}[37(\mathbf{f}_{i,j}^{(1)} - \mathbf{f}_{i-1,j}^{(1)}) - 8(\mathbf{f}_{i-1,j}^{(1)} - \mathbf{f}_{i-2,j}^{(1)}) + (\mathbf{f}_{i-2,j}^{(1)} - \mathbf{f}_{i-3,j}^{(1)})] \quad (2.33d)$$

where the two indices (i, j) in the subscript represent the x and y direction grid ($i, j \in [0, M]$, M is the maximum grid index) and the index (n) in the superscript represents the time step ($n \in [0, N]$, N is the maximum time step index). Next in the y direction replacing **f** by **g** and reversing the role of indices i and j in eq. (2.33), defining the backward-forward operator F_y and forward-backward operator F_y^+ for one-dimensional problem $\mathbf{U}_t = \mathbf{B}_t\mathbf{U}_y$, then the MacCormack splitting method can be expressed as

$$\mathbf{U}^{n+2} = F_x F_y F_y^+ F_x^+ \mathbf{U}^n \quad (2.34)$$

$\mathbf{U}^n$ is the output value of the nth time step and $\mathbf{U}^{n+2}$ is for the $(n+2)^{\text{th}}$ time step. Each operator proceeds the calculation by a half time step; thus a complete update includes four operators in two time steps. In each sequential time step, the order of the x and y direction updates is reversed, so is the order of forward-backward and backward-forward operators. In this operation, the MacCormack algorithm acquires second-order accuracy in time and sixth-order accuracy in space (referred to 2-6 scheme), which is modified from a 2-4 order algorithm proposed by Bayliss *et al*. (1986) and Gottlieb and Turkel

(1976).

For the term $\frac{\partial \mathbf{U}}{\partial t} = \mathbf{C}_t \mathbf{U}$ in eq. (2.30), the increment of $\mathbf{U}$ due to $\mathbf{C}_t$ is calculated in advance by $\Delta \mathbf{U}_{i,j}^{(n)} = e^{\mathbf{C}_t \Delta t}$, and then at each time step this term is added into each grid point. This method avoids the difference computation at each time step, thus speeds up the calculation. If the plate is subjected to a distributed transverse loading, the $\mathbf{q}$ term in eq. (2.30) can be counted into the numerical results by inserting the amplitude into the iteration at each time step as a boundary condition. For a point force with amplitude P, which is desired in migration technique, the force term $\mathbf{q}$ with $q = P / \Delta A$ is applied as a distributed force on a very small area ΔA to simulate the loading. Because these two terms are independent of spatial grid, they are updated after the splitting computation of eq. (2.31) and summed into the result after each time step of finite difference calculation.

2.2.2 Treatment of the boundaries

In the analysis of geophysics problems using finite difference method, three unbounded edges of the computation domain must be truncated by artificial boundaries to render the computational domain finite. These boundaries can be constructed as absorbing boundaries, while the surface of the Earth is treated as a free boundary. By using absorbing boundaries from which the artificial reflection in the calculation is minimized, a problem with infinite media can be modeled in finite computation dimensions. In the current study, the plate is assumed to be infinite in the *x*-*y* plane (free edges) to circumvent the complexity of the reflection waves from the edges of the plate. Thus, absorbing boundary conditions (ABC) need to be applied to all the edges of the plate. The one-dimensional absorbing boundary with anisotropic filtering (AF) effect proposed by Dai *et al*. (1993) is adopted in this study. Another approach using Perfectly Matched Layer (PML) for mesh truncation with finite element methods in electromagnetic wave propagation problems governed by full-wave Maxwell's equations has being actively pursued (e.g. Kuzuoglu and Mittra, 1999).

A transition strip near the four edges of the plate, as the shaded area shown in Fig.

2.6, is secluded to construct the anisotropic filter. The AF is used to adjust the material constants of the plate (i.e., material property matrix $\mathbf{E}_0$ in eq. 2.29) so that the directivity of the outgoing waves in the strip will change gradually to the normal direction with respect to the edges. For the bottom edge of the plate ($y = -N \times \Delta y / 2$), the desired direction of the waves is in the negative y direction, thus the wave equation in the transition strip is modified and expressed as

$$\frac{\partial \mathbf{U}}{\partial t} = m(y)\mathbf{A}_t \frac{\partial \mathbf{U}}{\partial x} + \mathbf{B}_t \frac{\partial \mathbf{U}}{\partial y} + m(y)\mathbf{C}_t \mathbf{U} + \mathbf{q} \tag{2.35}$$

where

$$m(y) = \frac{1}{2} + \frac{1}{2}\cos\frac{i_a \pi}{N_a}, \qquad (i_a = 1, 2, ..., N_a)$$

and N_a refers to the grid number of the transition strip or the absorbing boundary (Fig. 2.6). The characteristic velocities in the x direction are related to the eigenvalues of the matrix $m(y)\mathbf{A}_t$. As the horizontal grid lines approach the bottom edge, $m(y)$ approaches zeroes, so do the x direction characteristic velocities. Therefore, at the bottom edge only the negative y-direction waves exist and the wavefront of the waves becomes a straight line. Then the one-dimensional absorbing boundary condition is applied so that the amplitude of the reflection of the normal incidence waves from the artificial edges could be reduced effectively. Absorbing boundaries can be applied to the top edge and two vertical edges in a similar way.

Besides absorbing boundary conditions, two other kinds of boundary treatments must be taken into consideration. The first one is so-called calculation domain boundary conditions. These conditions are required to find extra grid points so that the proposed finite difference algorithm is able to complete the calculation of the points near the boundaries. A fourth-order extrapolation from the interior points is executed to determine the points near the boundaries in the current algorithm. In the forward space scheme, the points (i, j = 0, 1, 2) are calculated by:

$$u_{i,j}^{(1)} = 5u_{i+1,j}^{(1)} - 10u_{i+2,j}^{(1)} + 10u_{i+3,j}^{(1)} - 5u_{i+4,j}^{(1)} + u_{i+5,j}^{(1)} \tag{2.36a}$$

$$u_{i,j}^{(n+1/2)} = 5u_{i+1,j}^{(n+1/2)} - 10u_{i+2,j}^{(n+1/2)} + 10u_{i+3,j}^{(n+1/2)} - 5u_{i+4,j}^{(n+1/2)} + u_{i+5,j}^{(n+1/2)} \tag{2.36b}$$

for the predictor and corrector, respectively. In the backward-space scheme, the points (i, $j = M$, M-1, M-2) are calculated by:

$$u_{i,j}^{(1)} = 5u_{i-1,j}^{(1)} - 10u_{i-2,j}^{(1)} + 10u_{i-3,j}^{(1)} - 5u_{i-4,j}^{(1)} + u_{i-5,j}^{(1)} \tag{2.37a}$$

$$u_{i,j}^{(n+1/2)} = 5u_{i-1,j}^{(n+1/2)} - 10u_{i-2,j}^{(n+1/2)} + 10u_{i-3,j}^{(n+1/2)} - 5u_{i-4,j}^{(n+1/2)} + u_{i-5,j}^{(n+1/2)} \tag{2.37b}$$

The other boundary treatment is the implementation of physical boundary conditions. Eq. (2.30) shows that the physical boundary conditions about **u** are applied in the algorithm through **U**. Based on $\mathbf{U} = \mathbf{E}_0\mathbf{u}$, if values of the variables at the boundary are zero, the real constraints about $\dot{w}$, $\dot{\psi}_x$, $\dot{\psi}_y$, Q_x, Q_y, M_{xy} can be plugged directly into the calculation. If the values are non-zero, the corresponding constant factors are applied respectively. To solve eq. (2.30), besides the initial conditions of w, ψ_x, ψ_y and their derivatives throughout the plate, three boundary conditions must be given on each edge of the plate. However, the finite difference calculation based on eq. (2.30) requires all the eight variables of **U** be given to proceed the calculation. Otherwise, the calculation may become unstable which has been observed in our study. Thus, at the edges or boundaries of the plate, other linear independent relations must be introduced to calculate the values of other five variables from the three given physical boundary conditions. Gottlieb, *et al*. (1982) demonstrated that to guarantee the convergence of the algorithm, these relations could be chosen as the characteristic variables that propagate toward the boundary. Bayliss *et al*. (1986) also used this method to model the free surfaces in their problem. This method is tested in the current simulation. However, the algorithm becomes unstable. The reason might be that this method of boundary treatment could not be used in the cases with high frequency signals.

2.2.3 Stability and accuracy criteria

Although the explicit finite-difference scheme is computationally much more

efficient than the implicit scheme, it is restricted by CFL (Courant-Friedrichs-Lewy) stability condition, assuming that the waves are not allowed to propagate over two grids in just a single time step. In this case the properties of the waves could be reserved in the numerical approximation and the stability is guaranteed. It requires the numerical propagation speed $\Delta x/\Delta t$ to be less than the fastest propagation wave speed. For the MacCormack scheme, the time step is limited by

$$\Delta t < \frac{2\min(\Delta x, \Delta y)}{3C_{\max}} \tag{2.38}$$

where $min(\Delta x, \Delta y)$ means selecting a smaller value between the x-direction grid space Δx and y-direction grid space Δy, C_{max} is the maximum velocity of all wave components. Three characteristic velocities for flexural wave can be listed as:

$$C_0 = \sqrt{\frac{2}{1-\nu}}\sqrt{\frac{G}{\rho}} = \sqrt{\frac{E}{\rho(1-\nu^2)}} \tag{2.39a}$$

$$C_S = \sqrt{\frac{G}{\rho}} = \sqrt{\frac{E}{2\rho(1+\nu)}} \tag{2.39b}$$

$$C_R = \kappa\sqrt{\frac{G}{\rho}} \tag{2.39c}$$

and the dilatational wave velocity is

$$C_P = \sqrt{\frac{E(1-\nu)}{\rho(1+\nu)(1-2\nu)}} \tag{2.39d}$$

Among these velocities, C_P is the maximum. Because the energy and disturbance travel with the group velocity, which is bounded by the dilatational wave velocity, it is conservative to choose $C_{max} = C_P$ (Assadi-Lamouki and Krauthammer, 1989), and the CFL condition of MacCormack algorithm for the Mindlin plate problem is formed as

$$\Delta t \le \frac{2 \cdot \min(\Delta x, \Delta y)}{\sqrt{\frac{9E(1-\nu)}{\rho(1+\nu)(1-2\nu)}}} \tag{2.40}$$

It is advisable to choose $\Delta t^2 = \max(\Delta x^6, \Delta y^6)$ so that the accuracy of this algorithm will not be dominated only either by the second order truncation error in time $O(\Delta t^2)$ or by the sixth order error in space $O(\Delta x^6)$. Usually, Δx and Δy choose the same value ($\Delta x = \Delta y = \Delta s$). It follows from eq. (2.40) that the optimum grid space can be estimated as

$$\Delta s^2 = \sqrt{\frac{2(1-2\nu)}{9(1-\nu)}} \Big/ C_s \tag{2.41}$$

The dispersion effect of the flexural waves also should be taken into consideration in choosing the calculation parameters like grid space and time step. For Mindlin plate theory described in eq. (2.3), by setting the external load q to zero and assuming a straight crested wave (plane wave), it is found that the phase velocity C is related to wavenumber γ as in the dispersion relation:

$$\gamma = \frac{\pi}{h} \frac{C_S C}{\sqrt{(\kappa^2 C_S^2 - C^2)(C_0^2 - C^2)}} \tag{2.42}$$

The frequency f of interest then is related to the plate thickness as

$$4h^2 \left(\frac{\kappa^2 C_S^2}{\lambda^2} - f^2 \right) \left(\frac{C_0^2}{\lambda^2} - f^2 \right) = C_S^2 f^2 \tag{2.43}$$

To preserve the propagation properties of waves at significant frequencies, $\Delta s \le \lambda / 10$ should be chosen to assure the error to be less than 1% (Balasubramanyam *et al*., 1996). Thus a maximum value of grid space can be drawn from eq. (2.43):

$$\Delta s = \left(\frac{h^2(\kappa^2 C_S^2 + C_0^2)}{50(4h^2 f^2 - C_S^2)} + \frac{h}{50 f} \sqrt{\frac{\kappa^2 C_S^4 (\kappa^2 h^2 f^2 + C_0^2) + h^2 f^2 C_0^2 (C_0^2 - 2\kappa^2 C_S^2)}{(4h^2 f^2 - C_S^2)^2}} \right)^{1/2} \tag{2.44}$$

Combining eq. (2.41) and eq. (2.44), and defining $\eta = 100\sqrt{2(1-2\nu)/(1-\nu)}/3$, it gives the center frequency f_0 around which the 2-6 order scheme will give the best accuracy:

$$f_0 = \left(\frac{\kappa^2 C_S^2 + C_0^2}{2\eta} + \frac{C_S}{8h^2} \pm \sqrt{\left(\frac{\kappa^2 C_S^2 + C_0^2}{2\eta} + \frac{C_S}{8h^2} \right)^2 - \left(\frac{\kappa C_S C_0}{\eta} \right)^2} \right)^{1/2} \sqrt{C_S} \quad (2.45)$$

In other words, it is advisable to choose center frequency f_0 according to eq. (2.45) when constructing source wavelet for the numerical simulation. For classic thin plate theory governed by eq. (2.4), a similar derivation gives a much simpler form

$$f_0 = \frac{6\kappa h}{\sqrt{1-2\nu}} \left(\frac{C_S}{10} \right)^2 \quad (2.46)$$

The frequency range of interest is also bounded by the cut-off frequency of lowest mode thickness shear waves. Assuming the displacement is

$$\psi_x = e^{iwt}, \quad w = \psi_y = 0 \quad (2.47)$$

Substituting (2.47) into eq. (2.3), the cut-off frequency f_c of the lowest mode thickness shear waves is obtained:

$$f_c = \frac{\kappa}{\pi h} \sqrt{\frac{3G}{\rho}} \quad (2.48)$$

Eq. (2.48) shows that the thicker the plate is, the lower frequency information the waves in the plate can propagate. In other words, the product of frequency timing thickness ($f \cdot h$) gives a limitation of discussing plate waves using Mindlin plate theory. For an Al-6061 plate (E = 10Msi, ν = 0.35), this product is about $60 KHz \cdot in$.

To verify the accuracy of the finite difference (FD) algorithm, the FD calculation results are compared with the results based on the derived analytical solution, as shown in Fig. 2.7. From eq. (2.38) it is clear that the accuracy of finite difference simulation is highly dependent on the wavelength of the propagating waves. In this case, the grid space is chosen as $\Delta s = 0.02 in.$. In Fig. 2.7a, the central frequency is 20kHz, corresponding to the wavelength $\lambda \approx 17.3h$. This satisfies the requirement that the wavelength should be 10 times smaller than the grid spacing, thus the finite difference result agrees well with the analytical solution. As expected, increasing the central frequency, while the grid

space remains unchanged, will decrease the calculation accuracy. This can be observed in Fig. 2.7b, when the central frequency is 100kHz, corresponding to the wavelength $\lambda \approx 7.4h$, the error between two solutions can be clearly recognized. It can be concluded based on Fig. 2.7 that the constructed finite difference algorithm is capable of simulating the flexural waves accurately.

2.3 Reflection wave field

Fig. 2.6 shows the geometry of the plate in the finite difference calculation. In the figure, N is the grid number for both x-direction and y-direction including the absorbing boundary, N_a is the grid number for absorbing boundary, $2N_s+1$ is the number of sensors at which the wave field is recorded. To generate the reflection wave field scattered by multiple damages in a plate, the plate is viewed as inhomogeneous materials. Each damage is modeled as a small region of the plate with different material constants. This can be implemented simply by altering the matrix $\mathbf{E}_0$ in eq. (2.30) without affecting the kernel codes of the finite difference program. By using this approach, the boundary conditions at the interfaces between the plate and damages are implicitly satisfied, which makes it easier to model damages with complicated geometry and material properties.

Fig. 2.8 gives a synthesized reflection wave field of a damage with rectangular shape. The modeled square plate has a side length 72 in. The absorbing boundary is 4 in. along each side of the plate. The plate including the absorbing boundary is modeled by 200×200 finite difference mesh with uniform spacing $\Delta x = \Delta y = 0.4$ in. ($N = 200$, $N_a = 10$). The 161 piezoelectrics are located at $y = 0$ and $-32 \le x \le 32$ in. with uniform spacing $\Delta x = 0.4$ in. ($N_s = 80$). The aluminum 6061-T6 has the following material properties: $E = 10$ Msi, $\nu = 0.35$, $\rho = 0.008$ lb/in^3. The plate thickness is 1 in. The damage area is modeled as a material with one-eighth value of the bending stiffness for the plate. In this figure, the amplitude of the velocity of transverse deformation ($\dot{w}$) is shown as a contour plot. The value scale shown on the color-bar represents the real value of the velocity multiplied by $5.6\times10^6/\rho h$ (in./s). The abscissa represents the position of sensors, while

the ordinate represents the propagating time of the waves. The damage has a rectangular shape as shown in Fig. 2.6. Two cases are given with different damage sizes, 40×0.8 (unit in inches) in Fig. 2.8a and 10×5 in Fig. 2.8b, respectively. Both damages have a center located at (0, -16). The waves are excited from an actuator at (10, 0) with a source wavelet that contains half cycle of a sine function (f_0 = 40kHz). In the figure, the incident waves have already been muted by subtracting the wave field without damage from the total reflection wave field of the damage.

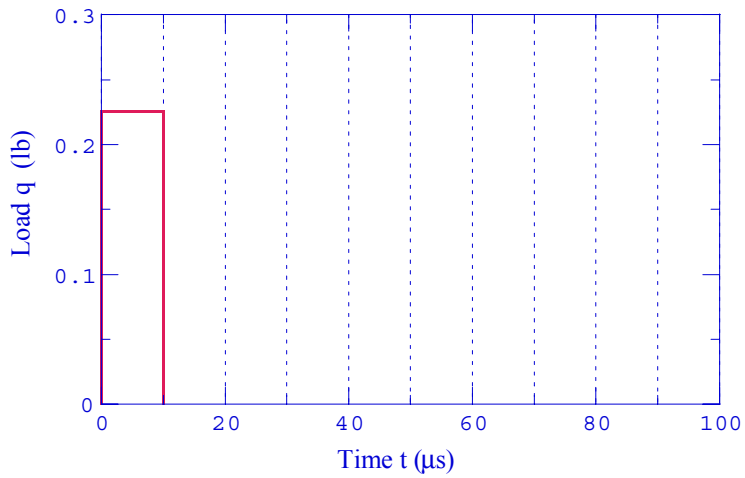

(a) Waveform

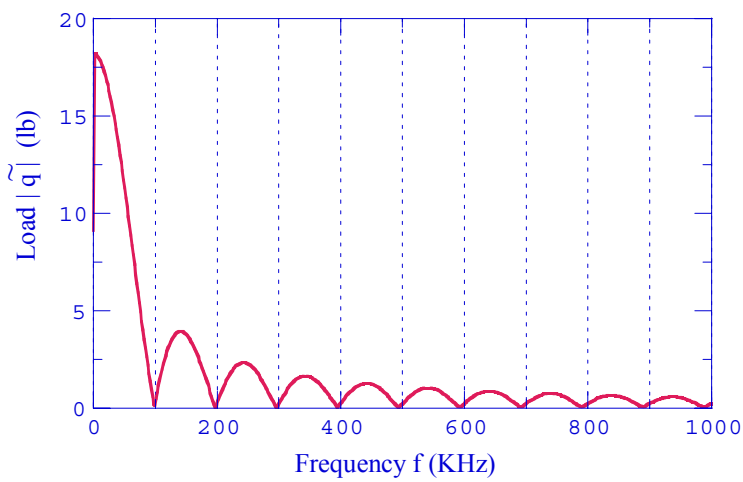

(b) Amplitude spectrum

Fig. 2.1 Impulse load history and its frequency spectrum

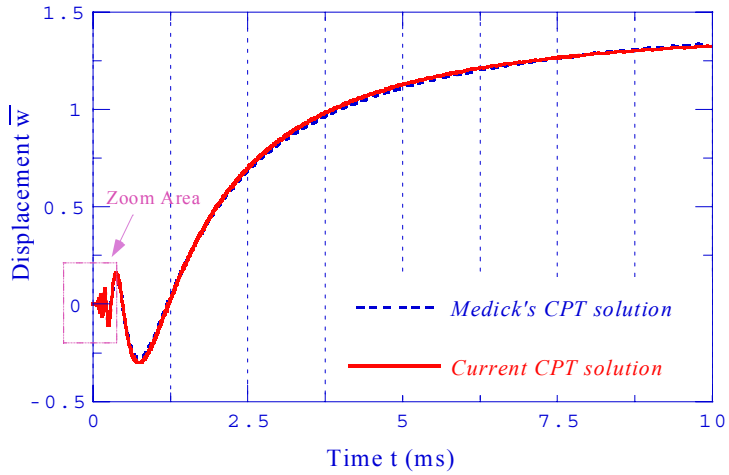

(a) Displacement at r = 6 in.

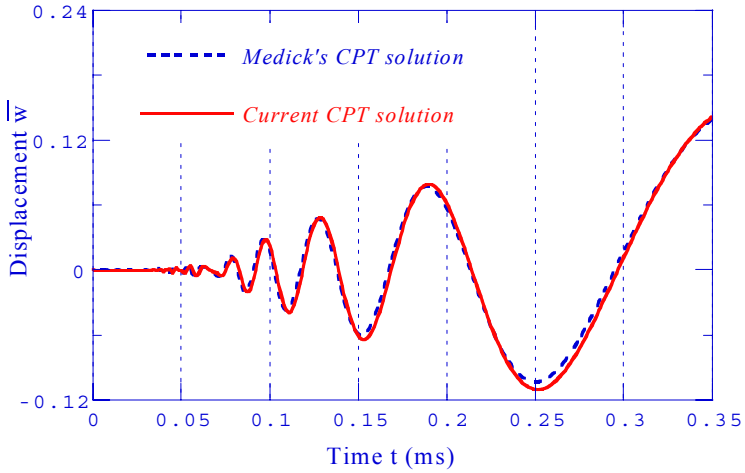

(b) Close view of (a)

Fig. 2.2 Comparison of transverse displacement between Medick's solution and current CPT solution

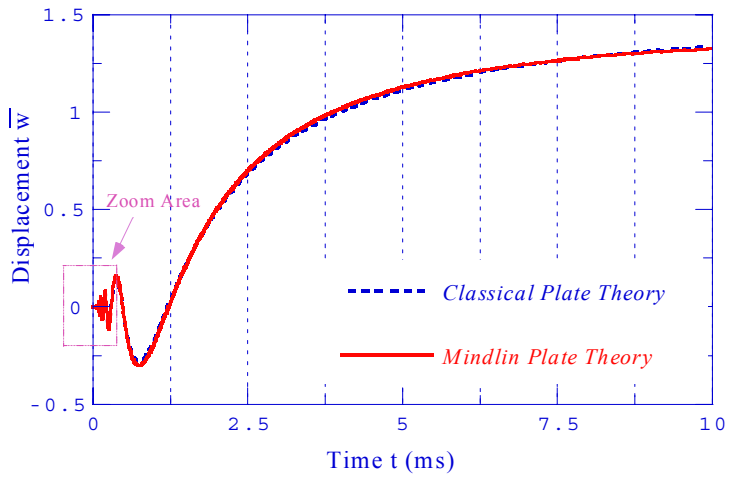

(a) Displacement at r = 6 in.

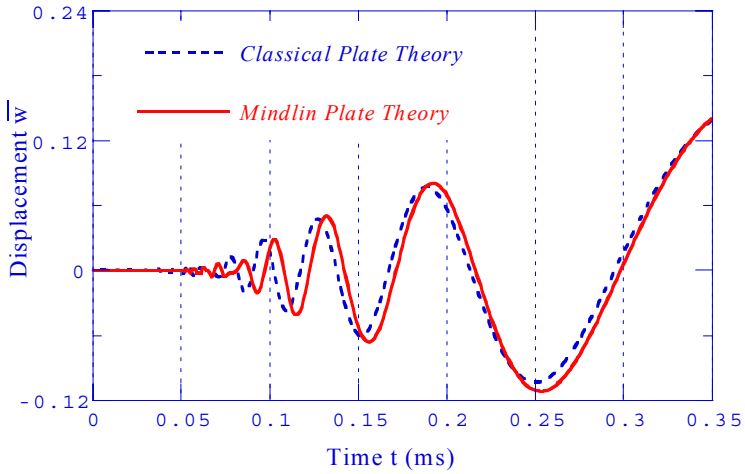

(b) Close view of (a)

Fig. 2.3 Comparison of transverse displacement between CPT and MPT

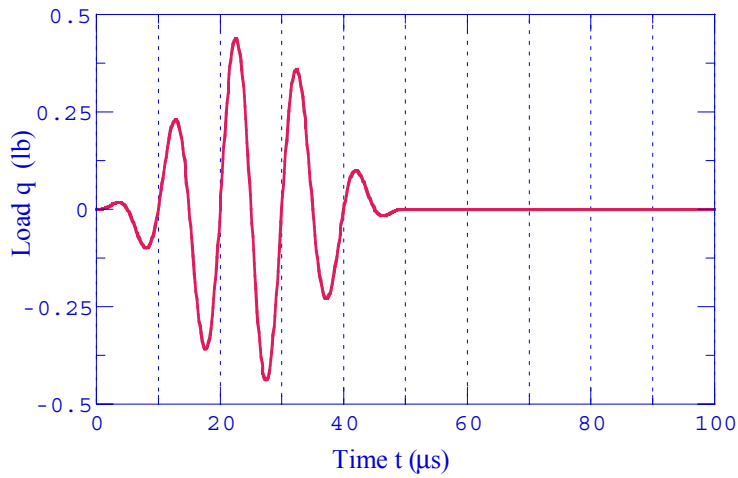

(a) Waveform

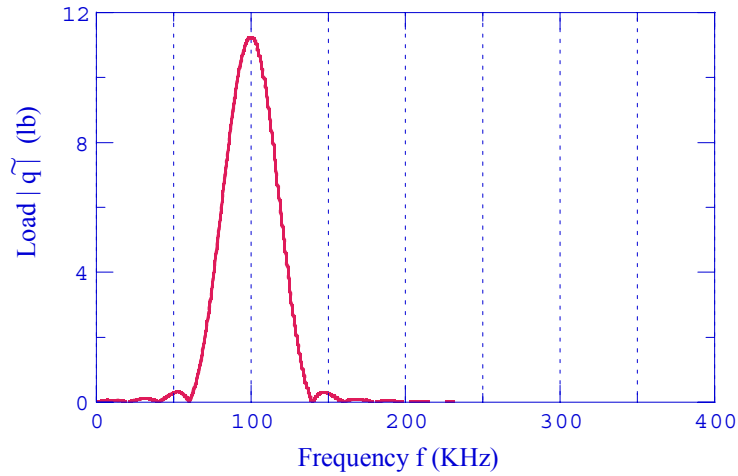

(b) Amplitude spectrum

Fig. 2.4 Sinusoid modulation loading history and its frequency spectrum

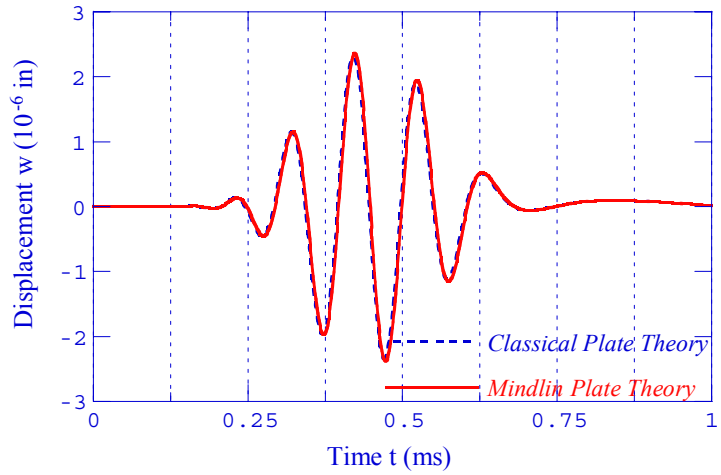

(a) f_0 = 10kHz

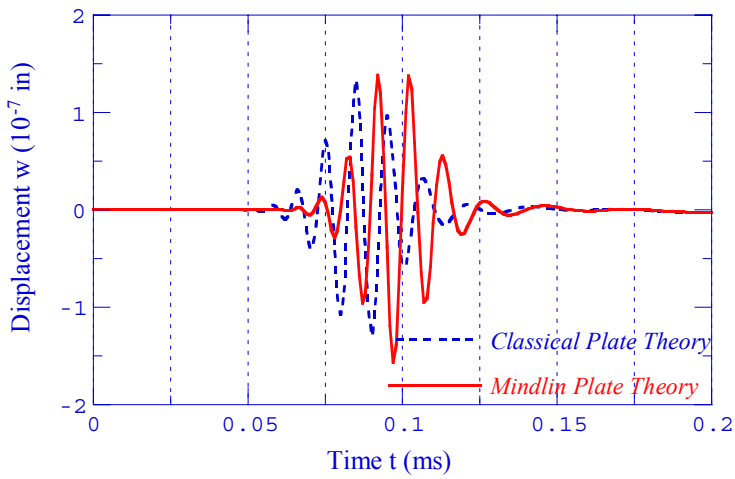

(b) f_0 = 100kHz

Fig. 2.5 Comparison of transverse displacements at r = 6 in. between CPT and MPT at different central frequencies when the load is a sinusoid modulation function

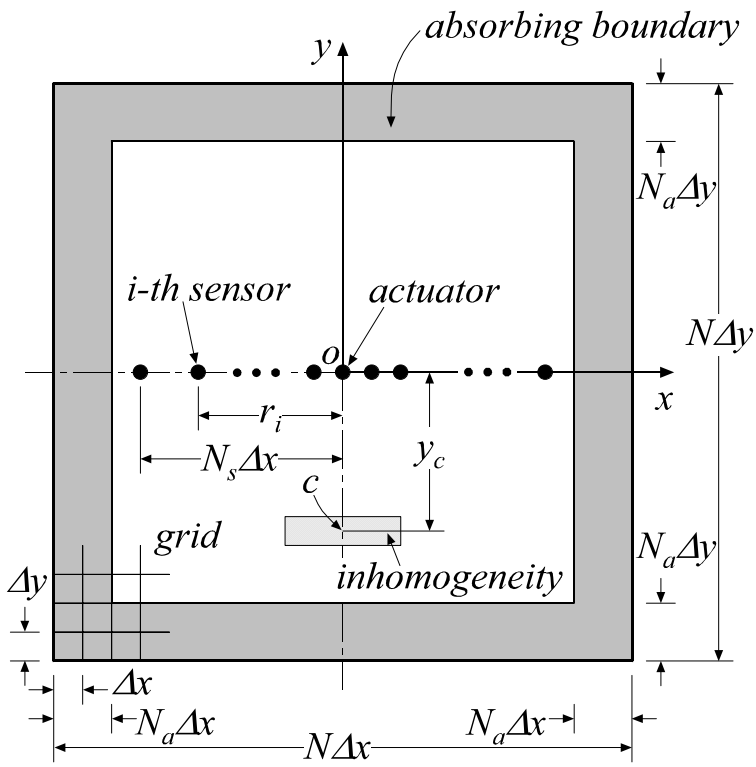

Fig. 2.6 Geometry of a square plate including absorbing boundaries, sensor/actuator and inhomogeneity locations, and finite difference grid spacing

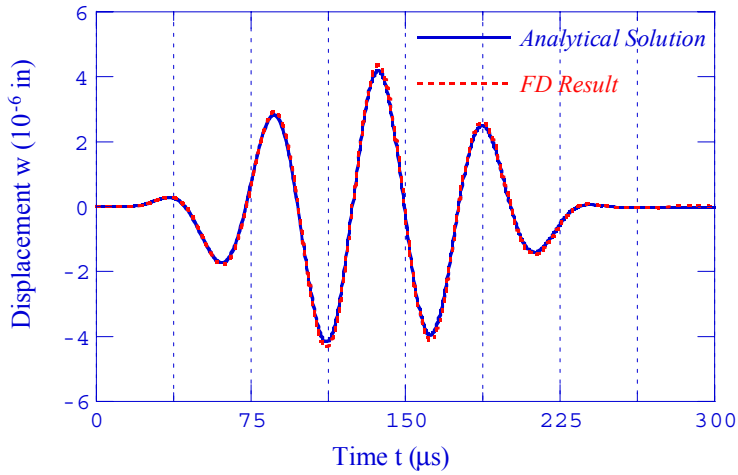

(a) r = 0.4 in., f_0 = 20kHz

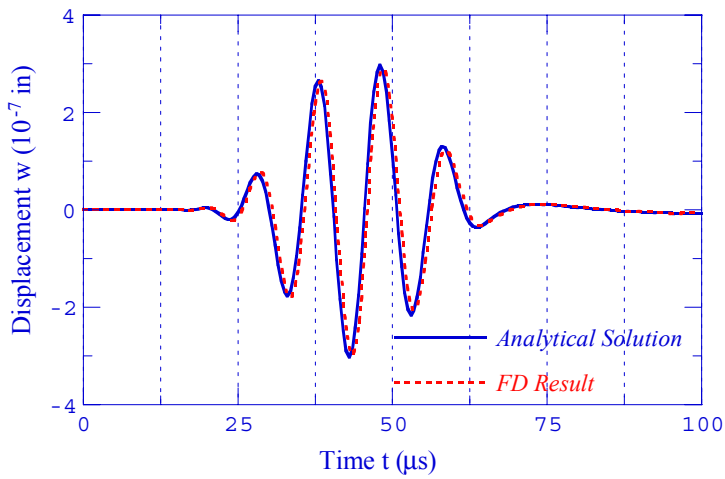

(b) r = 1.6 in., f_0 = 100kHz

Fig. 2.7 Comparison of transverse displacement between analytical solution and finite-difference result

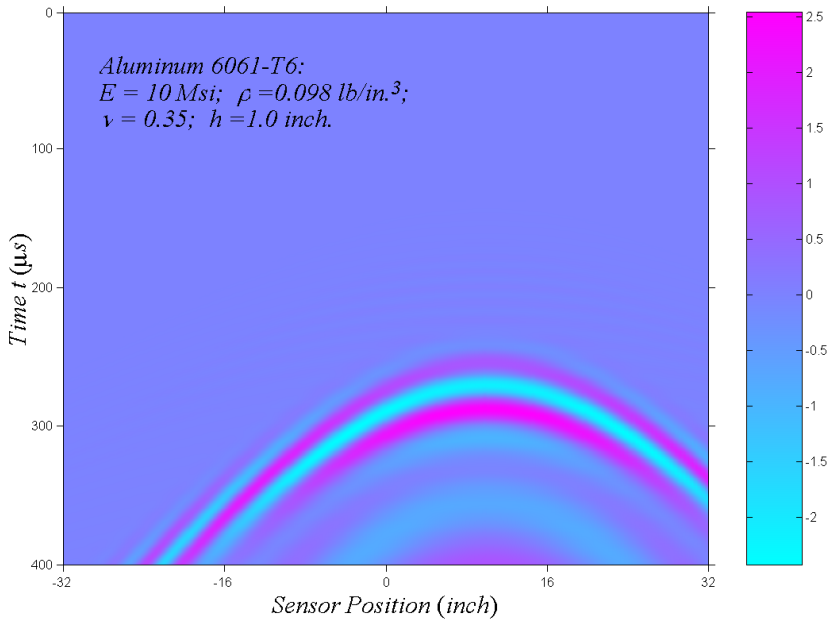

(a) inhomogeneity size: 40 in.×0.8 in.

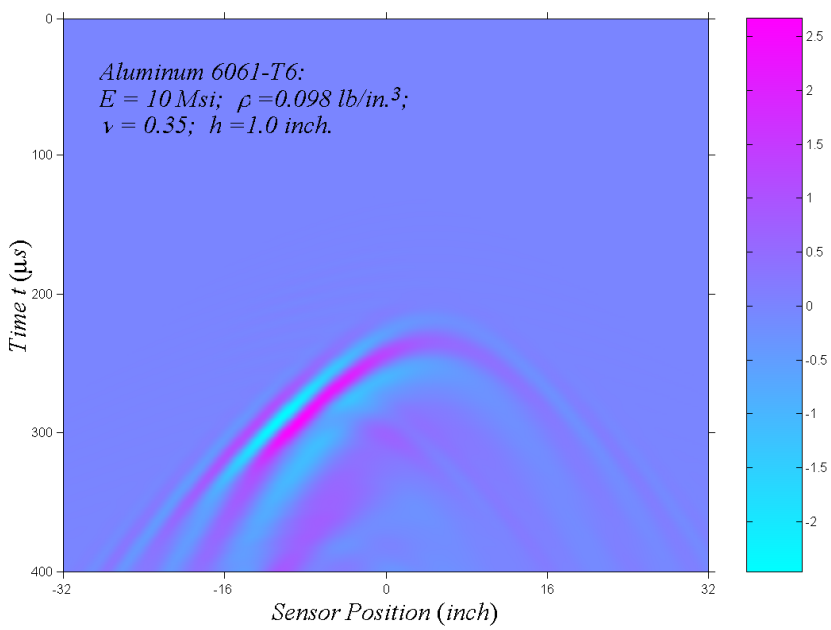

(b) inhomogeneity size: 10 in. ×5 in.

Fig. 2.8 Synthesized reflection wave field from different sizes of inhomogeneities

3 Poststack Migration: for Single Symmetric Damage

This chapter studied the feasibility of applying poststack migration to image the plate and detect a single, symmetric damage using synthetic data. In the first part of this chapter, the general concepts of poststack migration are introduced followed by a discussion about data pre-processing procedures before migration, such as muting direct arrival, deconvolution and Normal MoveOut (NMO) stacking. Then, a one-way version of flexural wave equation is derived and the correction of its dispersion relation is discussed briefly. Finally, some numerical results of the poststack migration are presented regarding different excitation signals and various damage shapes.

3.1 Concepts of migration

3.1.1 Poststack migration

The received reflection wave field contains information of the amplitude of reflectivity versus time history at different receivers (geophones or hydrophones in geophysics and piezoelectric sensors in SHM), as shown in Fig. 2.8. Each time an actuator is actuated and sends out a transient wavelet (a shot) and every sensor will collect a trace of reflection wave, which may also contain the direct arrival of the source wave. A time section is then obtained by presenting the traces from all the sensors for the same shot and it displays the echo amplitude on the coordinates of sensor location and time. The final target is to find the location, dimensions and the intensity of the reflection source (inhomogeneity or damage). The remaining problem is then how to attain the information about the reflectivity versus space (depth in geophysics and distance in SHM), or how to interpret those recorded data. Migration is a successful technique in geophysics to perform the interpretation. Because the reflection events appearing on the time sections are not as the same as the true position and shape of the reflector, migration moves these events back to the right position. Therefore migration can also be viewed as

a corrective technique that attempts to develop a right image of the reflectors from the distorted image in time section.

All migration techniques are based on Huygens' Principle: every point on a wavefront can be considered as a secondary source of spherical wavelets (Claerbout, 1983). As shown in Fig. 3.1a, the propagation waves generated from the source S reach the receiver R at moment t and are recorded. Reversibly, based on Huygens' principle, the wavefront at t-Δt can be re-constructed by using the received waves. Through this procedure, the waves are back-propagated towards the source. At certain moment, the wavefront of the back-propagating waves is coincident with the source and will have the same shape as the source. Thus, if a damage (reflector) is treated as a secondary source, back-propagating its reflection waves and imaging the wavefront at a pre-determined moment will reveal the existence and geometry of the damage. Fig. 3.1b illustrates the function of migration method. Assuming there is a point reflector in the x-y plane, the reflection waves recorded by a linear sensor array along the x-axis will appear as a hyperbolic events in the x-t (sensor position - time) coordinates. Migration collapses the hyperbolic events in the x-t plane to the point in the x-y plane, thus extracts the information in spatial domain from the raw data in time domain. Migration in geophysics includes two basic steps: extrapolation and imaging (Dai, 1993). Extrapolation means treating the recorded wave field as an excitation and reconstructing the spatial wave field on the vertical section of the Earth. Most of the latest migration techniques are proceeded based on the wave equation. In these processes, the recorded wave field is used as a boundary condition to solve the wave equation, then the reflection wave field is back-propagated or extrapolated. Imaging means building and displaying the strength and location of the reflector by extracting a variable from the extrapolated wave field, which is governed by an imaging principle. The imaging principle or imaging time condition is the moment when the back propagation is stopped. One variable from the reconstructed wave field is then extracted and presented in the spatial coordinates. In this way, the reflector, or the damage in SHM, is imaged and the data collected in the time domain is converted into the information in the spatial domain. Because the migration actually

focuses the reflection energy, not only it gives the right location and shape of the image, the resolution of the image in the migrated space section will also be better than in the time section.

In this section, the migration is applied to image the damage in the plate after the time sections are stacked, so-called poststack sections. Poststack migration is based on zero-offset experiment, which means that the actuator and sensor are at the same position. In this analysis, the reflector is looked as an exploding source (so called exploding reflector model). Under the assumption of this model, the reflector is treated as a source and is exploded at time $T/2$, and the data recorded in this way will be the same as the data recorded in the zero-offset configuration. Here T is the two-way travel time of a wavelet to and from the reflector. Or equivalently, to explode the reflector as a source at $t = 0$ and halve the velocity of the wave propagation to get the same result. The wave signals collected by a linear array of sensors are usually finite-offset data. Therefore, before the migration, the received signals need to be sorted into approximate zero-offset data.

Before the recorded wave field can be migrated to image the damage in the plate, several data processing procedures must be taken. There is a long list of data processing techniques related to the migration in geophysics (Yilmaz, 1993). For SHM for a plate-like structure, only muting, deconvolution and stacking are needed. Some other data processing procedures, such as velocity analysis and residual statics correction that are related tightly to geophysical prospecting, are not necessary for use in SHM.

3.1.2 Finite difference reverse-time migration

Wave equation migration can be performed in either the space-time domain, in the space-frequency domain, in the wavenumber-frequency domain or in the wavenumber-time domain. The numerical techniques employed in migration processes can generally be divided into three categories, namely, the finite difference approach, the summation approach and the transformation approach (Dai, 1993; Yilmaz, 1993). In this study, finite difference reverse-time migration is adopted. In the reverse-time migration, the recorded wave traces at each sensor are reversed in time first, then are assigned to the corresponding locations at each time step. Now the extrapolation is then proceeded by

solving the one-way wave equation with the boundary conditions at sensor locations. The finite difference algorithm discussed in Chapter 2 is used to solve the equation and to back-propagate the wave field. The material constants must be modified so that the wave propagation velocity will be set to be half of the value to satisfy the basic assumption of exploding reflector model. The reason of using reverse-time migration is that the main target of SHM is the initiation and propagation of the damage and the dimension of the incipient damage of interest is rather small compared to the size of the structure. Thus it is reasonable to assume that the wave propagation velocity is almost constant all over the entire plate, which guarantees that reverse-time migration will give the same accuracy as other migration methods.

The imaging time condition is proposed based on the assumption that reflector exists in the Earth where an upgoing wave is time-coincident with the first arrival of a downgoing wave (Claerbout, 1985). Or, a reflector exists at the spatial and temporal coincidence of incidence and reflection waves. For poststack migration, exploding reflector model assumes that all the energy of the waves recorded at time t on the stacked data arises from the reflection at time $t/2$. Thus the reflector can be determined by propagating that energy back for half of its arrival time. The imaging condition for zero offset gathers then could be expressed simply as: the extrapolated wave field at time zero when half velocity is used or $t/2$ when full velocity is used. In this study, the former is chosen: the whole plate is simultaneously imaged at time 0. The plate is imaged by extracting the velocity of transverse deformation at all the finite difference grid points.

3.2 Data processing before migration

3.2.1 Muting

Muting means the process to reject the direct incidence waves from the total wave field received by sensors and to obtain a pure reflection wave signals. For muting the direct arrival from the actuator, the arrival time and duration of the reflection wavelet for each sensor are estimated, then the wave amplitude before the estimated arrival time was

set to zero. The ith sensor trace (velocity of transverse deformation) is processed by

$$\dot{w}_i^a(t) = \dot{w}_i^b(t) \cdot H[t - \frac{(i-1)\Delta x}{k_s V_S} + k_W T_W] \tag{3.1}$$

where H is the Heaviside step function, V_S is the shear wave velocity, and T_w is the duration of the source wavelet. k_s and k_w are two correction factors, which are estimated to compensate the shift induced by the dispersion property of the waves. The superscripts a and b denote after and before stacking respectively. The trace after treated in this way will have an abrupt change (from zero to a certain value) at the end point of the muting region. This may further cause other difficulties in the following data processing procedures. One way to overcome this problem is to add small amplitude of white noise into the trace after muting. It is equivalent to shift its spectrum slightly, and will not affect the real signature of the trace. In fact, this will provide more realistic measures in actual situations. It should also be noticed that when the direct arrival is muted by this method, some of the reflected and diffracted energy may also be removed if they overlap to some extent with the direct arrival. This unwanted removal may affect the accuracy of the final migration result. It happens because some reflectors may be so close to the actuator that its reflection travel time is shorter than the span of the excitation wavelet.

Another method for muting is to subtract the wave field of the plate without inhomogeneity from the recorded wave field. This method is a good choice in synthesizing the scattering wave field for the migration. In real SHM applications, this is only applicable to history monitoring, in which the original state is accessible. Even in this situation, one must pay close attention to the possible phase shift occurred in the following tests after the first recording.

3.2.2 Deconvolution

Instinctively, one may want to use spike-like signal to drive the piezoelectric actuator. Then the sensor would also receive a spike signal, thus a better resolution of the damage identification can be obtained. It is however unlikely and by no means a good idea to have a broad band input signal. The dispersion effect of the flexural waves would

distort the received signals, making them almost impossible to synchronize with the initialization signals. A complementary approach relies on narrow banded excitation signals, whose length of the wavelet can be neither zero nor infinite. However due to the finite length of the wavelet, the time required for back-propagation cannot be determined. If the first arrival signal is adopted, signals following the first arrival are not migrated to the reflectors yet. This is called under migration, in contrast with over migration in which the termination of the signal is used as the arrival time. Thus the received signal must be processed and turn the banded signals back into spike signal again, which is called deconvolution. In view of real SHM applications, only banded wavelets could be generated to actuate the actuators for Lamb wave excitation. Comparing the assumptions about deconvolution in seismology and their compatibility in SHM, it is found that it is not appropriate to adopt directly the deconvolution techniques used in geophysics into SHM. First, it is assumed in geophysics that the source generates only *P*-waves, and that these waves will only impinge on layer boundaries at normal incidence, therefor no shear waves will be generated. However, flexural waves in a plate may be divided into three types: slow flexural, fast flexural and thickness-shear waves (Pao and Chao, 1964). In general, any one of these waves propagating towards the edge of a plate or the interface of inhomogeneity gives rise to reflected waves of all three types. Secondly, it is assumed in geophysics that the source waveform does not change as it travels in the Earth. For plate SHM, this assumption can not be satisfied because the flexural waves are dispersive. Thus, the difficulty of deconvolution of flexural waves in a plate lies in that it is dispersive, i.e., it has different wave shapes at different times and different spatial points, which makes re-constructing the spike signal unlikely. Finding an effective deconvolution method for achieving high resolution is a valuable topic for using migration in SHM.

3.2.2.1 Time domain (Wiener optimal filter) deconvolution

Wiener filtering involves designing the filter $f(t)$ so that the least-squares error between the actual $y(t)$ output induced by $x(t)$ and desired outputs $d(t)$ is a minimum (Yilmaz, 1993). From this assumption, it is quite straightforward to derive that

$$\sum_{\tau} f_{\tau} \sum_{t} x_{t-\tau} x_{t-i} = \sum_{t} d_t x_{t-i} \qquad (i = 0, 1, 2 \ldots n-1) \tag{3.2}$$

Define auto-correlation of the input as

$$r_{i-\tau} = \sum_{t} x_{t-\tau} \cdot x_{t-i} \tag{3.3}$$

and cross-correlation between the desired output and the input as

$$g_i = \sum_{t} d_t \cdot x_{t-i} \tag{3.4}$$

an equation to solve the filter parameter f_i is obtained

$$\begin{bmatrix} r_0 & r_1 & r_2 & \cdots & r_{n-1} \\ r_1 & r_2 & r_3 & \cdots & r_{n-2} \\ . & . & . & & . \\ . & . & . & & . \\ r_{n-1} & r_{n-2} & r_{n-2} & \cdots & r_0 \end{bmatrix} \begin{Bmatrix} f_0 \\ f_1 \\ . \\ . \\ f_{n-1} \end{Bmatrix} = \begin{Bmatrix} g_0 \\ g_1 \\ . \\ . \\ g_{n-1} \end{Bmatrix} \tag{3.5}$$

For spike deconvolution, it can be simply set $g_0 = x_0,\ g_1 = g_2 = \ldots = g_{n-1} = 0$.

3.2.2.2 Frequency domain deconvolution

Successful deconvolution requires minimum phase wavelet. Although it is possible to construct this kind of wavelet in numerical calculation, it is very difficult to realize perfect minimum phase wavelet in the experimental work or in real applications. Band limited signals are not causal since it does not contain information associated with every frequency component. Thus the signals will make the effect of deconvolution not as good as expected. Assuming that the autocorrelation of the input wavelet $q(t)$ in the frequency domain could be written as:

$$R_w(\omega) = Q(\omega) \cdot \overline{Q}(\omega) \tag{3.6}$$

where $\overline{Q}(\omega)$ is the complex conjugate of the Fourier transform of $q(t)$. Define

$$U(\omega) = \ln[R_w(\omega)] \tag{3.7}$$

then if an auxiliary ϕ is suitably chosen, eq. (3.6) can be rewritten as

$$R_w(\omega) = e^{[U(\omega)+i\phi(\omega)]/2} \cdot e^{[U(\omega)-i\phi(\omega)]/2} \tag{3.8}$$

with $\phi(\omega)$ being suitably chosen.

Comparing eqs. (3.8) with eq. (3.6) gives

$$Q(\omega) = e^{[U(\omega)+i\phi(\omega)]/2} \tag{3.9}$$

If a minimum-phase wavelet is assumed, $\phi(\omega)$ turns out to be the Hilbert transform of $U(\omega)$. The deconvolution operator (or inverse filter) in the frequency domain is then written as

$$A_f(\omega) = 1/A(\omega), \quad \varphi_f(\omega) = -\varphi(\omega) \tag{3.10}$$

where $A(\omega)$ and $\varphi(\omega)$ is the amplitude spectra and phase spectra of the minimum phase wavelet $Q(\omega)$, respectively. To avoid dividing-zero error in the above calculation and to ensure the stability of the filter, a small constant number is required to be added into the amplitude spectrum, which is called prewhitening.

3.2.3 Normal moveout (NMO) correction and stacking

Poststack migration is based on exploding reflector model. Thus the CMP section must be stacked to construct zero offset data before migration. In geophysics, zero offset data means the reflection response for a point source at the surface being recorded only at the position of the source. In SHM, it means that the actuator and sensor must be at the same position. Because the duration of the excitation wavelet is known, by special circuit design of the data acquisition system, piezoelectric materials can serve as both actuator and sensor alternately. Zero-offset data then can be gathered by a sequence of single receiver experiments, in which for each shot only the actuator will be used as sensor to receive the reflection. But it still provides promising advantages to use finite offset data because it generates plenty of data sets to increase signal-to-noise ratio (SNR). Using CMP gather makes it possible to obtain the maximum span for the sensors, which is beneficial for decreasing the truncation error induced by finite domain measurement. Unlike in single receiver experiment, each shot will have the entire receivers to record

data. Because the reflection signal is identical and the random noise is mutually uncorrelated from trace to trace, this redundant recording will improve SNR. If the damage exists, the induced hyperbolic event will be strengthened while the random noise as well as the non-hyperbolic events will be attenuated by the stacking. Fig. 3.2 and 3.3 illustrate the process of stacking. As shown in Fig. 3.2, trace 4 from shot 1 and trace 6 from shot 2 have a common midpoint. They will be summed together to form trace 4 in the stacked section. It is clear that the travel time of trace 6 in shot 2 has a different Δt_{NMO} from the travel time of trace 4 in shot 1 shown in Fig. 3.3, which is a zero offset trace. Given a stacking velocity V_{NMO}, it can be easily obtained that

$$\Delta t_{NMO} = [t_0^2 + (2x/V_{NMO})^2]^{1/2} - t_0 \tag{3.11}$$

where t_0 is the two-way travel time of zero offset trace, x is the half offset (distance between the midpoint and the source or the sensor), V_{NMO} is chosen as the velocity of shear waves in this study. Thus before trace 6 can be summed into the final zero-offset section, it must be corrected by a term Δt_{NMO}. This step is called Normal MoveOut (NMO) correction. Summing together the NMO corrected traces is referred to as stacking and the resulting data is called stacked section. It could be noted that Δt_{NMO} may not be equal to the time step in synthesizing the reflection waves or the sampling interval in real applications. Thus interpolation algorithm is used to calculate the values for the points that are not coincident with the sampling points. NMO correction and stacking compose an approximate zero-offset trace collection on which the zero-offset (poststack) migration is applied.

Fig. 3.4 and 3.5 give an example of NMO and stacking. Fig. 4 is the synthesized reflection wave field. The damage is selected as a narrow strip: 40×0.8 with center at (0, -16). 51 shots were made, ranged from –10 in. to 10 in. along the x-axis. Fig. 3.4a is the gather from a shot at the center of the plate, while Fig. 3.4b shows the gather from a shot 10 inches away from the center, which is farthest from the center among all the shots. To guarantee that each zero offset trace in stacked section is summed from a same number of traces, the effective stack range is chosen to be from -16 in. to 16 in.. It can be observed

that the hyperbolic events in Fig. 3.4 are successfully flatten by NMO and stacking, as shown in Fig. 3.5.

3.3 One-way wave equation

3.3.1 Derivation

Assuming the damage is located below the x-axis, the reflection goes upward and the migration can be treated as a downward continuation similar in geophysics. Isolating the wave equation along the y-direction, eq. (2.29) yields

$$\frac{\partial \mathbf{U}}{\partial t} = \mathbf{B}_t \frac{\partial \mathbf{U}}{\partial y} \tag{3.12}$$

If λ_i be the eigenvalues of $\mathbf{B}_t$ ($\lambda_1 \le \lambda_2 \cdots \le \lambda_8$), the matrix $\mathbf{B}_t$ can be diagonalized into a diagonal matrix $\mathbf{\Lambda}$ with $\mathbf{\Lambda}_{ii}=\lambda_i$ by a transformation:

$$\mathbf{L}\mathbf{B}_t\mathbf{R} = \mathbf{\Lambda} \tag{3.13}$$

where the rows of the matrix $\mathbf{L}$ are the normalized left row eigenvectors corresponding to eigenvalue λ_i of $\mathbf{B}_t$, and the columns of the matrix $\mathbf{R}$ are the corresponding normalized right column eigenvectors. For migration purpose, the plate is considered to be homogenous. Thus $\mathbf{B}_t$ is independent of y. Further by knowing the orthogonality relation $\mathbf{L}\,\mathbf{R} = \mathbf{I}$ and applying the linear transformation $\mathbf{V} = \mathbf{L}\,\mathbf{U}$, eq. (3.13) can be written as

$$\frac{\partial \mathbf{V}}{\partial t} = \mathbf{\Lambda} \frac{\partial \mathbf{V}}{\partial y} \tag{3.14}$$

Or it can be written as $\frac{\partial \mathbf{V}_i}{\partial t} = \lambda_i \frac{\partial \mathbf{V}_i}{\partial y}$, which describes the wave $\mathbf{V}_i$ travelling with a characteristic velocity $-\lambda_i$. For $\lambda_i > 0$, the wave $\mathbf{V}_i$ travels in the negative y-direction. Based on eq. (3.13), rewriting eq. (3.12) leads to

$$\frac{\partial \mathbf{U}}{\partial t} = \mathbf{R}\,\mathbf{\Lambda}\,\mathbf{L} \frac{\partial \mathbf{U}}{\partial y} \tag{3.15}$$

Solving the eight eigenvalues of matrix $\mathbf{B}_t$ and arranging them in order yields

$$\left(-\sqrt{\frac{2}{1-\nu}}C_S, -C_S, -\kappa C_S, 0, 0, \kappa C_S, C_S, \sqrt{\frac{2}{1-\nu}}C_S\right) \tag{3.16}$$

where C_S is the velocity of the shear waves. The right and left eigenvectors are

$$\mathbf{R} = \begin{bmatrix} 0 & 0 & i\left(\frac{\kappa h\sqrt{\rho G}}{2}\right)^{1/2} & 0 & 0 & \left(\frac{\kappa h\sqrt{\rho G}}{2}\right)^{1/2} & 0 & 0 \\ 0 & i\left(\frac{h^3\sqrt{\rho G}}{24}\right)^{1/2} & 0 & 0 & 0 & 0 & \left(\frac{h^3\sqrt{\rho G}}{24}\right)^{1/2} & 0 \\ i\left(\frac{h^3}{24}\sqrt{\frac{2\rho G}{1-\nu}}\right)^{1/2} & 0 & 0 & 0 & 0 & 0 & 0 & \left(\frac{h^3}{24}\sqrt{\frac{2\rho G}{1-\upsilon}}\right)^{1/2} \\ 0 & 0 & -i\left(\frac{1}{2\kappa h\sqrt{\rho G}}\right)^{1/2} & 0 & 0 & \left(\frac{1}{2\kappa h\sqrt{\rho G}}\right)^{1/2} & 0 & 0 \\ 0 & 0 & 0 & 0 & 1 & 0 & 0 & 0 \\ 0 & 0 & 0 & 1 & 0 & 0 & 0 & 0 \\ -i\left(\frac{6}{h^3}\sqrt{\frac{1-\upsilon}{2\rho G}}\right)^{1/2} & 0 & 0 & -\nu & 0 & 0 & 0 & \left(\frac{6}{h^3}\sqrt{\frac{1-\upsilon}{2\rho G}}\right)^{1/2} \\ 0 & -i\left(\frac{6}{h^3\sqrt{\rho G}}\right)^{1/2} & 0 & 0 & 0 & 0 & \left(\frac{6}{h^3\sqrt{\rho G}}\right)^{1/2} & 0 \end{bmatrix}$$

and

$$\mathbf{L} = \begin{bmatrix} 0 & 0 & -i\left(\frac{6}{h^3}\sqrt{\frac{1-\nu}{2\rho G}}\right)^{1/2} & 0 & 0 & i\mu\left(\frac{h^3}{24}\sqrt{\frac{2\rho G}{1-\nu}}\right)^{1/2} & i\left(\frac{h^3}{24}\sqrt{\frac{2\rho G}{1-\nu}}\right)^{1/2} & 0 \\ 0 & -i\left(\frac{6}{h^3\sqrt{\rho G}}\right)^{1/2} & 0 & 0 & 0 & 0 & 0 & i\left(\frac{h^3\sqrt{\rho G}}{24}\right)^{1/2} \\ -i\left(\frac{1}{2\kappa h\sqrt{\rho G}}\right)^{1/2} & 0 & 0 & i\left(\frac{\kappa h\sqrt{\rho G}}{2}\right)^{1/2} & 0 & 0 & 0 & 0 \\ 0 & 0 & 0 & 0 & 0 & 1 & 0 & 0 \\ 0 & 0 & 0 & 0 & 1 & 0 & 0 & 0 \\ \left(\frac{1}{2\kappa h\sqrt{\rho G}}\right)^{1/2} & 0 & 0 & \left(\frac{\kappa h\sqrt{\rho G}}{2}\right)^{1/2} & 0 & 0 & 0 & 0 \\ 0 & \left(\frac{6}{h^3\sqrt{\rho G}}\right)^{1/2} & 0 & 0 & 0 & 0 & 0 & \left(\frac{h^3\sqrt{\rho G}}{24}\right)^{1/2} \\ 0 & 0 & \left(\frac{6}{h^3}\sqrt{\frac{1-\nu}{2\rho G}}\right)^{1/2} & 0 & 0 & \mu\left(\frac{h^3}{24}\sqrt{\frac{2\rho G}{1-\nu}}\right)^{1/2} & \left(\frac{h^3}{24}\sqrt{\frac{2\rho G}{1-\nu}}\right)^{1/2} & 0 \end{bmatrix}$$

Setting the negative eigenvalues equal to zero, the one-way wave equation for the flexural waves propagating in the negative-y direction is obtained

$$\frac{\partial \mathbf{U}}{\partial t} = \mathbf{A}_t \frac{\partial \mathbf{U}}{\partial x} + \hat{\mathbf{B}}_t \frac{\partial \mathbf{U}}{\partial y} + \mathbf{C}_t \mathbf{U} + \mathbf{p} \tag{3.17}$$

where

$$\hat{\mathbf{B}}_t = \frac{1}{2}\begin{bmatrix} \kappa\sqrt{\frac{G}{\rho}} & 0 & 0 & \kappa^2 Gh & 0 & 0 & 0 & 0 \\ 0 & \sqrt{\frac{G}{\rho}} & 0 & 0 & 0 & 0 & 0 & \frac{Gh^3}{12} \\ 0 & 0 & \sqrt{\frac{2G}{(1-\nu)\rho}} & 0 & 0 & \frac{Gh^3}{6}\frac{\nu}{1-\nu} & \frac{Gh^3}{6(1-\nu)} & 0 \\ \frac{1}{\rho h} & 0 & 0 & \kappa\sqrt{\frac{G}{\rho}} & 0 & 0 & 0 & 0 \\ 0 & 0 & 0 & 0 & 0 & 0 & 0 & 0 \\ 0 & 0 & 0 & 0 & 0 & 0 & 0 & 0 \\ 0 & 0 & \frac{12}{\rho h^3} & 0 & 0 & \sqrt{\frac{2G}{(1-\nu)\rho}}\nu & \sqrt{\frac{2G}{(1-\nu)\rho}} & 0 \\ 0 & \frac{12}{\rho h^3} & 0 & 0 & 0 & 0 & 0 & \sqrt{\frac{G}{\rho}} \end{bmatrix}$$

Fig. 3.6 and Fig. 3.7 show the difference of the wave propagation governed by the full-way equation and the one-way equation. Four sequential snapshots of the wave field generated by a point force (governed by eq. (2.24) with $\beta = 50\mu s$) at the center of the plate are taken and presented. In Fig. 3.6, which is synthesized by use of the full-way eq. (2.39), the wavefront remains as a circle with center at the loading point during the propagation. The flexural waves propagate radially in a plane wave form. In the fourth frame, reflection from the boundary can be observed. Fig. 3.7 gives the one-way wave field governed by eq. (3.17). It can be observed that the wave propagates only in the desirable negative *y*-direction. Since the dispersion relation of the one-way equation is not the same as that in the full-way equation, the wave front does not propagate in a form of circle. The wavefront becomes a distorted ellipse, and only in a very small range of incidence angle the wavefront remains circular shape. Furthermore, there exist many unwanted multiples of the waves. Therefore, for a satisfactory migration, the dispersion relation of the one-way wave equation must be corrected to a better approximation of the full-way equation.

3.3.2 Correction of the dispersion relation

The one-way wave equation eq. (3.17), which governed the waves propagating in negative-*y* direction, is modified by multiplying the matrix $\mathbf{A}_0$ by a factor α and becomes

$$\mathbf{E}_0 \frac{\partial \mathbf{u}}{\partial t} = \alpha \mathbf{A}_0 \frac{\partial \mathbf{u}}{\partial x} + \hat{\mathbf{B}}_0 \frac{\partial \mathbf{u}}{\partial y} + \mathbf{C}_0 \mathbf{u} + \mathbf{p} \tag{3.18}$$

where

$$\hat{\mathbf{B}}_0 = \frac{1}{2}\begin{bmatrix} \kappa h\sqrt{\rho G} & 0 & 0 & 1 & 0 & 0 & 0 & 0 \\ 0 & \frac{h^3}{12}\sqrt{\rho G} & 0 & 0 & 0 & 0 & 0 & 1 \\ 0 & 0 & \frac{h^3}{12}\sqrt{\rho G}\sqrt{\frac{2}{1-\nu}} & 0 & 0 & 0 & 1 & 0 \\ 1 & 0 & 0 & \frac{1}{\kappa h\sqrt{\rho G}} & 0 & 0 & 0 & 0 \\ 0 & 0 & 0 & 0 & 0 & 0 & 0 & 0 \\ 0 & 0 & 0 & 0 & 0 & 0 & 0 & 0 \\ 0 & 0 & 1 & 0 & 0 & 0 & \frac{12}{h^3\sqrt{\rho G}}\sqrt{\frac{1-\nu}{2}} & 0 \\ 0 & 1 & 0 & 0 & 0 & 0 & 0 & \frac{12}{h^3\sqrt{\rho G}} \end{bmatrix}$$

Rewrite eq. (3.18) in the form of eq. (2.2):

$$\rho h\frac{\partial^2 w}{\partial t^2} = \alpha\frac{\partial Q_x}{\partial x} + \frac{1}{2}\kappa h\sqrt{\rho G}\frac{\partial w}{\partial y\partial t} + \frac{1}{2}\frac{\partial Q_y}{\partial y} + q \tag{3.19a}$$

$$\frac{\rho h^3}{12}\frac{\partial^2 \psi_x}{\partial t^2} = \alpha\frac{\partial M_x}{\partial x} + \frac{h^3}{24}\sqrt{\rho G}\frac{\partial \psi_x}{\partial y\partial t} + \frac{1}{2}\frac{\partial M_{xy}}{\partial y} - Q_x \tag{3.19b}$$

$$\frac{\rho h^3}{12}\frac{\partial^2 \psi_y}{\partial t^2} = \alpha\frac{\partial M_{xy}}{\partial x} + \frac{h^3}{24}\sqrt{\rho G}\sqrt{\frac{2}{1-\nu}}\frac{\partial \psi_y}{\partial y\partial t} + \frac{1}{2}\frac{\partial M_y}{\partial y} - Q_y \tag{3.19c}$$

$$\frac{\partial Q_y}{\partial t} = \kappa^2 Gh\left(\frac{1}{2}\frac{\partial w}{\partial y\partial t} + \frac{1}{2\kappa h\sqrt{\rho G}}\frac{\partial Q_x}{\partial y} + \frac{\partial \psi_y}{\partial t}\right) \tag{3.19d}$$

$$\frac{\partial Q_x}{\partial t} = \kappa^2 Gh\left(\alpha\frac{\partial w}{\partial x\partial t} + \frac{\psi_x}{\partial t}\right) \tag{3.19e}$$

$$\frac{\partial M_x}{\partial t} - \nu\frac{\partial M_y}{\partial t} = \alpha\left(1-\nu^2\right)D\frac{\partial \psi_x}{\partial x\partial t} \tag{3.19f}$$

$$\frac{\partial M_y}{\partial t} - \nu\frac{\partial M_x}{\partial t} = \left(1-\nu^2\right)D\left(\frac{1}{2}\frac{\partial \psi_y}{\partial y\partial t} + \frac{6}{h^3\sqrt{\rho G}}\sqrt{\frac{1-\nu}{2}}\frac{\partial M_y}{\partial y}\right) \tag{3.19g}$$

$$\frac{\partial M_{xy}}{\partial t} = \frac{(1-\nu)D}{2}\left[\alpha\frac{\partial \psi_y}{\partial x\partial t} + \frac{1}{2}\frac{\partial \psi_x}{\partial y\partial t} + \frac{6}{h^3\sqrt{\rho G}}\frac{\partial M_{xy}}{\partial y}\right] \tag{3.19h}$$

It is then possible to determine α value by applying a least-square optimization to minimize the difference of dispersion relations between eq. (2.2) and eq. (3.19). After correction, in a wider range of incidence angles (relative to the negative *y*-axis) the one-way flexural waves governed by eq. (3.18) should be able to keep the properties of the full way wave.

3.4 Numerical results

In this section, a number of images generated by the poststack migration algorithm are presented. In these images, the reflectivity at each grid of the plate is displayed at different gray levels. The area marked by thin lines indicates the true dimension and location of the assumed damage. To sharpen the image of the damage, some pictures are generated from $\dot{w}^p$ (p is a positive integer and will be indicated in the figure's caption). In these images, artifacts due to the data truncation can be observed. Other factors account for these artifacts are: (a) the dispersion relation of derived one-way wave equation has not been corrected; (b) deconvolution was not processed for the reflection traces; (c) the shape of the damage violates the assumption of NMO process. Especially when the dimension of the damage is rather large, the detection image is not consistent with the actual damage, which can only be solved by prestack migration.

Fig. 3.8 compares the effect of three different excitation signals, half cycle and full cycle of sine function and a sinusoid modulation function, on the image of the damage (p = 4). The assumed damage is a 0.8×0.8 square with center at (0, -16). It can be seen that the sinusoid modulation excitation signal gives the best image among the three excitation signals. Fig. 3.9 shows the image of post-stack migration for different shapes of damages. Both cases use sinusoid modulation excitation wavelet (frenquency f_0= 40kHz and p = 2). The images of a 0.8×0.8 square damage at (0, -16) and a line damage with dimension 3.2×0.2 at center (0, -10) appear correctly in the figures.

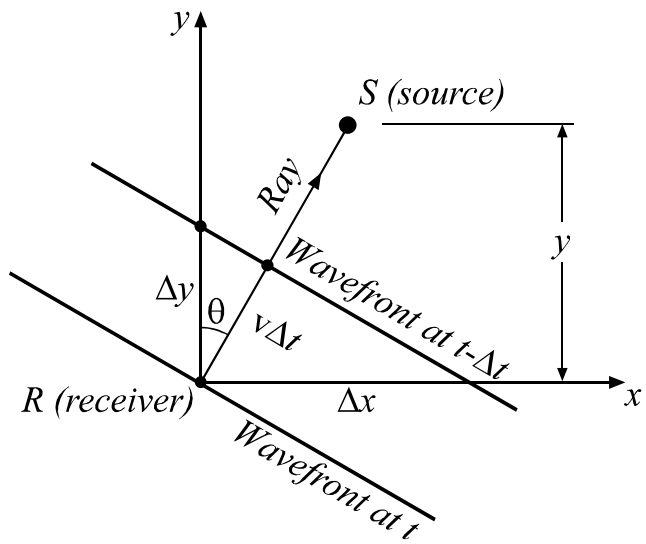

(a) The wavefront is moving backward to source position through migration.

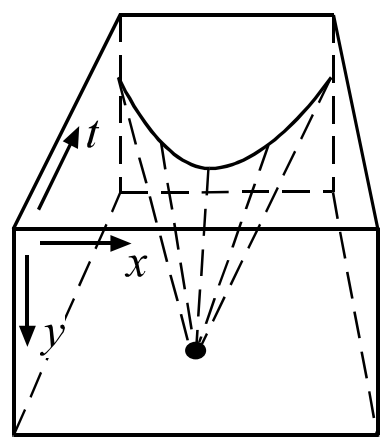

(b) The purpose of migration is to get the spatial information by collapsing the hyperbolic events on the time section.

Fig. 3.1 Illustrative explanation of migration technique

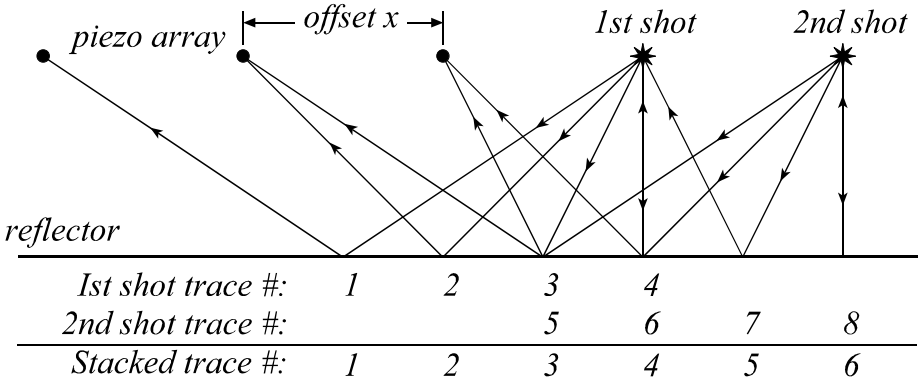

Fig. 3.2 Generating the CMP gather

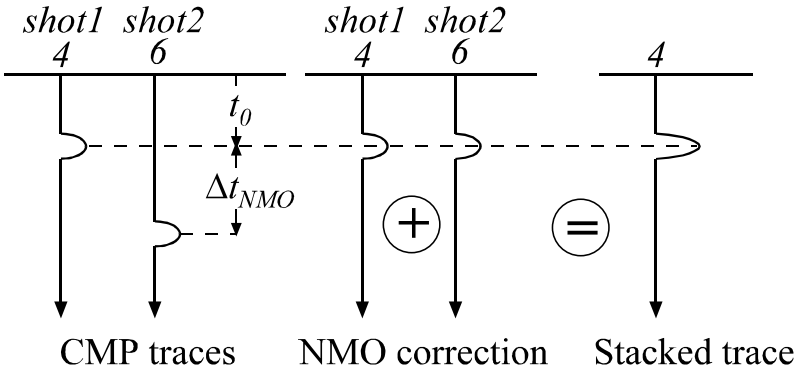

Fig. 3.3 NMO correction and CMP stacking

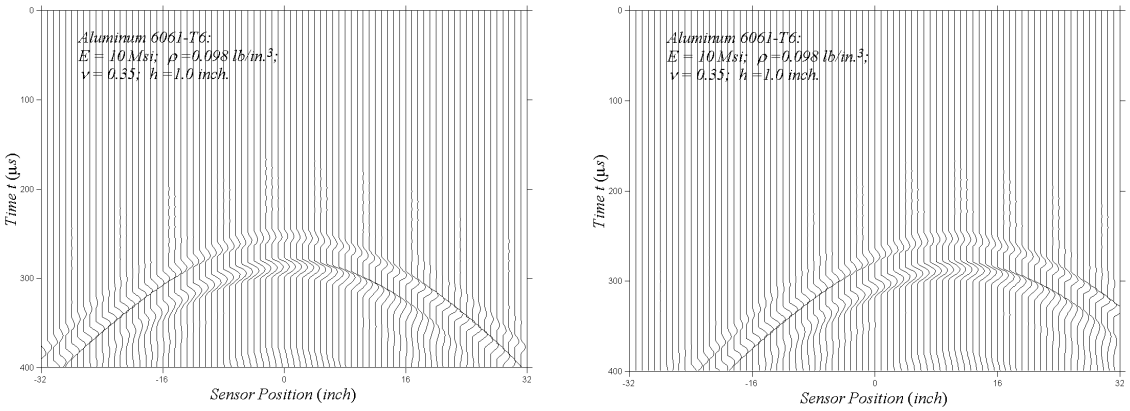

a. shot at $x = 0$, $y = 0$

b. shot at $x = 10$ in., $y = 0$

Fig. 3.4 Reflection waves due to a narrow strip damage

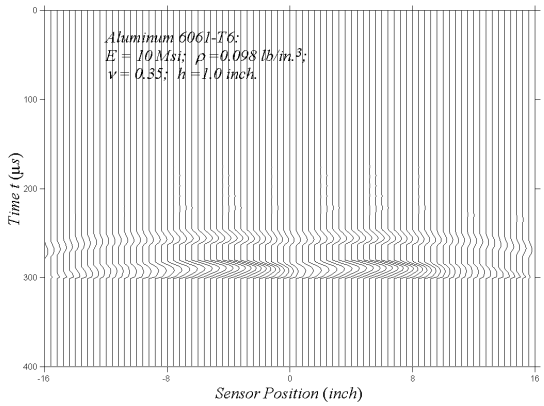

Fig. 3.5 Stacked CMP section

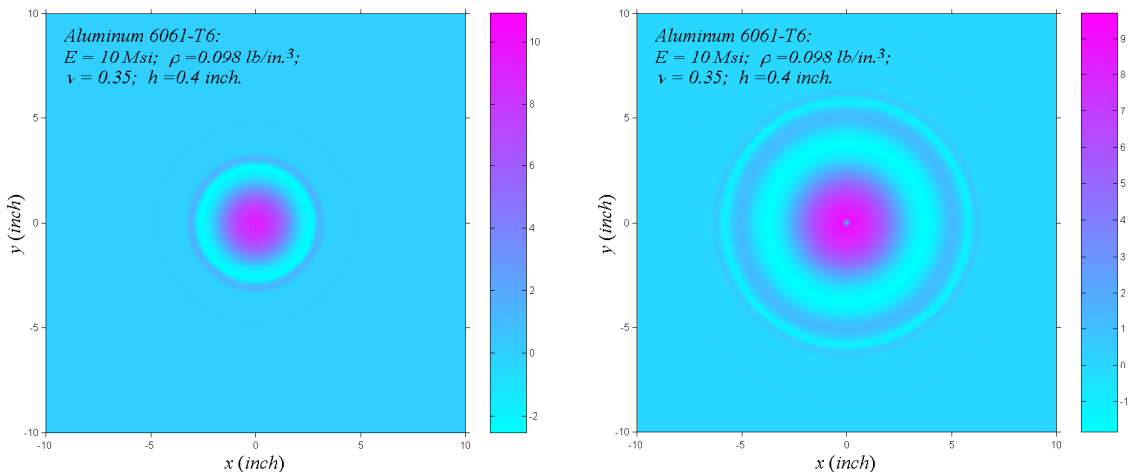

(a) t = 25 μs

(b) t = 50 μs

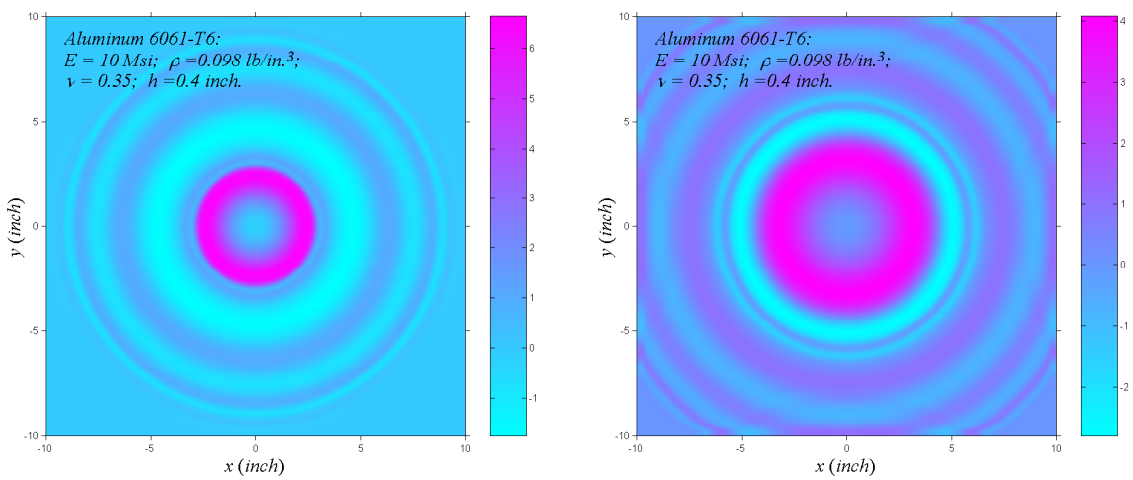

(c) t = 75 μs

(d) t = 100 μs

Fig. 3.6 Four snapshots of propagation waves governed by two-way wave equation

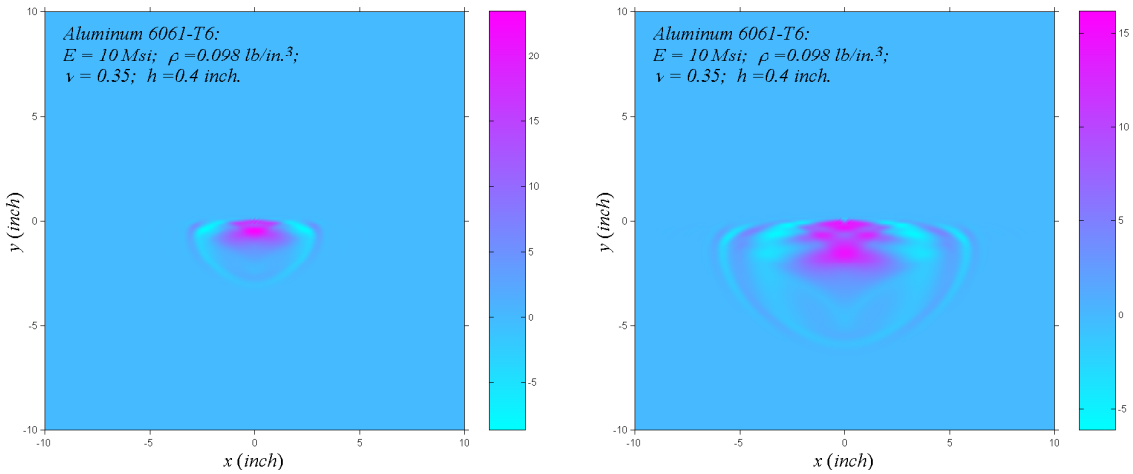

(a) t = 25 μs

(b) t = 50 μs

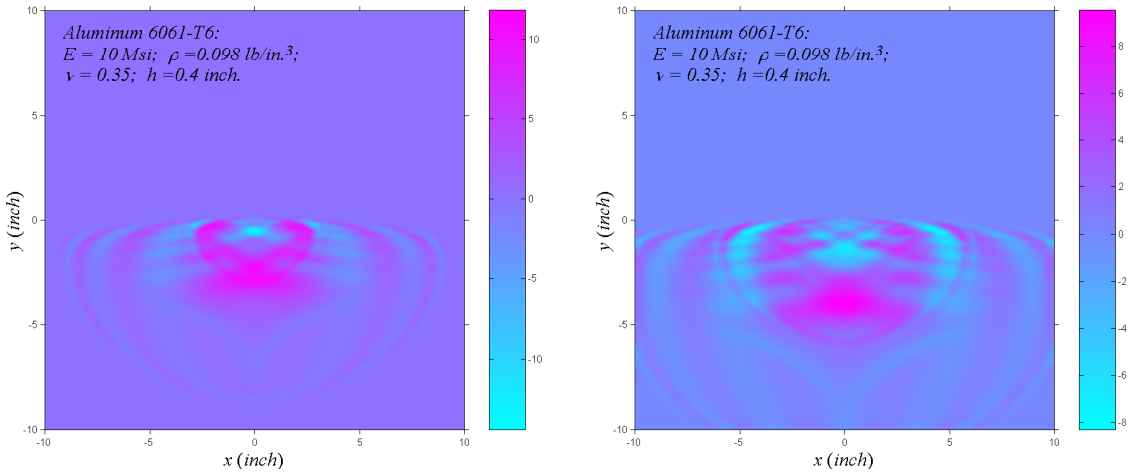

(c) t = 75 μs

(d) t = 100 μs

Fig. 3.7 Four snapshots of propagation waves governed by one-way wave equation

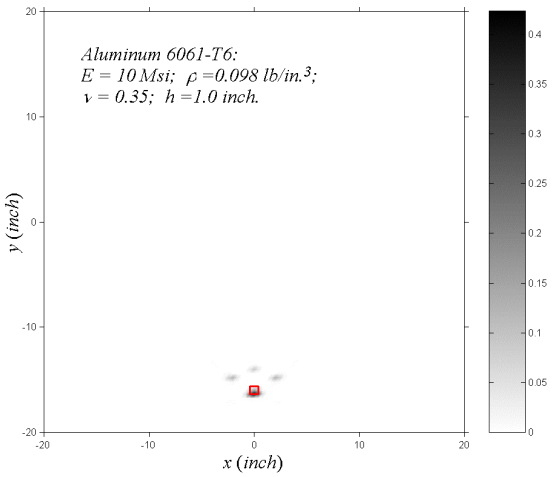

(a) half cycle of a sine function

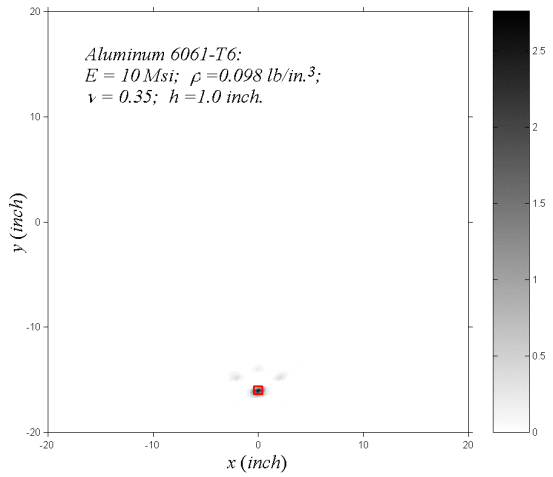

(b) single cycle of a sine function

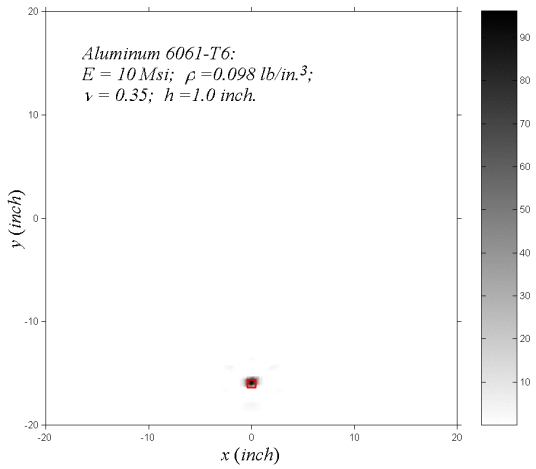

(c) sinusoid modulation function

Fig. 3.8 Comparison of migration images from different excitation signals (f_0 = 40kHz, p = 4)

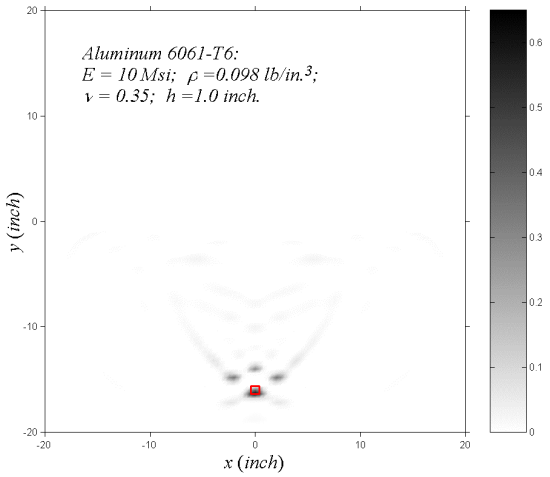

(a) Square shape damage with dimension 0.8×0.8 centered at (0,-16)

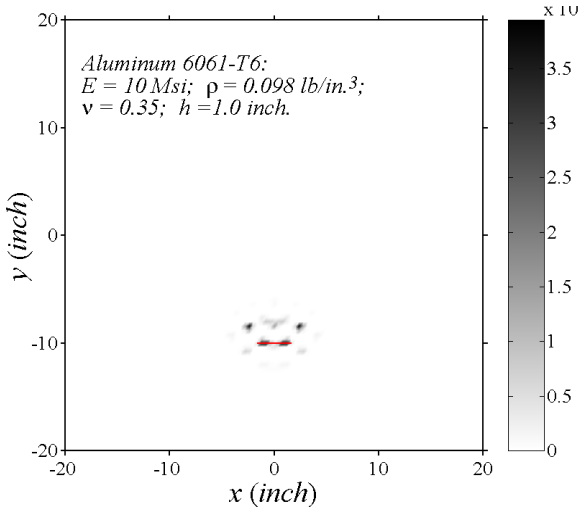

(b) Rectanglar shape damage with dimension 3.2×0.2 centered at (0,-10)

Fig. 3.9 Comparison of migration images for different damage shapes (p = 2)

4 Prestack Migration: Multiple Asymmetric Damages

In this chapter, feasibility of applying prestack migration to image the plate and detect multiple asymmetric damages is studied using synthesized data. First, the reverse-time prestack migration process is discussed. Then, an excitation-time imaging condition specifically for the migration of waves in a plate is introduced based on ray-tracing concepts and the asymptotic properties of flexural wave velocities. Lastly, the numerical results are presented to show that two assumed discrete damages could be correctly identified through the images in the prestack migration. The influence of number of sensors/actuators on the resolution of the damage in the plate is also discussed in this section.

4.1 Prestack migration

4.1.1 Concepts

For a distributed actuator/sensor monitoring system, each actuator can excite A_0 mode Lamb waves in the plate. All the sensors collect the back-scattering waves and a time section is assembled. In poststack migration, the time sections of different excitations are NMO corrected and added up to develop a zero-offset section, which is the data form to be used in the migration (Claerbout, 1971). This stacking process increases the Signal-to-Noise Ratio (SNR) and thus improves the quality of the migration. However NMO correction is based on the assumption that the reflectors are flat layers, thus poststack migration is only suitable for the case that actuators/sensors are distributed along an array and the interfaces of the flaws are parallel to this array. Further, if the recorded signals are transformed into a zero-offset data before the migration, the information of reflection amplitude relating with actuator-sensor distance (offset) might be lost. In this chapter, time sections without correction from a single excitation is used to execute the migration. The stacking is processed after the migration, so called prestack

migration, and applied to the migrated images. The most attractive feature of the prestack migration is that it releases the limitation of the fixed pattern of distributed actuators/sensors and it has the potential to identify the location, shape, and form of arbitrary number of damages.

The prestack migration adopted in this chapter is based on the full-way wave equation rather than the one-way wave equation. In geophysics, most applications use one-way wave equation based migration. The reason is that the receiver is placed on the Earth's surface and its recorded signal is the upward traveling waves. Then the migration works as downward continuation of the reflection wave field. For SHM cases, the actuator may be placed any region of interest on the surface or inside the plate and it can receive reflection energy from any coming direction. Thus the two-way wave equation has to be used in migration to back-propagate the waves received by the sensors. Another consideration in geophysics when using one-way wave equation based migration is to avoid imaging multiple reflection energy. This is not a concern in SHM because incipient flaws are usually small in size and the structures could be modeled as homogeneous materials in the migration process. In fact, because the locations and dimensions of the damages are unknown before the migration is accomplished, it is unlikely to estimate the material distribution. However, the one-way wave equation based prestack migration might be necessary when the boundaries of the structure need to be taken into consideration. By using full-way wave migration, for a single flaw it will develop two images that are symmetrical with respect to the sensor array. To uniquely determine the real location of the flaw, an auxiliary migration along a different direction is necessary.

Reverse-time finite difference migration is used in this study. The finite difference algorithm discussed in Chapter 2 is used to perform the migration. The time section is reversed with respect to time first. Each trace was treated as a time-dependent boundary condition of transverse deformation velocity $\dot{w}$ at the grid point corresponding to the sensor. Because the finite difference algorithm used is a two step time splitting method, the time step in the migration is twice the time step in synthesizing the wave field. In real applications, the time step for the migration is equal to the sampling interval of the

Analog/Digital (A/D) device. By applying the boundary conditions at all sensor locations at each time step, the received reflection waves are back-propagating towards the damages or secondary sources.

4.1.2 Excitation-time imaging condition

Prestack migration uses the finite offset time section, thus it has a different imaging condition than poststack migration, in which the entire plate is imaged simultaneously at the end of extrapolation. The excitation-time imaging condition proposed by Chang and McMechan (1986) is used in this study. The imaging condition is based on a concept that if both the source and the recorded wave are extrapolated, the reflectors exist at the places where these two waves are in phase to each other. By this condition, a point is imaged at its excitation time. Excitation time is defined as the moment when the point is excited by the energy from the actuator. This imaging condition is explicit and each point in the image space has its own image time. Thus, at each time step $i\Delta t$, imaging is processed at all the grid points located on a locus defined by

$$t_d = (N - i + 1)\Delta t \tag{4.1}$$

where t_d is the one-way travel time from the loading point to the points, N is the total time steps. The direct arrival time can be obtained by extrapolating the source through a finite difference algorithm. In this study, it is done by an approximation based on ray-tracing concepts. Based on Fermat's principle, an arbitrary ray path $\vec{P}$ in a heterogeneous medium with wave velocity distribution $C(x, y)$ is governed by the ray equation (Lee and Stewart, 1981),

$$\frac{d}{dp}\left(\frac{1}{C(x,y)}\frac{dx}{dp}\right) = \frac{\partial C(x,y)}{\partial x} \tag{4.2a}$$

$$\frac{d}{dp}\left(\frac{1}{C(x,y)}\frac{dy}{dp}\right) = \frac{\partial C(x,y)}{\partial y} \tag{4.2b}$$

where as shown in Fig. 4.1,

$$dx = dp\cos\theta, \quad dy = dp\sin\theta$$

Eq. (4.2) can be further transformed into

$$\begin{cases} \dfrac{dx}{dt} = C(x,y)\cos\theta \\ \dfrac{dy}{dt} = C(x,y)\sin\theta \\ \dfrac{d\theta}{dt} = \dfrac{\partial C}{\partial x}\sin\theta - \dfrac{\partial C}{\partial y}\cos\theta \end{cases} \tag{4.3}$$

The first two equations in eq. (4.3) specify the change of ray positions with respect to time, and the third equation specifies the change of ray direction with respect to time. Then, summing the travel time on the all segments along the ray path gives the direct arrival time

$$t_d = \int_{\vec{P}} \frac{dp}{C(x,y)} = \sum_i \frac{\Delta p}{C(x,y)} \tag{4.4}$$

If the damage dimension is ignored and the plate is considered as homogeneous, θ in eq. (4.3) is a constant, which means that the wavefront is a circle centering at the loading point and a ray path is a straight line along the radius r. It appears that the direct arrival time simply equals $t_d = r / C_d$, where C_d is a wave velocity determined for calculating the imaging condition.

Assuming the waves in a plate have a form like $e^{i(\omega t - \gamma r)}$, where γ represents the wavenumber, the slow flexural wave w_1 and fast flexural wave w_2 can be decoupled from each other by eq. (2.8) as

$$(\nabla^2 + \gamma_i^2) w_i = 0, \quad i = 1, 2 \tag{4.5}$$

where

$$\gamma_i^2 = \frac{\rho h \omega^2}{2D}\left[\sqrt{(S-R)^2 + \frac{4D}{\rho h \omega^2}} \pm (S+R)\right]$$

$$R = \frac{h^2}{12}, \quad S = \frac{D}{\kappa^2 G h}$$

Thus the velocities V_1, V_2 of slow and fast flexural waves are frequency dependent. When frequency is very high, as it occurs in ultrasonic testing, it can be shown that

$$V_1 = \frac{\omega}{\gamma_1} \rightarrow \kappa C_s \tag{4.6}$$

$$V_2 = \frac{\omega}{\gamma_2} \rightarrow \sqrt{\frac{2}{1-\nu}} C_s \tag{4.7}$$

i.e., the velocity of slow flexural waves and fast flexural waves approach the velocities of Raleigh waves and plate extensional waves, respectively, as shown in Fig. 4.2. In both numerical simulation and experiments, the arrival of fast flexural waves is hardly discernable. The reason might be that most of the energy is propagating in the velocity of shear waves C_s, which is close to the velocity of slow flexural waves. Thus, in this study, the velocity used to estimate the direct arrival time is approximately chosen as

$$C_d = C_s \tag{4.8}$$

The imaging condition locus for each extrapolation time step is calculated in advance and used as a reference table in migration process. At each extrapolation step, those points on which the direct arrival time locus cross with back-propagating wavefront are imaged in terms of the velocity of transverse deformation $\dot{w}$. The imaging locus does not always across the grid point. In the current study, a point that is not far away from the locus more than $\Delta s/4$ was imaged at this time step. One grid point might be imaged more than a single time during one time section migration, because the stability criterion of finite difference algorithm prevents the locus from passing through one grid space in a single time step. Mean value of the imaging variable is used to image these points. On the other hand, all the loci for all time steps may not cover all the grid points. Thus interpolation for the image is necessary. One alternative to apply interpolation is in the process of extrapolation, or interpolation in terms of time step. This will lower the speed of migration and increase the memory requirement of the calculation. Another option to do it is after the whole extrapolation, which means that the interpolation was totally done in spatial domain and would turn out a smoother image. To compensate the effect that the

waves attenuate over the travelling distance, the image intensity at one point was multiplied by r, which is the distance between that point and the loading point.

4.1.3 Illustration of reverse-time migration

Fig.4.3 displays four snapshots of back-propagating waves in the process of reverse-time migration at four different times. The reflection wave field is generated from two small damages at point A (-10", -10") and B (4", -16"). The actuator is placed at (-20", 0") with loading-time history described by eq. (2.27) with $P = 0.225\ lb$, $f_0 = 40$KHz and $N_p = 3$. The time at which a snapshot is taken is labeled in the caption of each frame, and these times were counted from the recording start-up point of the time section. Thus the real time of each frame counting from the beginning of the migration process should be the time span of the time section (800μs) minus the labeled time. The dashed line superimposed on each snapshot represents the imaging condition locus (points with constant direct arrival time) at this moment. The two small circles represent the target damages. This figure illustrates how reverse-time migration back-propagates the recorded reflection waves and how the excitation-time imaging condition is applied to image multiple damages. In frame (a), the recorded wave field is extrapolated and begins to propagate towards the damages. The reflected energy from damage A is focused back to its secondary source through migration at time 278 μs (frame b), where the imaging condition locus is coincident with the wavefront of downward (negative y-direction) wave field. The hyperbolic event induced by damage B is collapsed into a point diffractor at the right position at 153 μs (frame c). In frame d, the reflection energy continued its downward propagation, and the wavefronts were much like an image of over-migration. The waves propagate divergently and the wavefront would not be coincident with the shrinking imaging condition locus again, thus no new point would be imaged.

Because the detectability of different damages is strongly dependent on the incidence angle of ultrasonic waves, migration of time sections from a single actuator might not give a complete image of the damages. For distributed actuator/sensor plate structure, each time one actuator is used to excite flexural waves while all the sensors collect the reflection signals, then a time section is assembled. Applying migration to

each time section gives an image of the plate. A complete image could be obtained by adding up all these images. This stacking process after the migration also increases the SNR. The more actuators are used, the higher SNR and the better resolution can be obtained for the final image. However, increasing the times of migration will increase the computation burden, which is not favorable in real time SHM.

4.2 Numerical results

4.2.1 Reflection wave from two discrete damages

A plate with dimension 40 in.×40 in. is modeled in the current study. A 200 × 200 finite difference mesh is superimposed on the plate region. The origin of the coordinate system is set at the center of the plate. Two small damages, shown in the following figures as the two small circles, are modeled as point diffractors at (4", -16") and (-10", -10"), respectively. The equivalent bending stiffness D at the grid points representing the damages is chosen as one eighth of the plate's bending stiffness. The loading-time history described by eq. (2.27) with $P = 0.225\ lb$, $f_0 = 40$KHz and $N_p = 3$, is applied at the center of the plate. Fig. 4.4 displays a snapshot of the synthesized reflection wave field as a whole view of the plate at $t = 300\ \mu s$. At this time, the wave has hit two damages. In this figure, the amplitude of the velocity of transverse deformation $\dot{w}$ at the grid points is shown as a contour plot. It can be observed that two point diffractors are illuminated by the incident waves sequentially, depending on the distance between the damage location and the loading point. The reflection waves radiate from each damage, acting like waves from a point source. Thus, a damage (or reflector) can be treated as a secondary source, generating waves. This phenomenon is one of the foundations of applying migration technique to detect damages in structures. Another observation from this figure is that the amplitude of reflection waves is dependent on the incidence angle. For the points along the direction of a line connecting a diffractor and the loading point, the amplitude reaches a maximum. The amplitude decreases with the increase of the angle deviating from this direction.

Fig. 4.5 shows the reflection wave field in the form of time section in geophysics. The abscissa represents the position of sensors located at $y = 0$, which is the spatial grid point in the simulation where the waves are recorded. The ordinate represents the propagating time of the waves. Each vertical line (a trace) is a time history of $\dot{w}$ at the corresponding point. For clarity, only every second trace is plotted in Fig. 4.5. The fluctuation of a line represents the amplitude change of $\dot{w}$. In the figure, the direct arrival of incident waves from the actuator to sensors has been muted by subtracting the received wave field for a plate without damage from the actual wave field with damages. As shown in the figure, the time span (800 μs) is chosen sufficiently long enough to ensure that all the sensors can pick up the whole length of the reflection wave package for both point diffractors. Contrary to poststack migration, prestack migration does not impose any restriction that limits on the span of sensors inherited in Normal Moveout stacking process. Thus all the traces recorded at the points along a horizontal line crossing through the plate could be used to execute the migration. With the increase of the span of sensors, the artifacts in the migration image due to the data truncation can be reduced to a minimum. In this study, the span of sensors is conservatively chosen as from x = -32" to 32" to avoid the influence from the edges of the plate. The time section provides the information of reflection events in time domain and is the data form that is practically obtainable in SHM. Two hyperbolic reflection events can be noticed in the figure. After migration, these two hyperbolic events will be collapsed into two damage locations. The hyperbolic curve with a peak on the left side indicates the reflection wave from a point reflector (-10", -10"), other reflection wave from (4", -16"). Thus, through migration, the information of reflection events can be transferred from time domain to space domain.

4.2.2 Migration results and discussions

This section shows some images obtained by the prestack reverse-time migration. The material constants and the dimensions of the plate have been given in Fig. 4.5. The plate, which is discretized by 200×200 finite difference mesh, is imaged at each extrapolation step by extracting the velocity of transverse deformation $\dot{w}$ at each grid point, and is displayed as a gray scale contour plot. In the figures, the circles with solid

line represent the target damages. From Figs. 4.6-4.8, the sensors are assumed to be placed at each grid point along the *x*-axis, ranging from (-32, 0) to (32, 0). Nine of the sensors also function as actuators, which are located ranging from (-20, 0) to (20, 0) with an interval of 5 in.. Each actuator gives one shot to excite A_0 mode Lamb waves. The traces collected by all the sensors are used to assemble the time section.

Fig. 4.6 gives an example of the migration images. Fig. 4.6a is the image migrated from a single shot generated by an actuator located at (-20", 0"). Fig. 4.6b is the image stacked from migration images of the time sections from nine actuators. Figs. 4.6a and b show that the prestack migration successfully propagated the reflection energy back to the secondary sources, and two damages are clearly shown in the plate image. The locations of damage's images are very close to the real locations of the target points, although there are some small discrepancy for the dimensions, shapes and locations between resulting images and real damages. The errors might result from the use of narrow banded excitation signals. To obtain perfect image, the excitation should be a spike signal to ensure a high resolution. Due to the dispersive properties of the Lamb waves, a wide banded signal will distort progressively during its propagation. Thus a narrow banded signal is used as the excitation. In this study the narrow banded waves have not been deconvoluted, and the duration time of the source wavelet would worsen the image. After the traces are reversed in time, an end point of the source wavelet package actually becomes a wavefront during the migration progress. Thus the wavefront imaged according to excitation imaging condition is not a real wave front, and thus there is a deviation by the value of duration length of the source package. This will also introduce an error to the location of imaged damages. From the results, it is also observed that there is a strong direction dependence of the images (stronger in the direction of wavefront propagation), which resulted from the fact that the reflection amplitude of a diffractor is angle-dependent. By comparing Figs. 4.6a and b, it is evident that the image after stacking has much better quality than the image from a single shot. It is expected that the stacking process will also suppress the effect of real noise and improve the performance of the migration, which will be pursued in the experimental studies.

However, it should be emphasized that the time required to carry out the prestack migration for N time sections from N actuators is N times of the time spent for a single shot, which is not favorable in real-time monitoring.

Fig. 4.7 shows migration images that the side effect of non-spike excitation discussed in Fig. 4.6 is compensated. Fig. 4.7a is the image from a shot initiated by the actuator at the center of the plate. The stacked image from nine shots is shown in Fig. 4.7b. For compensating the location error caused by the non-spike-like source wavelet, half of the duration time of the wavelet is subtracted from the direct arrival time in the calculation of the imaging condition table. The resulting images in Fig. 4.7 show that the image quality is much improved after the compensation. The images of the damages overlapped the targets more accurately than the images in Fig. 4.6. The effect of angle dependence of the image on the source position is also weakened.

Fig. 4.8 shows a stacked image of the plate obtained from the one-way wave equation (3.17) based migration. As shown in Figs. 4.6, 4.7 and 4.9, in the two-way wave migration, a pseudo image together with the right image of each damage appeared symmetrically with respect to the x-axis, along which the sensors are distributed. Because both damages are located below the x-axis, and intentionally, downward extrapolation is chosen, the resulting image shows the correct locations of damages and no pseudo image appeared. In this case, a damage located above the x-axis is not imaged. This figure implies that only if the sensors were placed along the edge of a plate, the one-way wave equation based migration can be used in SHM. It is also observed that there is energy scattered around the target damages. The reason might be that the one-way wave equation used has not been corrected to preserve the dispersion relation of the real full-way waves.

Fig. 4.9 displays plate images from migration with fewer actuators/sensors. Nine piezoelectric elements form a line array ranging from (-24", 0) to (24", 0) with a spacing of 6". All the piezoelectric elements function as sensors. In Fig. 4.9a, all the sensors also act as actuators. In Fig. 4.9b, only the three sensors at (-24", 0"), (0", 0") and (24", 0") are chosen to excite the A_0 mode Lamb waves. It is expected that the fewer the sensors/actuators, the poorer the resolution and quality of images may result. However,

the number of actuators/sensors in a real structural monitoring system should keep as small as possible so that the monitoring system will not add extra complexity and reduce the strength and performance of the structure. Fig. 4.9 demonstrates that prestack migration is still applicable when very few actuators/sensors are used. The number of sensors is cut down dramatically comparing with the case shown in Fig. 4.7. The damage imaging quality of both Fig. 4.9a and Fig. 4.9b is less sharp than that of the stacked image in Fig. 4.7b, but they both give a clear indication of the existing damages. In Fig. 4.9b, there is a noticeable error for the imaging of the location of the target damages. It could be concluded from the comparison among these images that the number of actuators, which determines how many images will be stacked, is more critical than the number of sensors as a factor of affecting the accuracy of the damage detection. That the image quality is not deteriorated significantly with few sensors/actuators is an advantage for prestack migration over poststack migration. The reason is that poststack migration is based on NMO corrected section, which is highly dependent on the interval between sensors.

Finally, it should be emphasized that in this chapter damages are modeled as point diffractors, which may not reflect the reality. Knowing that every damage with a solid area can be treated as a summation of certain point reflectors, it is believed that prestack migration is capable of detecting and locating any shape, any dimension of the damages.

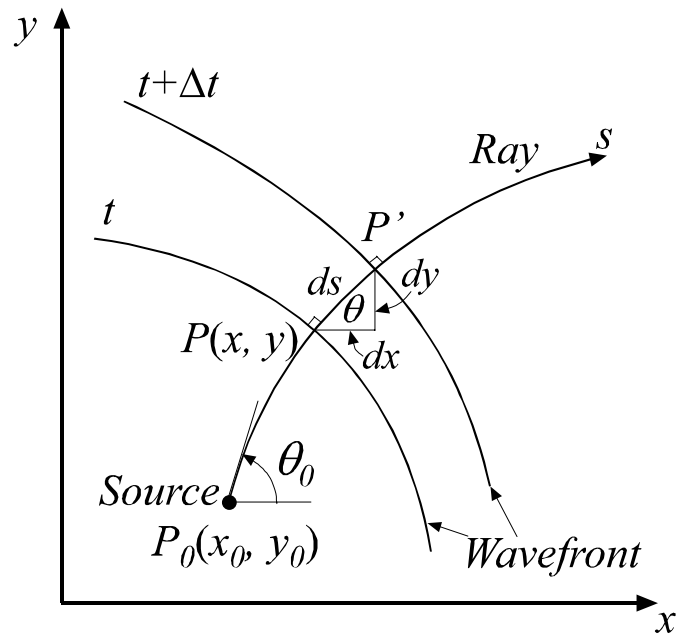

Fig. 4.1 Scheme of ray-tracing algorithm

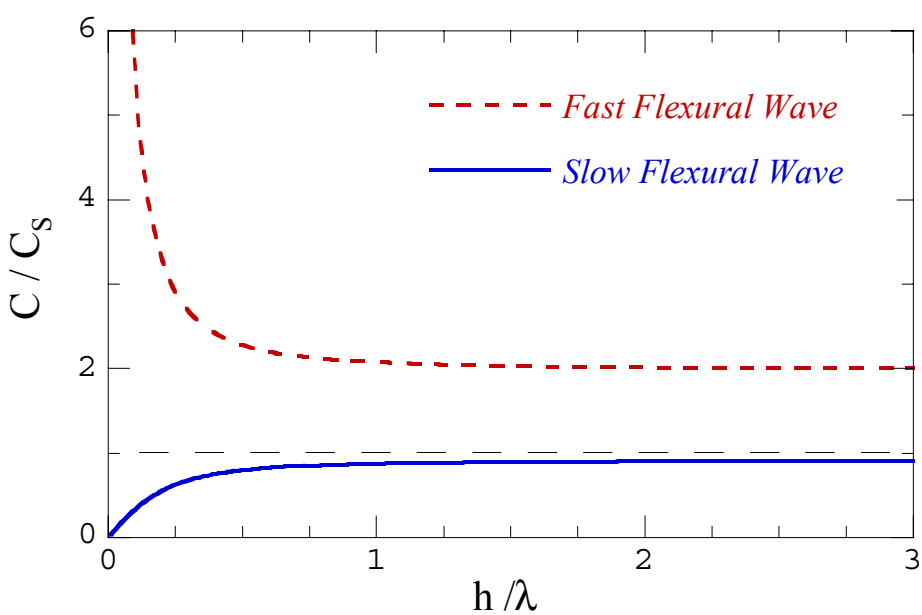

Fig. 4.2 Asymptotic properties of A_0 mode Lamb waves ($\nu = 0.5$)

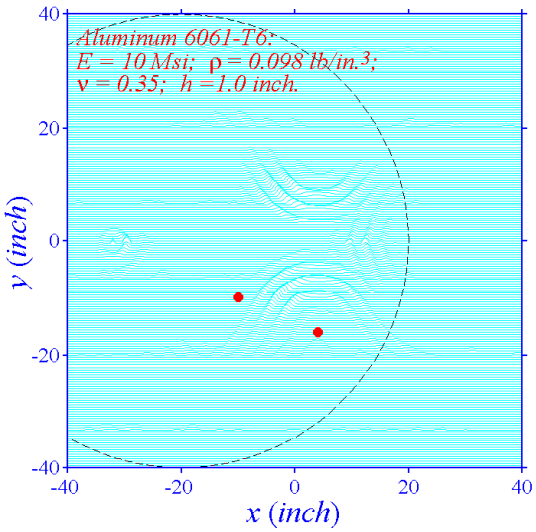

(a) t = 366 μs

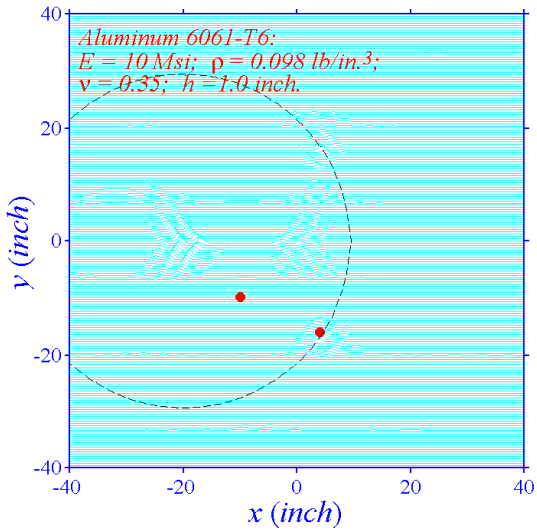

(b) t = 278 μs

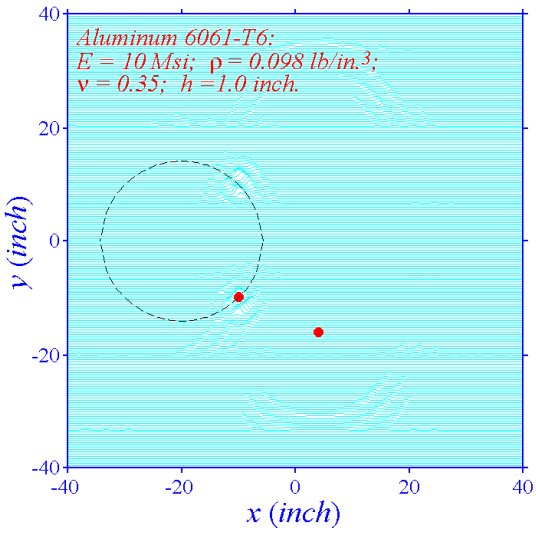

(c) t = 153 μs

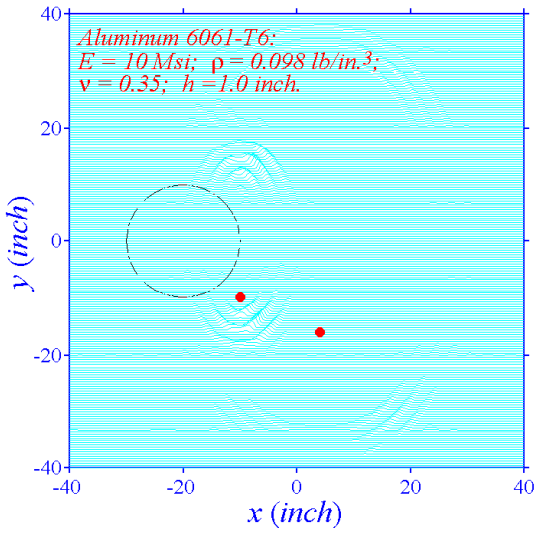

(d) t = 119 μs

Fig. 4.3 Snapshots of back-propagating waves in the reverse-time migration

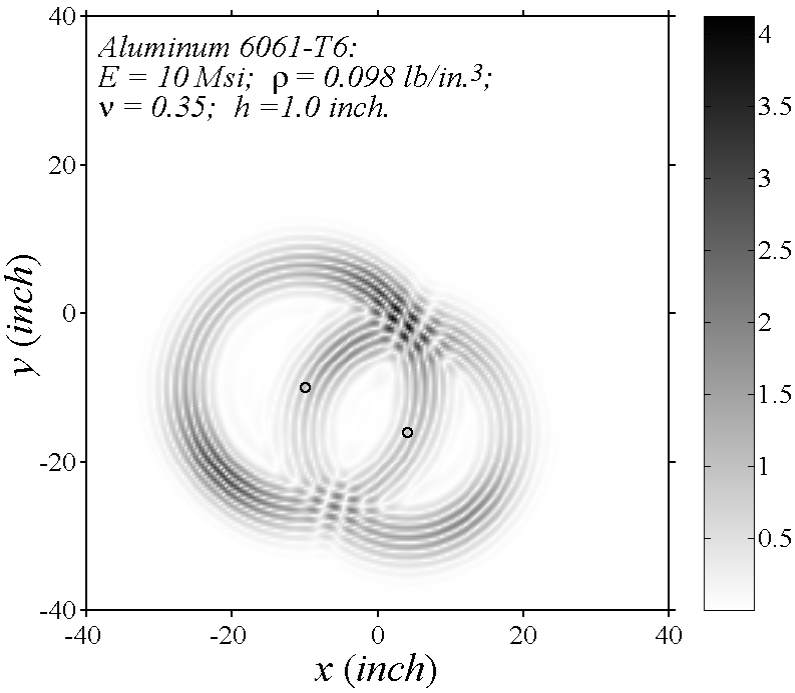

Fig. 4.4 Snapshot of the reflection wave field from two small damages at t = 300 μs.

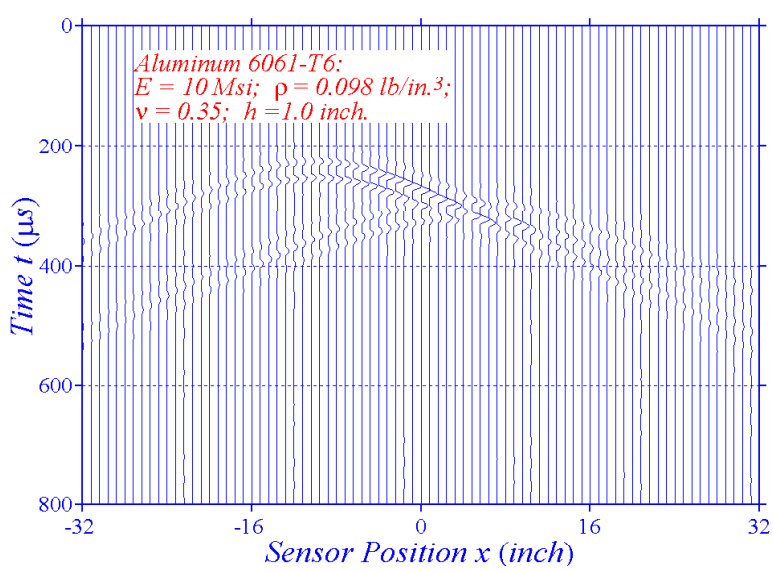

Fig. 4.5 A time section that is used to execute prestack migration

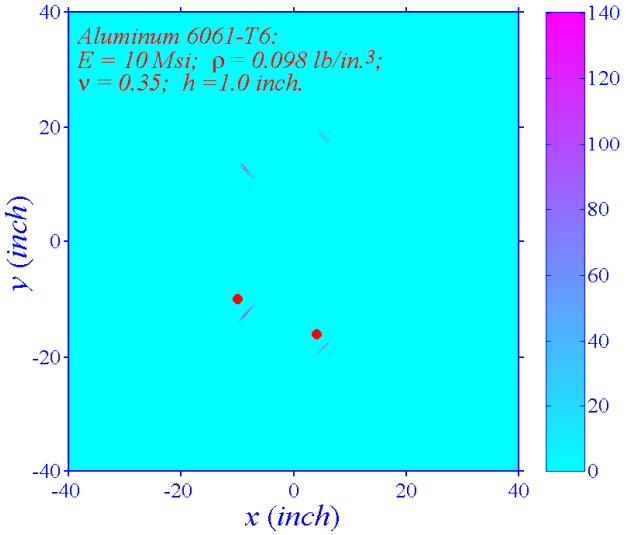

(a) a single actuator at (-20",0)

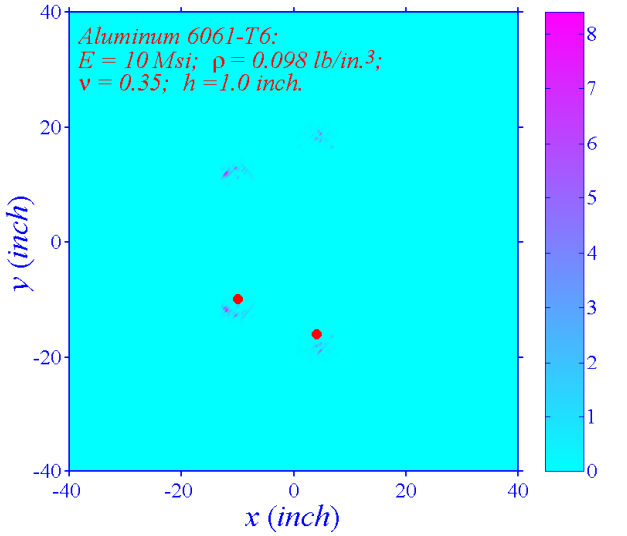

(b) the stacked image from regularly spaced 9 actuators

Fig. 4.6 Image of two small damages migrated from the synthetic data

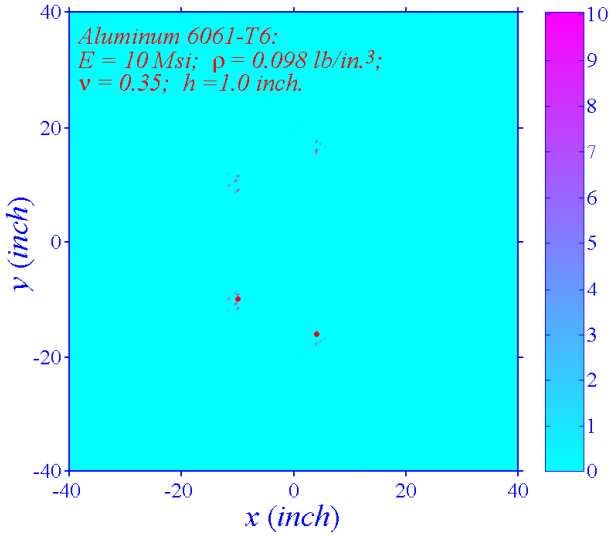

(a) actuator at (0", 0")

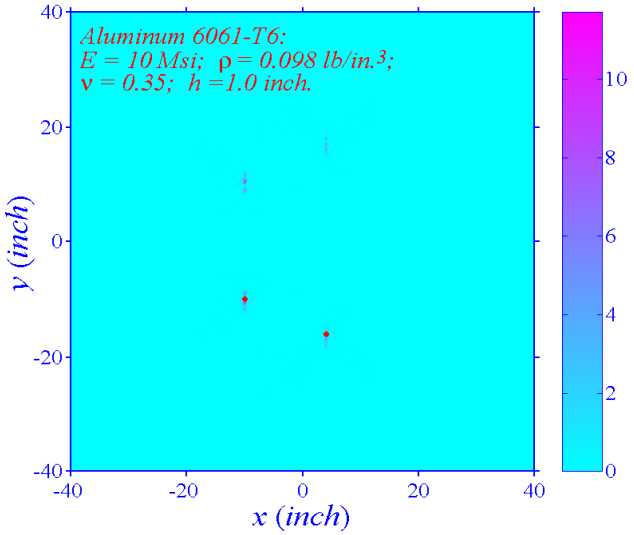

(b) stacked image

Fig. 4.7 Image of two small damages migrated from the synthetic data (The side effect of non-spike excitation was compensated in the migration)

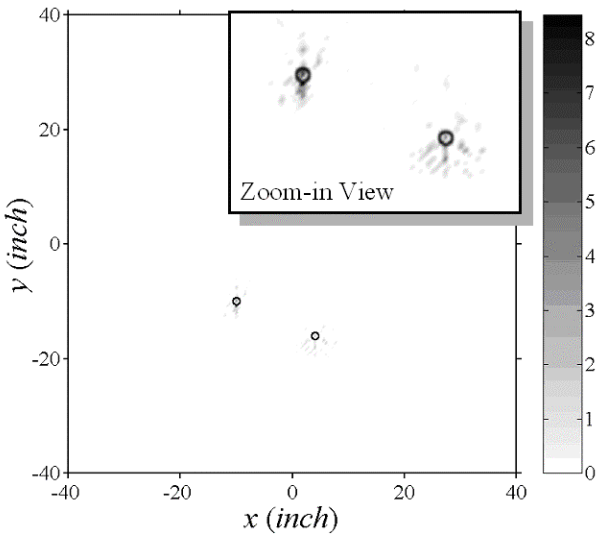

Fig. 4.8 Stacked image from one-way wave equation based migration

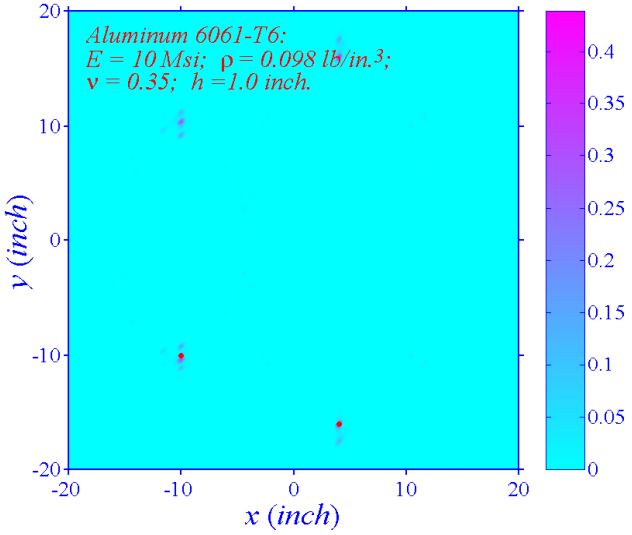

(a) stacked from 9 images

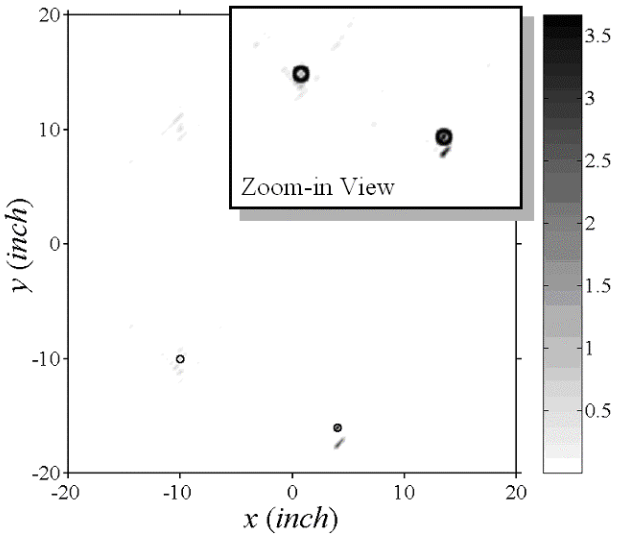

(b) stacked from 3 images

Fig. 4.9 Image of two small damages migrated from the synthetic data (The migration was done from a small number of sensors/actuators)

5 Sensor/Actuator Models and Experimental Verification

In this chapter, an experimental work is pursued to validate the feasibility of applying migration techniques to process the actual wave signals and identify the structural anomalies. First, an analytical model of wave signals generated and collected by piezoelectric (PZT) actuators/sensors is derived. This model combines the analytical solution of MPT (Chapter 2) and the piezoelectric effect of the actuators/sensors (constitutive relations), thus the voltage output of a sensor can be obtained directly from the voltage input of an actuator. After the configuration of experimental setup is presented, the experimental results show that the signals recorded in the experiment have excellent repeatability and agree well with the calculation data from the analytical model. The experimental facilities are thus proven to have the capability of generating and receiving Lamb waves accurately. Finally, the migration results from the reflection waves of an artificial damage are presented. It is shown that the existence of the damage is correctly revealed through migration process in the experiment as it has been shown in the numerical simulation.

5.1 Modeling Piezoelectric Sensors/Actuators

According to the IEEE compact matrix notation (IEEE, 1978), the constitutive equations of a linear piezoelectric material are written as

direct piezoelectric effect: $$\mathbf{D} = \boldsymbol{\varepsilon}^{T}\mathbf{E} + \mathbf{d}\boldsymbol{\sigma} \tag{5.1}$$

converse piezoelectric effect: $$\mathbf{S} = \mathbf{s}^{E}\boldsymbol{\sigma} + \mathbf{d}\mathbf{E} \tag{5.2}$$

where $\mathbf{D}$ and $\mathbf{E}$ are the electric displacement and electric field, respectively. $\mathbf{S}$ and $\boldsymbol{\sigma}$ are the mechanical strain and stress, $\mathbf{d}$, $\boldsymbol{\varepsilon}^{T}$, and $\mathbf{s}^{E}$ are the piezoelectric strain constant, dielectric permittivity, compliance constant, respectively. The superscripts E and T indicate that the values of the constants are obtained at a constant electrical field and

constant stress, respectively, and these superscripts will be omitted in the expressions hereafter. For the PZT disk used in this study, the piezoelectric effect has conical symmetry and the mechanical property is transversely isotropic, thus nonzero independent material constants are reduced to d_{31}, d_{33}, d_{15}; ε_1, ε_3, s_{11}, s_{33}, s_{55}, s_{12}, s_{13}, and other constants are given as,

$$d_{32} = d_{31},\ d_{24} = d_{15}\ ;\ \varepsilon_2 = \varepsilon_1;$$

$$s_{22} = s_{11},\ s_{23} = s_{13},\ s_{44} = s_{55},\ s_{66} = 2(s_{11} - s_{12})$$

Here the poling direction is assumed to be 3, perpendicular to the surface of the plate (or the PZT disk). The constitutive relations then can be written explicitly as

$$\begin{Bmatrix} D_1 \\ D_2 \\ D_3 \\ \varepsilon_{11} \\ \varepsilon_{22} \\ \varepsilon_{33} \\ \gamma_{23} \\ \gamma_{13} \\ \gamma_{12} \end{Bmatrix} = \begin{bmatrix} \varepsilon_1 & 0 & 0 & 0 & 0 & 0 & 0 & d_{15} & 0 \\ 0 & \varepsilon_1 & 0 & 0 & 0 & 0 & d_{15} & 0 & 0 \\ 0 & 0 & \varepsilon_3 & d_{31} & d_{31} & d_{33} & 0 & 0 & 0 \\ 0 & 0 & d_{31} & s_{11} & s_{12} & s_{13} & 0 & & 0 \\ 0 & 0 & d_{31} & s_{12} & s_{11} & s_{13} & 0 & 0 & 0 \\ 0 & 0 & d_{33} & s_{13} & s_{13} & s_{33} & 0 & 0 & 0 \\ 0 & d_{15} & 0 & 0 & 0 & 0 & s_{55} & 0 & 0 \\ d_{15} & 0 & 0 & 0 & 0 & 0 & 0 & s_{55} & 0 \\ 0 & 0 & 0 & 0 & 0 & 0 & 0 & 0 & s_{66} \end{bmatrix} \begin{Bmatrix} E_1 \\ E_2 \\ E_3 \\ \sigma_{11} \\ \sigma_{22} \\ \sigma_{33} \\ \sigma_{23} \\ \sigma_{13} \\ \sigma_{12} \end{Bmatrix} \tag{5.3}$$

Ignoring the in-plane external electric field ($E_1 = E_2 = 0$) and assuming plane stress condition, eq. (5.3) in terms of polar coordinate system can be simplified as

$$D_3 = \varepsilon_3 E_3 + d_{31}(\sigma_r + \sigma_\theta) \tag{5.4a}$$

$$\begin{aligned} \sigma_r &= \frac{E_p}{1-\nu_p^2}\left[(\varepsilon_r + \nu_p \varepsilon_\theta) - (1+\nu_p) d_{31} E_3\right] \\ \sigma_\theta &= \frac{E_p}{1-\nu_p^2}\left[(\varepsilon_\theta + \nu_p \varepsilon_r) - (1+\nu_p) d_{31} E_3\right] \end{aligned} \tag{5.4b}$$

5.1.1 Actuator model

Two thin PZT disks are bonded at the same location on the top and bottom surfaces of a plate (Fig. 5.1). With the polarization direction aligned with z-axis, the electrodes of

these two actuators are connected to a same voltage V_{in} with opposite sign. The actuators thus apply equal traction on the two sides of the plate with opposite direction. The resultant bending moment on the plate along the circumference of the actuator is uniform and flexural waves are therefore generated. For a free (unconstrained) PZT without in-plane external electric field and applied stress, the induced in-plane strain by applying a voltage across z-direction in a polar coordinate system can be expressed as

$$\varepsilon_{r_p} = \varepsilon_{\theta_p} = d_{31}E_3 = \frac{d_{31}}{h_p}V_{in} \equiv \Lambda \tag{5.5}$$

where the subscript p refers to PZT actuator and h_p is the thickness of the PZT disk. The piezo actuators are perfectly mounted on the plate and are sufficiently small that it will not affect significantly the plate's stiffness. Λ is the actuation strain. The strain at the interface between the plate and the PZT should be equal to ensure the continuity ($\varepsilon^i_{r_p} = \varepsilon^i_r$, $\varepsilon^i_{\theta_p} = \varepsilon^i_\theta$). Thus, the stress of PZT at the interface from eq. (5.4b) can be written as (combined unstrained strain due to the piezoelectric and the constrained strain of the plate),

$$\sigma^i_{r_p} = \frac{E_p}{1-\nu_p^2}\left[\varepsilon^i_r + \nu_p\varepsilon^i_\theta - (1+\nu_p)\Lambda\right] \tag{5.6}$$

where the superscript i refers to interface of the PZT and the plate. Assuming the strains both for the plate and for the PZT distribute linearly across the plate thickness with a same slope, the normal stresses σ_r are then obtained as:

$$\sigma_r = \frac{2\sigma^i_r}{h}z \tag{5.7a}$$

$$\sigma_{r_p} = \frac{1-\nu}{1-\nu_p}\frac{E_p}{E}\frac{2\sigma^i_r}{h}z - \frac{E_p}{1-\nu_p}\Lambda \tag{5.7b}$$

By use of the moment equilibrium about the neutral axis of the combined PZT disk and the plate ($r < a$, where a is the radius of the PZT disk)

$$\int_0^{h/2} 2\pi r\sigma_r z dz + \int_{h/2}^{h/2+h_p} 2\pi r\sigma_{r_p} z dz = 0 \tag{5.8}$$

the interface stress can be found:

$$\sigma_r^i = \frac{6\Lambda h h_p E_p (h+h_p)}{(1-\nu_p)[h^3 + 2\alpha h_p (3h^2 + 4h_p^2 + 6hh_p)]} \tag{5.9}$$

where

$$\alpha = \frac{1-\nu}{1-\nu_p}\frac{E_p}{E} \tag{5.10}$$

The bending moment induced from piezoelectric effect is assumed to be concentrated along the circumference of the PZT disk with radius $r = a$, and it can be evaluated by

$$M_r\big|_{r=a} = \int_{-h/2}^{h/2} \sigma_r z dz = C_{mV} V_{in} \tag{5.11}$$

where the voltage-moment conversion coefficient is defined by

$$C_{mV} = \frac{h^3 d_{31} E_p (h+h_p)}{(1-\nu_p)[h^3 + 2\alpha h_p (3h^2 + 4h_p^2 + 6hh_p)]} \tag{5.12}$$

Referring back to the analysis in Chapter 2, the expression for the bending moment can be obtained by substituting eq. (2.17) into eq. (2.7a)

$$\widetilde{M}_r = \frac{\rho\omega^2 D}{\kappa^2 GB}\frac{d}{dr}\left[\frac{d^3}{dr^3} + \frac{1+\nu}{r}\frac{d^2}{dr^2} + (A - \frac{\kappa^2 GB}{\rho\omega^2} - \frac{2-\nu}{r^2})\frac{d}{dr} + (A - \frac{\kappa^2 GB}{\rho\omega^2})\frac{\nu}{r} + \frac{2-\nu}{r^3}\right]\widetilde{w} \tag{5.13}$$

Substituting eq. (2.16) into eq. (5.13) yields

$$\widetilde{M}_r = \frac{\rho\omega^2 DC}{\kappa^2 GB} F(r) \tag{5.14}$$

where function $F(r)$ is defined as

$$F(r) = (A - \frac{\kappa^2 GB}{\rho\omega^2} - k_1^2)\left[\frac{k_1^2}{2}H_2^{(2)}(k_1 r) - \frac{\nu k_1}{r}H_1^{(2)}(k_1 r) - \frac{k_1^2}{2}H_0^{(2)}(k_1 r)\right]$$
$$+ (A - \frac{\kappa^2 GB}{\rho\omega^2} + k_2^2)\left[\frac{k_2^2}{2}H_2^{(2)}(-ik_2 r) - \frac{i\nu k_2}{r}H_1^{(2)}(-ik_2 r) - \frac{k_2^2}{2}H_0^{(2)}(-ik_2 r)\right] \quad (5.15)$$

By satisfying the boundary condition eq. (5.11), the constant C in eq. (5.14) is determined in terms of the excitation voltage by

$$C = \frac{\kappa^2 GBC_{mV}}{\rho\omega^2 DF(a)} V_{in}(f) \quad (5.16)$$

5.1.2 Sensor model

A single PZT disk with thickness h_p and radius a is mounted on the plate acting as a sensor. The center distance between the actuator and the sensor is R. Ignoring the external electric field $E_i = 0$ and only considering x'-y' plane deformation, the constitutive equation for sensor (direct piezoelectric effect) is simplified from eq. (5.4a) into

$$D = d_{31}(\sigma_{r'} + \sigma_{\theta'}) = \frac{d_{31}E_p}{1-\nu_p}(\varepsilon_{r'} + \varepsilon_{\theta'}) \quad (5.17)$$

where $x'y'z'$ is a local coordinate with origin at the center of the sensor and r', θ' are the local polar coordinate. The scattering effect of the sensor to the incidence waves is also neglected in current study. The electric charges Q accumulated on the top and bottom surfaces of the plate are equal and can be calculated by

$$Q = \frac{1}{4\pi}\int\int\int \nabla \cdot D dV \quad (5.18)$$

Substituting eq. (5.17) into eq. (5.18) and applying Gauss's theorem yields

$$Q = \frac{d_{31}E_p}{4\pi(1-\nu_p)}\int\int(\varepsilon_{r'} + \varepsilon_{\theta'}) r dr' d\theta' \quad (5.19)$$

By treating the PZT sensor as a capacitance (C_a), the output voltage of the sensor is then expressed as

$$V_{out} = \frac{Q}{C_a} = \frac{Qh_p}{\pi K_3 \varepsilon_0 a^2} \tag{5.20}$$

where K_3 is the relative dielectric constant and ε_0 = 2.25×10^{-9} F/in. is the dielectric permittivity of a free space. Substituting eq. (5.20) into eq. (5.19) yields

$$V_{out} = \frac{d_{31} E_p h_p}{4 K_3 \varepsilon_0 (\pi a)^2 (1-\nu_p)} \int\int (\varepsilon_{r'} + \varepsilon_{\theta'}) r' dr' d\theta' \tag{5.21}$$

Assume that the sensor is sufficiently small and the strain is constant inside the sensor area

$$\varepsilon_{r'} \approx \varepsilon_{\theta'} \approx \varepsilon_R \tag{5.22}$$

where ε_R is the strain at the center of the PZT sensor, eq. (5.21) is approximated by

$$V_{out} = \frac{d_{31} E_p h_p \varepsilon_R}{4 K_3 \varepsilon_0 \pi (1-\nu_p)} \tag{5.23}$$

Knowing that $u_r(x,y,t) = z\psi_r(x,y,t)$, differentiating eq. (2.17) gives

$$\begin{aligned} \tilde{\varepsilon}_R = \frac{\rho\omega^2 hC}{4\kappa^2 GB} \Big\{ & (A - \frac{\kappa^2 GB}{\rho\omega^2} - k_1^2) k_1^2 [H_2^{(2)}(k_1 R) - H_0^{(2)}(k_1 R)] \\ & + (A - \frac{\kappa^2 GB}{\rho\omega^2} + k_2^2) k_2^2 [H_2^{(2)}(-ik_2 R) - H_0^{(2)}(-ik_2 R)] \Big\} \end{aligned} \tag{5.24}$$

Combining eq. (5.16), (5.23) and (5.24), the ratio of V_{out} to V_{in} in the frequency domain gives

$$\begin{aligned} \frac{\tilde{V}_{out}}{\tilde{V}_{in}} = \frac{d_{31} E_p h h_p C_{mV}}{16\pi K_3 \varepsilon_0 (1-\nu_p) DF(a)} \Big\{ & (A - \frac{\kappa^2 GB}{\rho\omega^2} - k_1^2) k_1^2 [H_2^{(2)}(k_1 R) - H_0^{(2)}(k_1 R)] \\ & + (A - \frac{\kappa^2 GB}{\rho\omega^2} + k_2^2) k_2^2 [H_2^{(2)}(-ik_2 R) - H_0^{(2)}(-ik_2 R)] \Big\} \end{aligned} \tag{5.25}$$

The time domain response of the sensor output can be obtained by inverse Fourier transform of eq. (5.25). It should be noted that the frequency dependence for all the

piezoelectric constants is neglected in this model.

5.1.3 Experimental validation

The experimental configuration for an integrated plate with sensors/actuators is shown in Figure 5.2. The PZT ceramic disks PKI-402 (Piezo Kinetics, Inc.) are surface-mounted on both sides of an aluminum plate as actuators and on one-side of the plate as an sensors to generate and collect the flexural waves, respectively. The material properties and dimensions for both the plate and the PZTs are listed in Table 5.1. A waveform generator (Hewlett Packard 33120A) generates the excitation signal. The excited signal is first amplified by a wideband power amplifier (Model 7602, Krohn-Hite, Inc.), then drives a pair of PZT actuators to generate transient bending waves. The input voltage applied on the PZT actuator is governed by

$$V_{in}(t) = 40[H(t) - H(t - 5/f_c)]\,(1 - \cos\frac{2\pi f_c t}{5})\sin 2\pi f_c t \qquad (5.26)$$

whose time domain waveform and amplitude spectrum have same shape as shown in Fig. 2.4. It can be found through frequency domain analysis that the frequency components for this excitation signal are mainly concentrated in a small range around the central frequency f_c, thus the dispersive effect of the propagated wave can be significantly reduced, which is beneficial for interpretation of the received data. In fact, the diagnostic signal being controllable is one of the advantages for an active monitoring system. PZT sensors collect the waves and convert them into electrical signals, which are piped into a data acquisition board (Model 5911, National Instrument, Inc.) and recorded in its host PC.

Fig. 5.3 shows the Graphical User Interface (GUI) of the data acquisition system, which is built on a LabView platform. Through the GUI, users can arbitrarily select the data acquisition board (if more than one board are installed) and its input/output channels. The interface provides a convenient way to set the sampling frequency and sample length. This program stores the data into a file consisting of the acquired signals in two columns of data, representing the input voltage of the actuator and the output voltage of

the sensor respectively. Other programs can then extract these data from the file for further signal processing.

Fig. 5.4 demonstrates the excellent repeatability of the experiment data. The curves are the responses of a sensor (R = 8 in.) tested in three different times. The same input governed by eq. (5.26) is excited. Three response curves almost overlap with each other, which demonstrate the excellent repeatability of the signal generation and collection. In the experiments, the responses of all the sensors from the excitation of an actuator need to be recorded to construct a time section, which provides the input data for the migration. Due to the limited number of data acquisition channels, the repeatability of the experimental signals is useful to the experimental procedure. The output of few sensors can be collected at separate times by repeating the same excitation and assemble them together to construct the time section for all the sensors, rather than to collect the output from all the sensors simultaneously through multiple data acquisition channels.

Fig. 5.5 compares the sensor output between the experimental data and the model calculation. Three cases are given with different sensor-actuator distances. The results show that the experimental data agrees very well with those from the model for both the amplitude and the phase of the response. As it is expected, the curve of the sensor output retains the original wave shape of the input signal, which means that the dispersive effect is effectively suppressed by choosing a narrow banded excitation signal. It also demonstrates that a desirable single mode of Lamb waves can be generated in an active SHM system by properly choosing the actuator configuration and the excitation characteristics.

Figure 5.6 still displays the sensor output with different sensor-actuator distances. In this case, the transient waves are excited by another pair of actuators bonded on the plate. The experimental response and calculated data still hold good agreement. Attentive observation reveals that the discrepancy of the amplitude is augmented by comparing with the results in Fig. 5.5. Furthermore, it can be noticed that the amplitude in the experimental data is even greater than the model data, which do not seems to be realistic if some factors in real environments such as attenuation, energy dissipation, etc., are

taken into consideration. This phenomenon may be explained as follows. Although the same value of piezoelectric constants is used in the model calculation for both pairs of PZT actuators, the actual values may vary considerably and the deviation may reach up to 10% according to the data sheet provided by the manufacturer. However, the discrepancy shown in the curves from the viewpoint of real applications may be acceptable.

Figure 5.7 shows the sensor output in cases that the input voltage is applied on the PZT actuators with different central frequencies for constant R = 14 in.. The experimental data in this figure is collected from the response excited by another pair of actuators. The calculated data again agrees well with the real data. The figure also shows that the experimental response is delayed comparing to calculated data and this phase error increases with increasing excitation frequency. This might be caused by the negligence of the frequency dependence of the piezoelectric effect in the model. Another reason for this is that the shear lag is frequency dependent, which however is also omitted in the assumption of perfect bonding.

The model thus is verified with the experimental data. Although the model is simple, it can predict with enough accuracy both the amplitude and the phase of the sensor output for damage detection applications. Small discrepancy between calculated data and the experimental data exists, which might result from the perfect bonding assumption and the omission of the stiffness for both the actuators and sensors. This model could provide a convenient and efficient method to verify the status of integrated sensors/actuators and could even be used to calibrate the monitoring system. In this study, only the first mode of the antisymmetric waves in the plate are considered under the restriction that the PZT actuators are mounted symmetrically corresponding to the middle plane of the plate and only pure bending motion is generated. For other PZT built-in configurations, symmetric motion will be induced and needs to be included into modeling. Another restriction for this model is that it can only correctly predict the sensor response when the input frequency does not exceed the cut-off frequency of thickness shear waves. Otherwise, more than single mode of motions will occur and a higher-order approximation other than MPT needs to be adopted to model the problem.

5.2 Experimental validation of the migration algorithm

In this section, prestack migration algorithm is applied to experimental signals to validate its capability of damage identification. An aluminum plate (dimensions given in Table 5.1) is prepared and a circular arc shape slot with width 0.045 in. and radius 0.5 in. is cut through the thickness to simulate a damage. Nine pairs of PZT disks are mounted on the plate to form a horizontal linear array, with a sensor gap (distance between two adjacent sensors) of 1 in. and total sensor span (distance between the first and the last sensor) 8 in.. Each pair of the disks are mounted at the same position on the top and bottom surfaces of the plate, respectively. The layout of the sensor/actuators and the arc slot are shown in Fig. 5.8. As shown in the figure, the artificial damage is intentionally placed at an asymmetric location relative to the symmetric axis of the sensor array. The intention of this layout design is to provide a case where the damage is arbitrary and to demonstrate the feasibility of migration to detect any damages without *a priori* assumption about their distribution pattern, shape, and dimensions. The voltage excitation of the PZT actuators is governed by eq. (5.26) with central frequency $f_c = 100\text{kHz}$.

Each pair of the nine pairs of the PZT disks is set to be actuators alternatively. When the actuator pair is switched to be connected with input voltage, all other 8 PZT disks on the top surface of the plate function as sensors. Therefore, for each shot there are 8 traces generated. Due to the restriction of number of A/D channel on the data acquisition board, the output of all the sensors is recorded trace by trace through repeating excitation of the actuators. The PZT disks are mounted on the plate before the slot is cut. The responses of the plate without damage due to each excitation are recorded. After the damage is made, the recording is repeated and generates a new 72 trace set (9 shots each with 8 traces). The reflection wave field is then obtained by subtracting the traces with damage by the corresponding traces of the virgin plate. Fig. 5.9 a-e give the traces of the reflection waves excited by the actuators 1, 3, 5, 7 and 9, respectively. One observation is that the amplitude varies largely among traces without a clear pattern. Part of the causes of this phenomenon goes to the inconsistent value of the piezoelectric

constants of the sensors/actuators. The different strength and the thickness of the adhesive layer among PZT disks might also cause this discrepancy. Most importantly, subtracting the signals between with damage and without damage states requires that two signals be in phase completely. Otherwise, even a small phase shift will cause a large error in amplitude under current high frequency circumstances. One way to overcome this error is to use higher sampling frequency and to decrease the phase shift difference.

It has been shown in Chapter 4 that very few sensors/actuators can detect multiple damages successfully. In that case, the given damages are point diffractors and the locations are the key information to be detected. For imaging the outline of a solid shape of damage, an array with enough sensors is necessary to gain the geometry resolution. In the prestack migration, the points at the all grid points along the sensor array are superimposed the boundary conditions to drive the extrapolation of the reflection wave field, which means that the sensor gap should be equal to the grid space. In the current study, the plate in finite difference migration process is discretized by 400×400 grids with equal grid space 0.05 in. in both x and y directions. Since the sensor gap in the experimental setup is chosen as 1 in. based on the consideration of existing experimental conditions and the geometry of the sensors, not all the grid points along the sensor array can obtain real data to be fed in the migration. Thus, to increase the resolution of the migration image, a complete time-section that covers every grid points is constructed though an interpolation based on the acquired data from the nine sensors. The whole reflection wave field is reconstructed in two dimensions (one dimension in time and the other in space) using a polynomial curve fitting through solving the least-squares problem. It should be noted that in a prototype study only few sensors will be used. In real applications, many more sensors are needed for migration based detection and this step of data manipulation becomes unnecessary. Fig. 5.10 a-c show the reconstructed reflection waves by the interpolation process from the excitation of actuator 1, 5 and 9, respectively. Although the interpolation is very coarse due to the large ratio of sensor gap to grid space, it can be observed that the hyperbolic shape of the reflection events is clearly emerged. The shortest arrival time always occurs at the position of sensor 5. The

results show that the basic characteristics of the reflection waves are well preserved through a comparison with the wave field obtained in the numerical simulation.

To assure that the migration algorithm can successfully solve the described problem, a numerical simulation adopting the same configurations used in the experiment is pursued first. In the simulation, the same method of synthesizing the reflection wave field discussed in previous chapters is used. The slot is modeled as a part of the plate with different materials. The bending stiffness at these grid points is chosen one thousandth of the stiffness of the whole plate. Or, equivalently, the thickness at this part is $h/10$. The difference of this simulation with the real specimen is that in the simulation the waves can transmit through the damage, thus the amplitude of the reflection will be weaker than the real case. Since the target of this study is to prove the ability of migration to image the shape and the location of the damages, this difference will not significantly affect the conclusions. Actually, the amplitude information in the migration process is very difficult to preserve and migration methods of the reflection amplitude are still under investigation. In the numerical simulation, the sensor span is chosen as same as the real sensor span (8 in.). Every trace at each grid point between the first and the last sensor are recorded to assemble the time section. Then, the finite difference reverse-time prestack migration algorithm along with the imaging condition discussed in Chapter 4 are applied to image the plate. The migration result (stacked image of nine time sections) is shown in Fig. 5.11. It can be seen that the location of the damage is accurately revealed through the migration process. While the left side of the arc slot is well imaged, its right side is rather vague. It leads to the poor imaging quality of the shape of the arc slot. One of its reasons obviously is that the wavelength currently used (about 0.5 in.) is incapable of resolving the dimensions of the slot, which is only 0.87 in. wide and 0.24 in. high. To improve the image quality, the frequency of the excitation needs to be increased. This explanation can be further strengthened by a simulation case shown in Fig. 5.12. In this case, the excitation wavelength is about one third of the radius of the arc (half circle). Although the image is not very sharp, it clearly displays the arc shape of the damage.

Fig. 5.13 shows the plate image migrated from the data recorded in the experiment.

The experimental result is mostly similar to the result of the numerical simulation and reproduces same conclusions. While the major part of the damage is imaged, there is a lot of scattered blocks around the slot. These errors should be credited to the coarse approximation of the arrival time introduced in the process of reconstructing the wave field through interpolation. This could be corrected by using more sensors and thus omitting the interpolation process. Although the image migrated from the experimental data does not look perfect, it does demonstrate the feasibility of detecting arbitrary damages by interpreting the signals through the migration method. The image resolution and quality of the damages is not a major concern for current study, because they can be improved simply by increasing the density of the sensors and the frequency of the excitation when this technique is adopted in real applications.

Table 5.1 Material constants and geometry of Al-6061 aluminum and piezoelectric disk

Material	Young's modulus E (Ksi)	Poisson's ratio ν	Density ρ (lb./in.^{3})	Relative dielectric constant K_3	Piezoelectric strain cont. d_{31} (m/V)	Thickness h (in.)	Radius a (in.)	Dimension (in. ×in.)
Al-6061	10523	0.30	0.098	N/A	N/A	0.063	N/A	40×32
PKI-402	11031	0.31	0.275	1280	130×10^{-12}	0.010	0.125	N/A

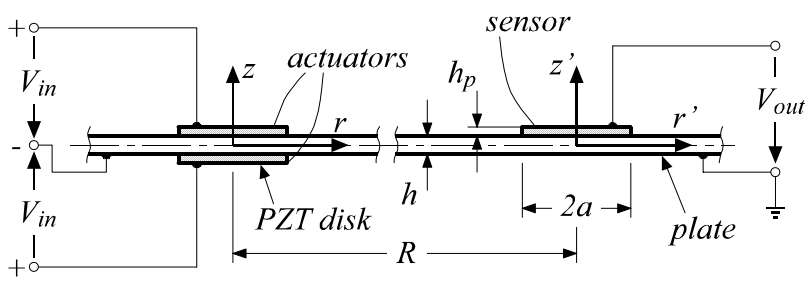

Fig. 5.1 Sensor/actuator model

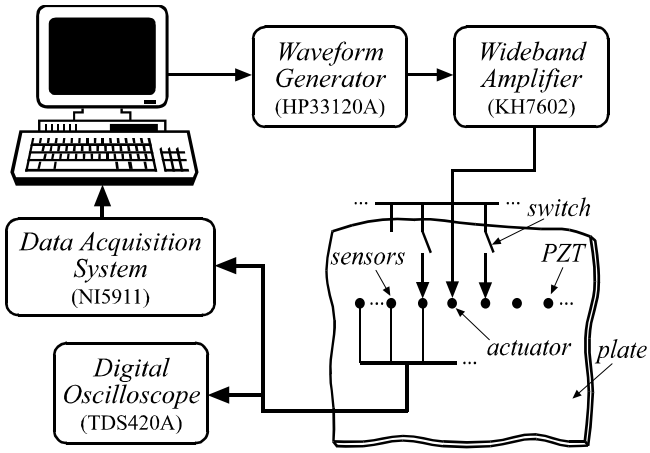

Fig. 5.2 Schematic diagram of experimental apparatus

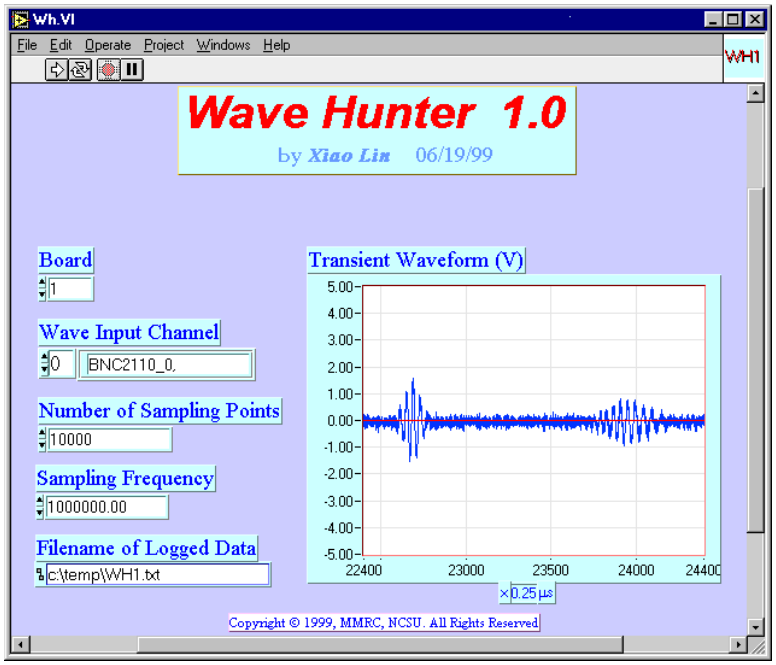

Fig. 5.3 GUI of the data acquisition system

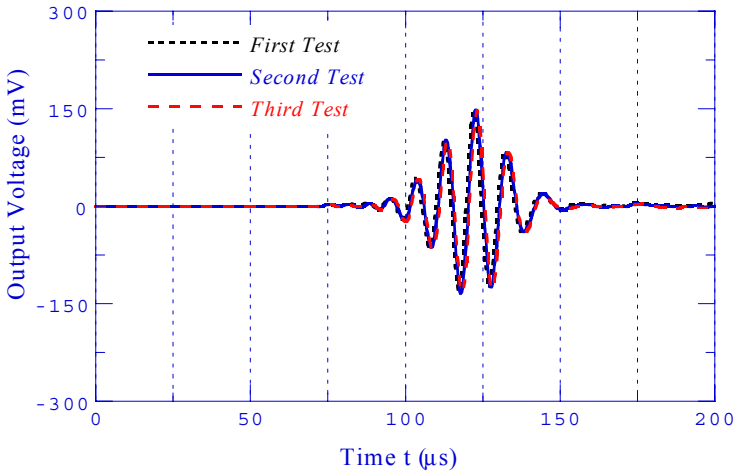

Fig. 5.4 Repeatability of the wave signals

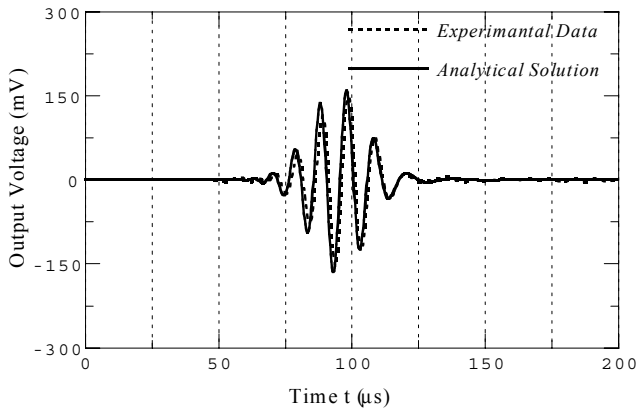

(a) R = 6 in.

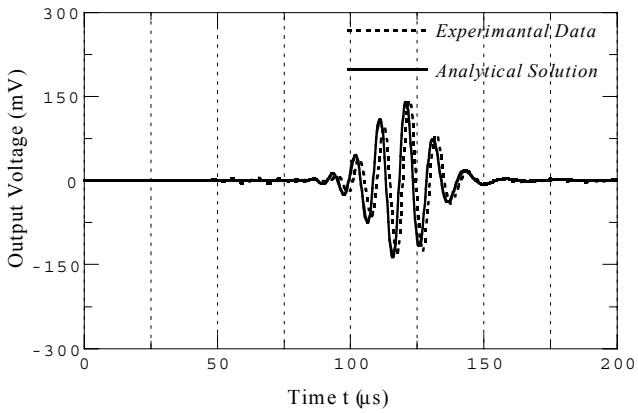

(b) R = 8 in.

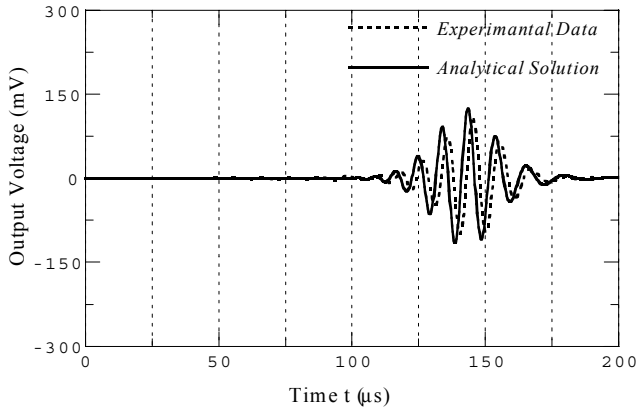

(c) R = 10 in.

Fig. 5.5 Sensor output with different distances between sensor and actuator (f_0 = 100kHz)

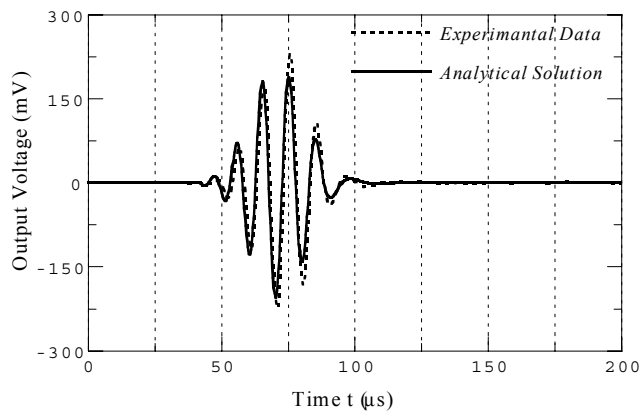

(a) R = 4 in.

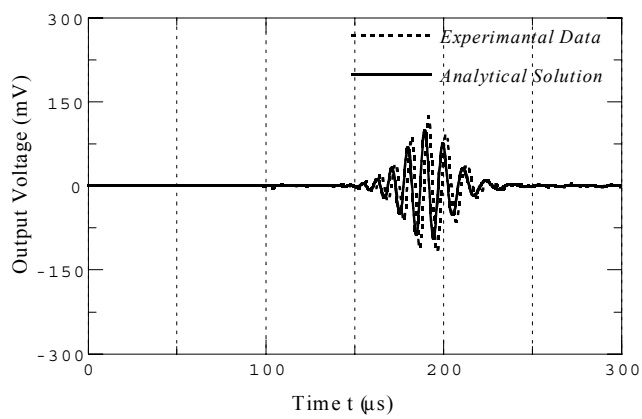

(b) R = 14 in.

Fig. 5.6 Sensor output with different distances between sensor and actuator (f_0 = 100kHz)

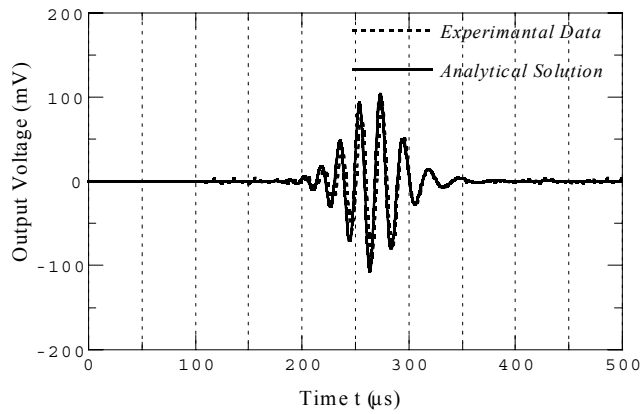

(a) f_0 = 50kHz

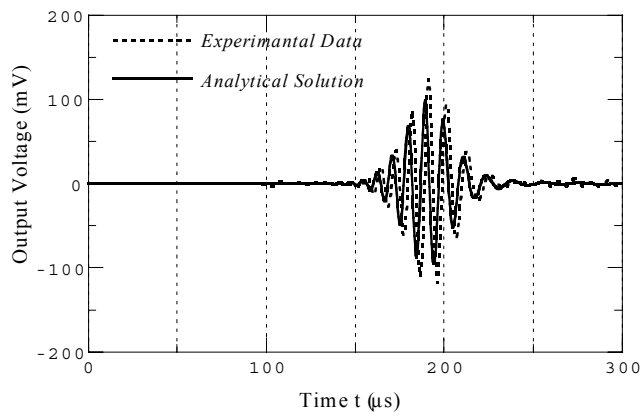

(b) f_0 = 100kHz

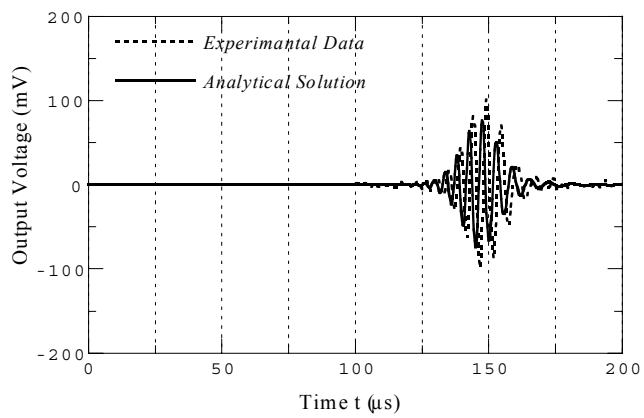

(c) f_0 = 200kHz

Fig. 5.7 Sensor output of given excitation with different central frequencies

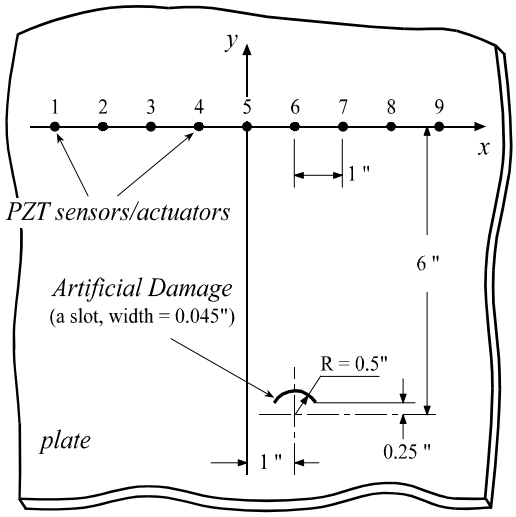

Fig. 5.8 Layout of sensors/actuators and the damage

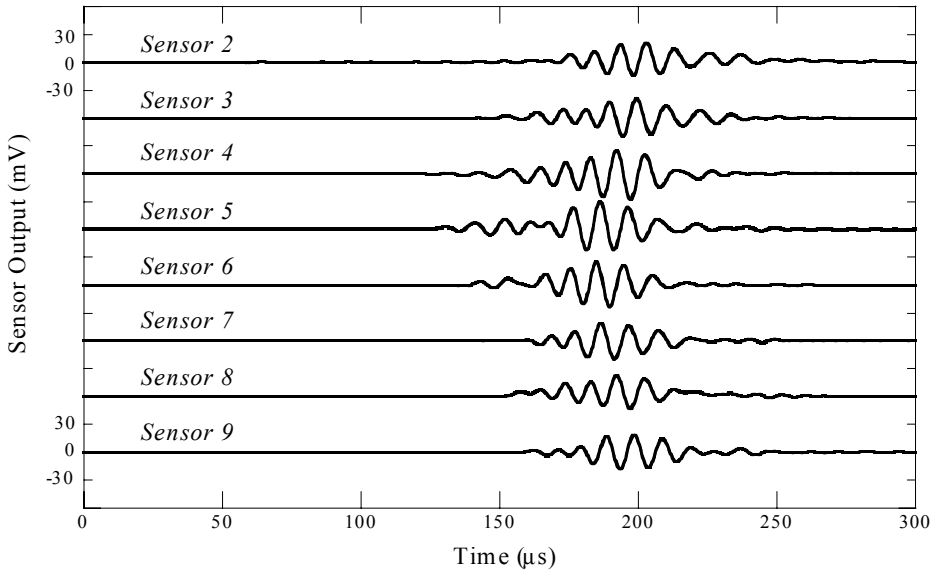

Fig. 5.9(a) Reflection wave signals excited by actuator 1

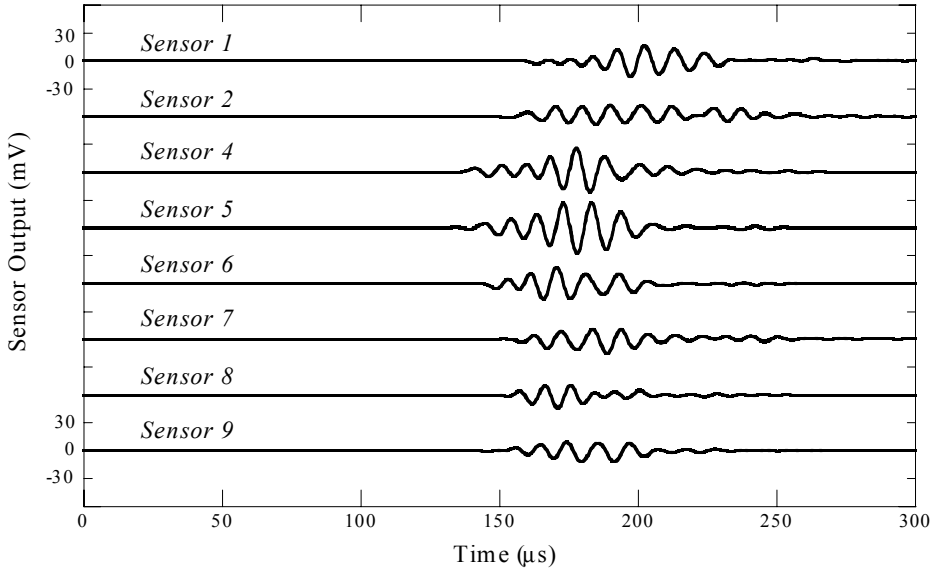

Fig. 5.9(b) Reflection wave signals excited by actuator 3

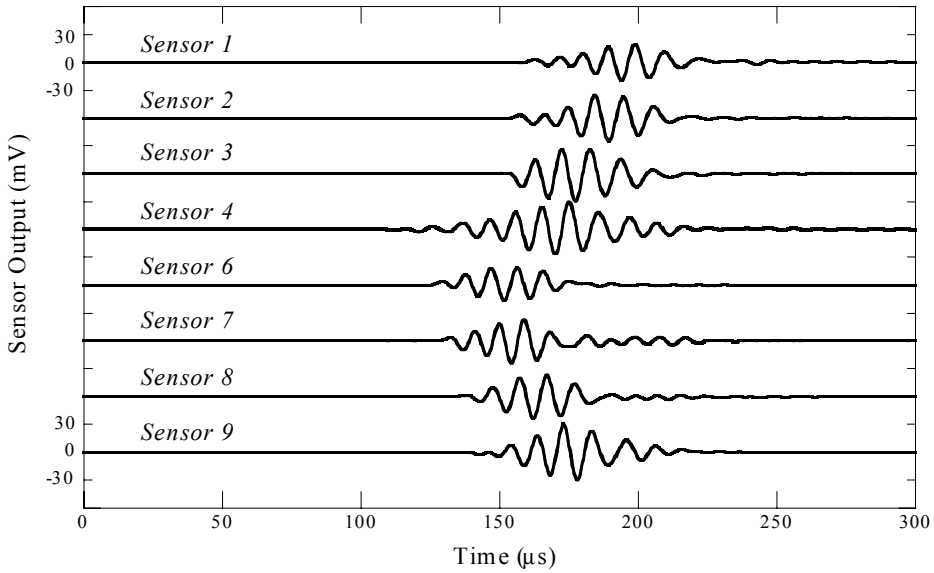

Fig. 5.9(c) Reflection wave signals excited by actuator 5

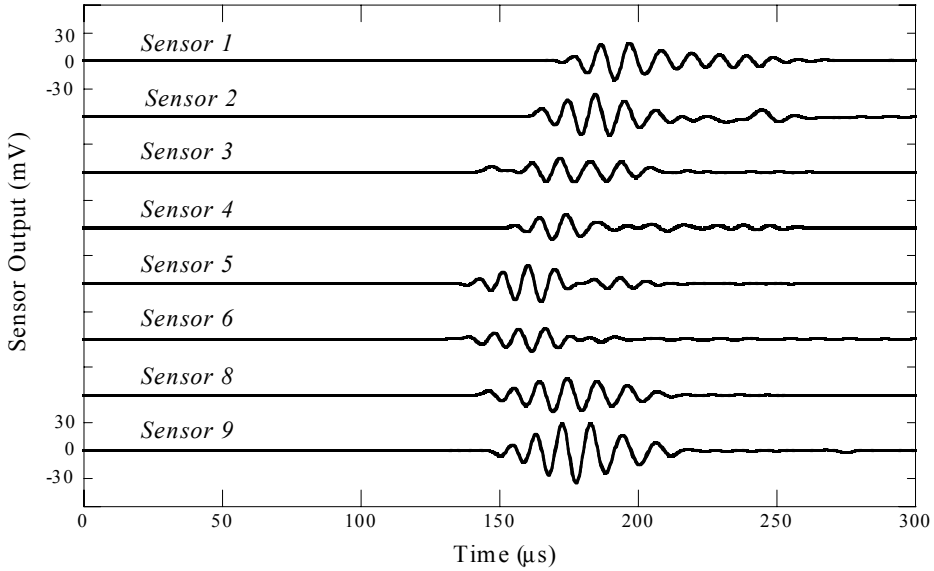

Fig. 5.9(d) Reflection wave signals excited by actuator 7

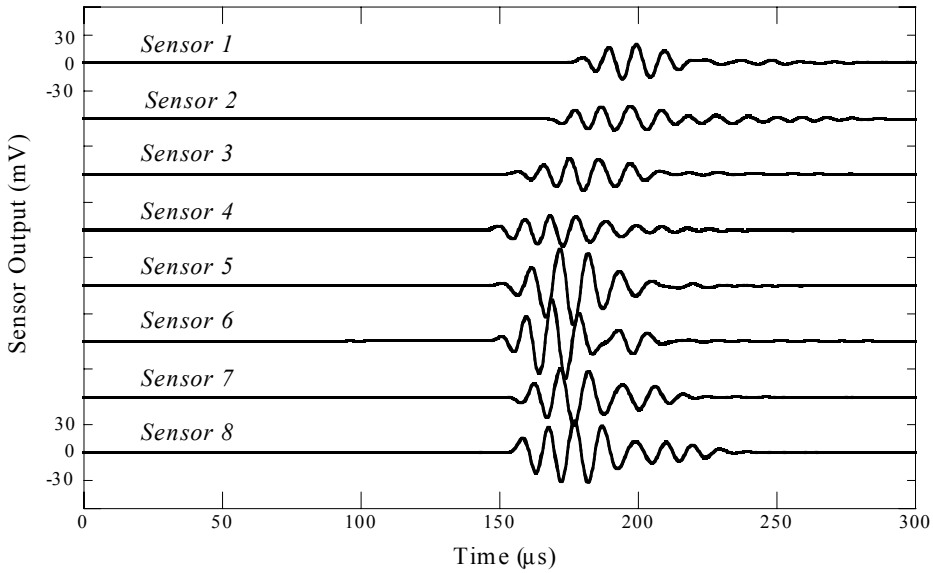

Fig. 5.9(e) Reflection wave signals excited by actuator 9

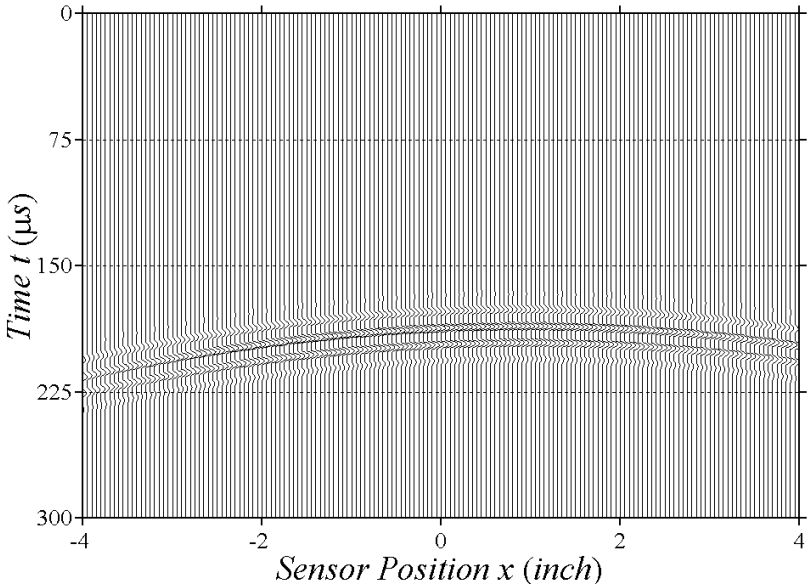

Fig. 5.10(a) Re-constructed reflection wave field (actuator 1)

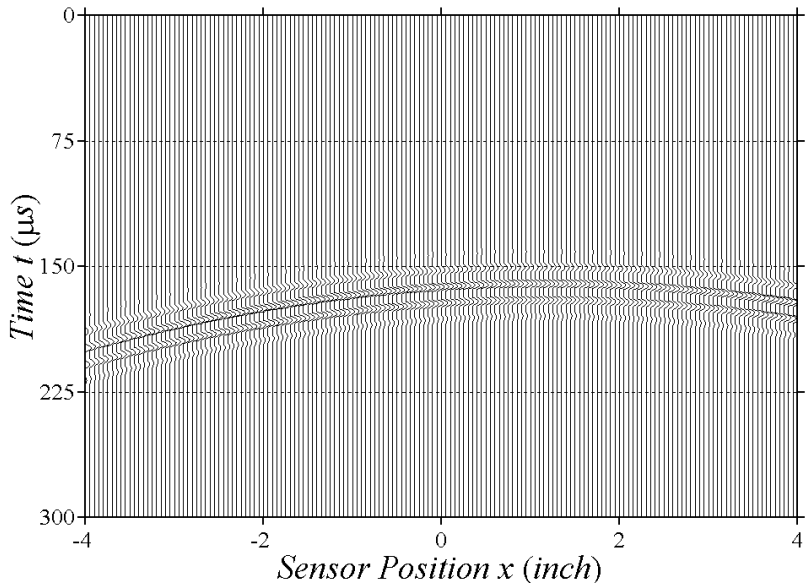

Fig. 5.10(b) Re-constructed reflection wave field (actuator 5)

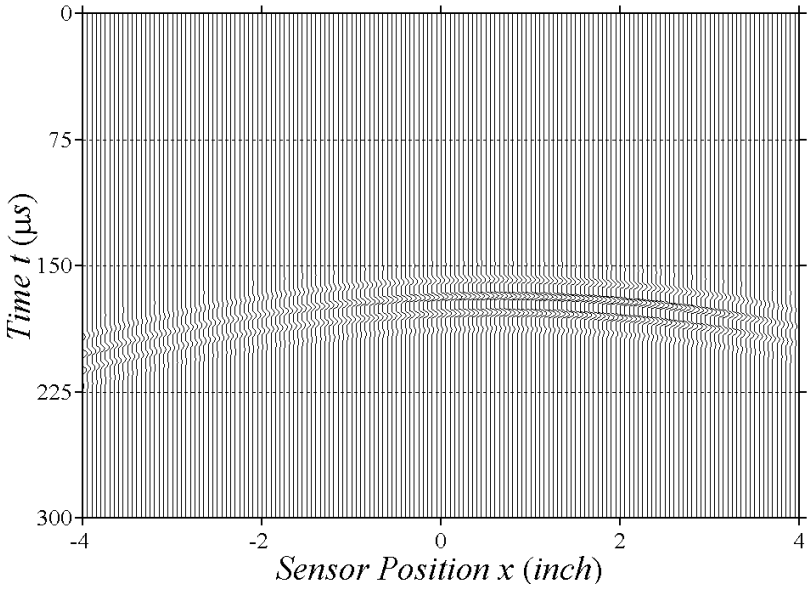

Fig. 5.10(c) Re-constructed reflection wave field (actuator 9)

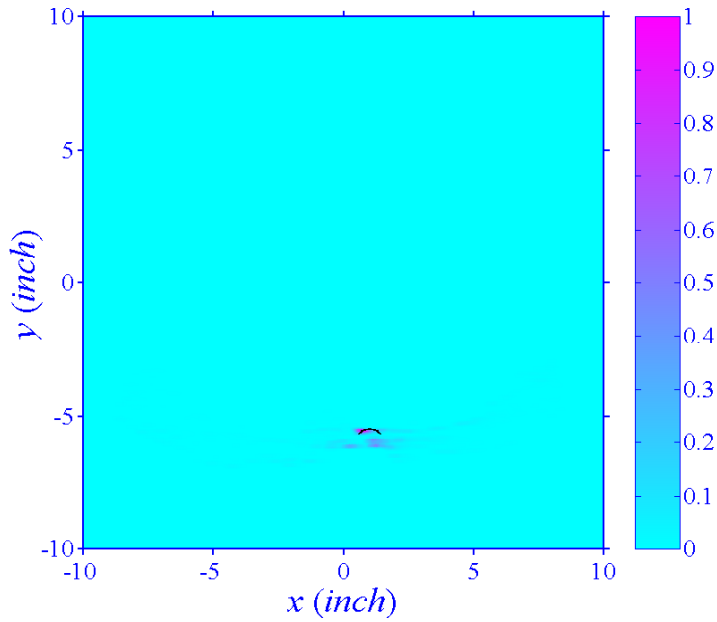

Fig. 5.11 Image of the damage migrated from the synthetic data

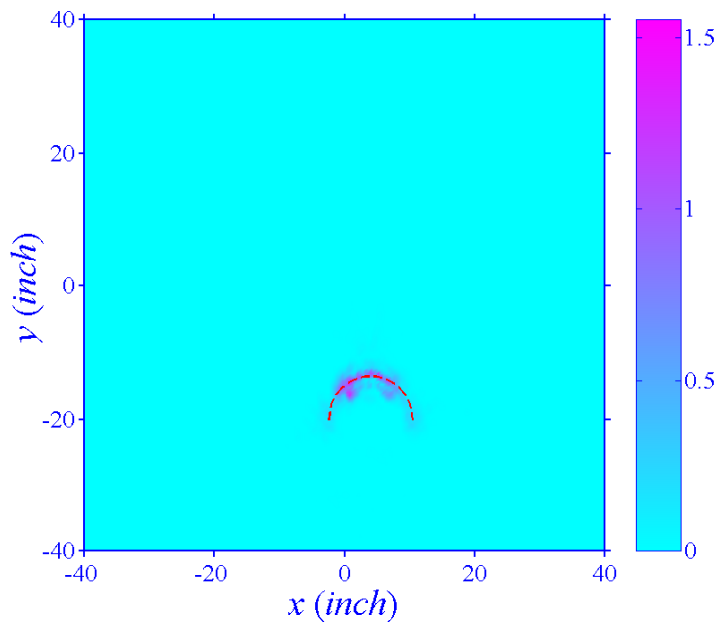

Fig. 5.12 Image of the damage migrated from the synthetic data (larger size arc)

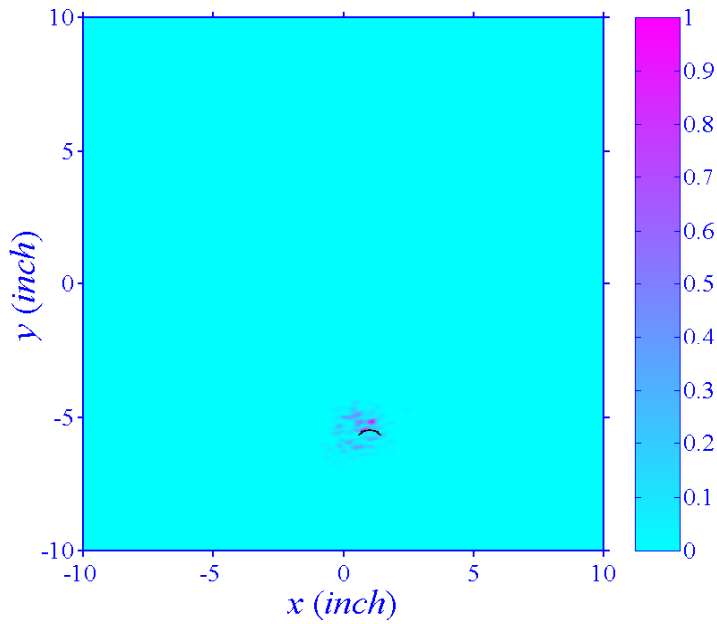

Fig. 5.13 Image of the damage migrated from experimental data

6 Discussion and Conclusions

6.1 Conclusions

Through this study, geophysical migration has been substantiated as a very useful method to interpret the ultrasonic Lamb waves in an active SHM system incorporated with linear piezoelectric actuator/sensor arrays. The migration technique can serve as a bridge that connects distributed sensor/actuator system and ultrasonic signals, and thus makes it possible to construct a near real-time, autonomous, and accurate monitoring system. Migration technique can detect not only the existence of damages, it may also provide the information about the locations, dimensions and seriousness of the damages. The monitoring information can be visually displayed by imaging the structure through the migration results. As an interpretation method of transient wave signals, migration provides the system with a potential to detect incipient damages with very small dimensions. It is not necessary to assume a damage pattern before applying the migration, which makes it feasible of detecting multiple discrete damages. Both poststack and prestack migrations have been numerically demonstrated and prestack migration has been experimentally verified. They possess the capabilities to back-propagate the reflection waves and identify the damages. In the poststack migration, the data is stacked before migration thus only one time migration is needed, which can greatly save calculation time. However, this method is based on an exploding reflector model, in which the stacking process before the migration will destroy the information in the wave field relating to the source-reflector distance and the reflection amplitude. Furthermore, it can not accurately image damages whose surfaces are not parallel to the sensor array. Thus poststack migration is only used to detect the single and symmetric damage in this study. The prestack migration technique simplifies the data processing procedures so that the data distortion due to several stacking procedures like NMO correction can be avoided. Further, it has the potential to compensate for the influence of dispersive waves on the accuracy of damage detection. Overall, prestack migration is a better choice than

poststack migration, except prestack migration requires more computation time. Another conclusion of this study is that the full-way wave equation based migration is proven to have better migration result than the one-way wave equation in SHM. This cross-disciplinary study combines the knowledge of computation mechanics, geophysics and electronics, and has the potential of integrating into real smart material system and structures to strengthen its signal interpretation capacity.

Specific contributions of this study to the field of the research can be summarized as follows:

(a) The basic framework of applying geophysical migration in active SHM applications has been systematically conducted. The feasibility of adopting migration technique to interpret ultrasonic wave signals has been substantiated by both the numerical and experimental studies.

(b) An analytical solution has been derived for the transient flexural waves of an infinite plate subjected to a point loading. The solution is based on Mindlin plate theory and could be reduced to the response derived from the classical plate theory when both rotary inertia and transverse shear deformation effect are ignored.

(c) An analytical model of piezoelectric (PZT) sensors/actuators incorporated in plate structures has been derived. This model combines the analytical solution of Mindlin plate theory and the electromechanical coupling of piezoelectric sensors/actuators. Thus the voltage output of a sensor could be obtained directly from the voltage input of an actuator.

(d) A one-way version of flexural wave equation has been derived based on the governing equation of Mindlin plate theory in a matrix form and the characteristic velocity (eigenvalue) analysis.

(e) A 2-6 order MacCormack finite difference algorithm has been implemented into modeling the plate problems using Mindlin plate theory. The stability and accuracy criteria for the plates are given and verified.

(f) An excitation-time imaging condition specifically for the migration of waves in

a plate is introduced based on ray-tracing concepts and the asymptotic properties of flexural wave velocities. The imaging condition has been formulated based on general ray equations for 2D heterogeneous materials, thus can be extended to structures other than flat plates or composite structures.

6.2 Future studies

Although briefly mentioned in previous chapters, at least two problems are not fully resolved in this study. One is the deconvolution of the recorded signals before migration; the other is the correction of the dispersive relation of the one-way wave equation. The resolution of the final images could be improved if these two procedures are incorporated in the migration process. The migration technique is suitable for identifying damages such as matrix cracking and delamination in general composite structures. Thus extending the study of migration to composite structures using distributed actuators/sensors is needed. Further, in some situations where the sensors/actuators are embedded in rather than surface-bonded on the structures or the excitation frequency is sufficiently high that other Lamb waves besides A_0 mode can prevail. In these cases, Mindlin plate theory may be not valid and other theories should be adopted to model the problems and to implement the migration. It could be noticed that the migration method can be used to interpret wave signals received or generated by any kind of sensors/actuators other than piezoelectric materials, thus it also can be adopted in the optic fiber based health monitoring system. In view of increasing the calculation efficiency and improving the resolution of the migration result, exploring migration techniques other than using finite difference method and extending two-dimensional to fully three-dimensional migration may be important topics to achieve a near real-time SHM system.

7 References

[1] Achenbach, J. D. and Thompson, D. O., (1991), "Towards quantitative nondestructive evaluation of aging aircraft", *Structural Integrity of Aging Airplanes* (Editors: S. N. Atluri, S. G. Sampath and P. Tong), Springer-Verlag, New York, pp. 1-13.

[2] Alleyne, D. N. and Cawley, P., (1992a), "Optimization of Lamb wave inspection techniques", *NDT & E International*, Vol. 25, No. 1, pp. 11-22.

[3] Alleyne, D. N. and Cawley, P., (1992b), "The interaction of Lamb waves with defects", *IEEE Transactions on Ultrasonics, Ferroelectrics and Frequency Control*, Vol. 39, No. 3, pp. 381-397.

[4] Assadi-Lamouki, A. and Krauthammer, T., (1989), "An explicit finite difference approach for the Mindlin plate analysis", *Computers & Structures*, Vol. 31, No. 4, pp. 487-194.

[5] Balasubramanyam, R., Quinney, D., Challis, R. E. and Todd, C. P. D., (1996), "A finite difference simulation of ultrasonic Lamb waves in metal sheets with experimental verification", *Journal of Physics D*: *Applied Physics*, Vol. 29, pp. 147-155.

[6] Bar-Cohen, Y., Mal, A. K. and Chang, Z., (1998), "Composite material defects characterization using leaky Lamb wave dispersion data", *Proceedings of SPIE on Nondestructive Evaluation of Materials and Composites* II, San Antonio, Texas, Vol. 3396, pp. 180-186.

[7] Bayliss, A., Jordan, K. E., LeMesurier, B. J. and Turkel, E., (1986), "A fourth-order accurate finite-difference scheme for the computation of elastic waves", *Bulletin of the Seismological Society of America*, Vol. 76, No. 4, pp. 1115-1132.

[8] Boller, C., (1996), "Fundamentals on damage monitoring", *AGARD-LS*-205, pp. 4.1-4.15.

[9] Boller, C. and Biemans, C., (1997), "Structural health monitoring in aircraft: state-of-the-art, perspectives and benefits", *Proceedings of the 1st International Workshop on Structural Health Monitoring*, Stanford University, pp. 541-552.

[10] Bond, L. J., Punjani, M. and Saffari, N., (1988), "Ultrasonic wave propagation and scattering using explicit finite difference method", *Mathematical Modeling in Non-destructive Testing*, (editors: M. Blakemore and G. A. Georgiou), Clarendon Press, Oxford, pp. 81-124.

[11] Cady, W. G., (1946), "*Piezoelectricity*", GcGraw-Hill, New York.

[12] Chang, F. K., (1999), "Structural health monitoring, a summary report on the first international workshop on structural health monitoring", *Proceedings of the 2nd International Workshop on Structural Health Monitoring*, Stanford University, pp. xix-xxix.

[13] Chang, W. F. and McMechan, G. A., (1986), "Reverse-time migration of offset vertical seismic profiling data using the excitation-time imaging condition", *Geophysics*, Vol. 51, No. 1, pp. 67-84.

[14] Chee, C. Y. K., Tong, L. and Steven, G. P., (1998), "A review on the modelling of piezoelectric sensors and actuators incorporated in intelligent structure", *Journal of Intelligent Material Systems and Structures*, Vol. 9, pp. 3-19.

[15] Cherukuri, H. P., Shawki, T. G. and El-Raheb, M., (1996), "A finite difference scheme for elastic wave propagation in a circular disk", *Journal of the Acoustical Society of America*, Vol. 100, No. 4, pp. 2139-2155.

[16] Chien, L. S., (1997), "In-situ damage detection of plates by the migration technique", *Proceedings of the 38th AIAA/ASME/ASCE/AHS/ASC Structures, Structural, Dynamics, and Materials Conference*, Kissimmee, FL, AIAA-97-1225, pp. 1110-1114.

[17] Claerbout, J. F., (1971), "Toward a unified theory of reflection mapping", *Geophysics*, Vol. 36, No. 3, pp. 467-481.

[18] Claerbout, J. F. and Doherty, M., (1972), "Downward continuation of moveout corrected seismograms", *Geophysics*, Vol. 37, No. 5, pp. 741-768.

[19] Claerbout, J. F., (1976), "*Fundamentals of Geophysical Data Processing*", McGraw-Hill, New York.

[20] Claerbout, J. F., (1985), "*Imaging the Earth's Interior*", Blackwell Scientific Publications, Boston.

[21] Crawley, E. F. and Lazarus, K. B., (1991), "Induced strain actuation of isotropic and anisotropic plates", *AIAA Journal*, Vol. 29, No. 6, pp. 944-951.

[22] Crawley, E. F., (1994), "Intelligent structure for aerospace: a technology overview and assessment", *AIAA Journal*, Vol. 32, No. 8, pp. 1689-1699.

[23] Dai, N., (1993), "Finite difference simulation and imaging of seismic waves in complex media", Ph. D. dissertation, University of Alberta, Canada.

[24] Datta, S. K., Al-Nassar, Y. and Shah, A. H., (1991), "Lamb wave scattering by a surface breaking crack in a plate", *Review of Progress in Quantitative Nondestructive Evaluation*, Vol. 10A, pp. 97-104.

[25] Deutsch, W. A. K., Cheng, A. and Achenbach, J. D., (1997), "Self-focusing of Rayleigh waves and Lamb waves with a linear phased array", *Research in Nondestructive Evaluation*, Vol. 9, pp. 81-95.

[26] Dimitriadis, E. K., Fuller, C. R. and Rogers, C. A., (1991), "Piezoelectric actuators for distributed vibration excitation of thin plates", *Journal of Vibration and Acoustics*, Vol. 113, pp. 100-107.

[27] Doyle, J. F., (1989), "*Wave Propagation in Structures: an FFT-based Spectral Analysis Methodology*", Springer-Verlag, New York.

[28] Egusa, S. and Iwasawa, N., (1998), "Piezoelectric paints as one approach to smart structural materials with health monitoring capabilities", *Smart Materials and Structures*, Vol. 7, pp. 438-445.

[29] Engquist, B. and Majda, A., (1977), "Absorbing boundary conditions for the

numerical simulation of waves", *Mathematics of Computation*, Vol. 31, No. 139, pp. 629-651.

[30] Fink, M., (1992), "Time reversal of ultrasonic field", *IEEE Transactions on Ultrasonics, Ferroelectrics, and Frequency Control*, Vol. 39, No. 5, pp. 555-592.

[31] Fink, M., (1993), "Time reversal mirror", *Journal of Physics D: Applied Physics,* Vol. 26, pp. 1333-1350.

[32] Gorman, M. R. and Prosser, W. H., (1996), "Application of normal mode expansion to AE waves in finite plates", *Journal of Applied Mechanics*, Vol. 63, No. 2, pp. 555-557.

[33] Gottlieb, D. and Turkel, E., (1976), "Dissipative two-four methods for time-dependent problems", *Mathematics of Computation*, Vol. 30, pp. 703-723.

[34] Gottlieb, D., Gunzberger, M. D. and Turkel, E., (1982), " On numerical boundary treatment for hyperbolic systems for finite difference and finite element methods", *SIAM Journal on Numerical Analysis*, Vol. 19, pp. 671-682.

[35] Graff, K. F., (1991), "*Wave Propagation in Elastic Solids*", Dover Publications, New York.

[36] Guo, Z., Achenbach, J. D. and Krishnaswamy, S., (1997), "EMAT generation and laser detection of single Lamb wave modes", *Ultrasonics*, Vol. 35, pp. 423-429.

[37] Hayashi, Y., Ogawa, S., Cho, H. and Takemoto, M., (1999), "Non-contact estimation of thickness and elastic properties of metallic foils by the wavelet transform of laser-generated Lamb waves", *NDT & E International*, Vol. 32, No. 1, pp. 21-27.

[38] Hickman, G. A., Gerardi, J. J. and Feng, Y., (1991), "Application of smart structures to aircraft health monitoring", *Journal of Intelligent Material Systems and Structure*, Vol. 2, pp. 411-430.

[39] Hsu, N. N., Simmons, J. A. and Hardy, S. C., (1977), "An approach to acoustic emission signal analysis - theory and experiment", *Materials Evaluation*, Vol. 35,

pp. 100-106.

[40] IEEE, (1978), "IEEE Standard 176: Piezoelectricity", IEEE, New York.

[41] Karunasena, W. M., Liew, K. M. M. and Kitipornchai, S., (1995), "Hybrid analysis of Lamb wave reflection by a crack at the fixed edge of a composite plate", *Computer Methods in Applied Mechanics and Engineering*, Vol. 125, pp. 221-233.

[42] Kelly, K. R., Ward, R. W., Treitel, S. and Alford, R. M., (1976), "Synthetic seismograms: a finite difference approach", *Geophysics*, Vol. 41, No. 1, pp. 2-27.

[43] Kino, G. S., Barnett, D. M., Grayeli, N., Herrmann, G., Hunter, J. B., Ilic, D. B., Johnson, G. C., King, R. B., Scott, M. P., Shyne, J. C. and Steele, C. R., (1980), "Acoustic measurements of stress fields and microstructure", *Journal of Nondestructive Evaluation*, Vol. 1, No. 1, pp. 67-77.

[44] Kishimoto, K., Inoue, H., Hamada, M. and Shibuya, T., (1995), "Time frequency analysis of dispersive waves by means of wavelet transform", *Journal of Applied Mechanics*, Vol. 62, pp. 841-846.

[45] Kudva, J. N., Marantidis, C., Gentry, J. and Blazic, E., (1993), "Smart structures concepts for aircraft structural health monitoring*", Proceedings of SPIE on Smart Structures and Intelligent Systems*, Albuquerque, New Mexico, Vol. 1917, pp. 964-971.

[46] Kundu, T. and Maslov, K., (1997), "Material interface inspection by Lamb waves", *International Journal of Solids and Structures*, Vol. 34, No. 29, pp. 3885-3901.

[47] Kuzuoglu, M. and Mittra, R., (1999), "Finite element solution of electromagnetic problems over a wide frequency range via the Padé approximation", *Computer Methods in Applied Mechanics and Engineering*, Vol. 169, pp. 263-277.

[48] Lee, W. H. K. and Stewart, S. W., (1981), "*Principles and Applications of Microearthquake Networks*", Academic Press, New York.

[49] Lin, X., Pan, E. and Yuan, F. G., (1999), "Imaging the damage in the plate with migration technique", *Proceedings of 2nd International Workshop on Structural*

Health Monitoring, Stanford University, pp. 731-742.

[50] Lin, X. and Yuan, F. G., (2000a), "Prestack reverse-time migration in structural health monitoring", *Proceedings of the 41st AIAA/ASME/ASCE/AHS/ASC Structures, Structural Dynamics, and Materials Conference*, Atlanta, Georgia, AIAA 2000-1701.

[51] Lin, X. and Yuan, F. G., (2000b), "Damage detection of a plate using migration techniques", *Journal of Intelligent Systems and Structures*, in review.

[52] Lin, X. and Yuan, F. G., (2000c), "Detection of multiple damages by prestack reverse time migration", *AIAA Journal*, accepted.

[53] Liu, P. L., Tsai, C. D. and Wu, T. T., (1996), "Imaging of surface-breaking concrete cracks using transient elastic wave", *NDT & E International*, Vol. 29, No. 5, pp. 323-331.

[54] Loewenthal, D., Lu, L., Roberson, R. and Sherwood, J., (1974), "The wave equation applied to migration", *Geophysical Prospecting*, Vol. 24, pp. 380-399.

[55] Medick, M. A., (1961), "On classic plate theory and wave propagation", *Journal of Applied Mechanics*, Vol. 28, pp. 223-228.

[56] Miklowitz, J., (1960), "Flexural stress waves in an infinite elastic plate due to a suddenly applied concentrated transverse load", *Journal of Applied Mechanics*, Vol. 27, pp. 681-689.

[57] Mindlin, R. D., (1951), "Influence of rotatory inertia and shear on flexural motions of isotropic, elastic plates", *Journal of Applied Mechanics*, Vol. 18, pp. 31-38.

[58] Mindlin, R. D. and Deresiewicz, H., (1954), "Thickness-shear and flexural vibrations of a circular disk", *Journal of Applied Physics*, Vol. 25, No. 10, pp. 1329-1332.

[59] Moetakef, M. A., Joshi, S. P. and Lawrence, K. L., (1996), "Elastic wave generation by piezoceramic patches", *AIAA Journal*, Vol. 34, No. 10, pp. 2110-2117.

[60] Monkhouse, R. S. C., Wilcox, P. W. and Cawley, P, (1997), "Flexible interdigital

PVDF transducers for the generation of Lamb waves in structures", *Ultrasonics*, vol. 35, pp. 489-498.

[61] Moulin, E., Assaad, J., Delebarre, C. and Osmont, D, (1999), "Lamb waves generation using a transducer embedded in a composite plate", *Proceedings of the 12th International Conference on Composite Materials*, Paris.

[62] Norris, A. N. and Vemula, C., (1995), "Scattering of flexural waves on thin plates", *Journal of Sound and Vibration*, Vol. 181, No. 1, pp. 115-125.

[63] Pao, Y. H., and Chao, C. C., (1964), "Diffraction of flexural waves by a cavity in an elastic plate", *AIAA Journal*, Vol. 2, No. 11, pp. 2004-2010.

[64] Proctor, T. M., Breckenridge, F. R. and Pao, Y. H., (1983), "Transient waves in an elastic plate: theory and experiment compared", *Journal of the Acoustical Society of America*, Vol. 74, No. 6, pp. 1905-1907.

[65] Roh, Y. S. and Chang, F. K., (1995), "Effect of impact damage on Lamb wave propagation in laminated composites", *Dynamic Response and Behavior of Composites*, ASME AD-Vol. 46, pp. 127-138.

[66] Sun, R. and McMechan, G. A., (1986), "Pre-stack reverse-time migration for elastic waves with application to synthetic offset vertical seismic profiles", *Proceedings of the IEEE*, vol. 74, No. 3, pp.457-465.

[67] Tan, K. S., Guo, N., Wong, B. S. and Tui, C. G., (1995), "Experimental evaluation of delaminations in composite plates by the use of Lamb waves", *Composites Science and Technology*, Vol. 53, pp. 77-84.

[68] Takadoya, M., Notake, M., Kitahara, M., Achenbach, J. D., Guo, Q. C. and Peterson, M. L., (1992), "Neural network approach to the inverse problem of crack depth determination from ultrasonic backscattering data", *IUTAM Symposium on Inverse Problems in Engineering Mechanics*, Tokyo, pp. 413-422.

[69] Thomas, G., (1995), "Overview of nondestructive evaluation technologies", *Proceedings of SPIE on Nondestructive Evaluation of Aging Aircraft, Airports,*

Aerospace hardware, and Materials, Oakland, California, Vol. 2455, pp. 5-9.

[70] Timoshenko, S. and Woinowsky-Krieger, S., (1959), "*Theory of Plates and Shells*", 2nd Ed., McGraw-Hill, New York.

[71] Tracy, M., Roh, Y. S. and Chang, F. K., (1996), "Impact damage diagnostics for composite structures using built-in sensors and actuators", *Proceedings of SPIE on Smart Structures and Materials*, Vol. 2779, Lyon, France, pp. 118-123.

[72] Vemula, C. and Norris, A. N., (1997), "Flexural wave propagation and scattering on thin plates using Mindlin theory", *Wave Motion*, Vol. 26, pp.1-12.

[73] Wang, Y., (1998), "Modeling of surface mounted circular piezoelectric sensors and actuators for wave propagation in plates", Ph.D. dissertation, Stanford University.

[74] Weaver, R. L. and Pao, Y. H., (1982), "Axisymmetric elastic waves excited by a point source in a plate", *Journal of Applied Mechanics*, Vol. 49, pp. 821-836.

[75] Worlton, D. C., (1957), "Ultrasonic testing with Lamb waves", *Nondestructive Testing*, No. 7, pp. 219-222.

[76] Yilmaz, O. and Claerbout, J. F., (1980), "Prestack partial migration", *Geophysics*, Vol. 45, No. 12, pp. 1753-1779.

[77] Yilmaz, O., (1993), "Seismic Data Processing", Society of Exploration Geophysicists, Tulsa, Oklahoma.

[78] Yuan, F. G. and Lin, X., (2000), "Accurate simulation of flexural waves in structural health monitoring tests", *IUTAM Symposium on Smart Structures and Structronic Systems,* Magdeburg, Germany.